Ultra-Compact HII Regions

Harrison George Steggles

School of Physics and Astronomy

University of Leeds

Submitted in accordance with the requirements for the degree of

Doctor of Philosophy

September 2016

Declaration

The candidate confirms that the work submitted is his/her own and that appropriate credit has been given where reference has been made to the work of others. This copy has been supplied on the understanding that it is copyright material and that no quotation from the thesis may be published without proper acknowledgement.

Harrison George Steggles

September 2016

Acknowledgements

I would like to first thank both of my supervisors, Prof. Melvin Hoare and Dr. Julian Pittard, for not just their guidance during my research, but also for being all-round great people. Their combined knowledge was incredibly useful especially during group discussions, which I will miss.

To the PhD students who started alongside me (Jacob Close, Karim Ababakr and Fernando Olguin): thank you for the help and for working hard with me. I'd like to also thank everyone in the Astrophysics Group for making these four years some of the best in my life. I will miss ending the week at Fenton with you lot!

Thank you Mallory Taylor for marrying me, for keeping me happy and also for proofreading this thesis.

Lastly, thanks go to my parents and my brothers and sisters for supporting me and always being there. All I ever want is to make all of you proud.

Abstract

In this thesis I have studied hydrodynamical models of cometary HII regions and distributions of UCHII (ultra-compact HII) regions in simulated surveys, for comparison with CORNISH (Co-Ordinated Radio 'N' Infrared Survey for High-mass star formation). I present the numerical method used to model the evolution of cometary HII regions produced by ZAMS stars of O and B spectral types, which are driving strong winds and are born off-centre from spherically symmetric cores with power-law ($\alpha = 2$) density slopes. A model parameter grid was produced that spans stellar mass, age and core density. Exploring this parameter space I investigated limb-brightening, a feature commonly seen in cometary HII regions. It was found that all of the models produce this feature. The models have a cavity, bounded by a contact discontinuity separating hot shocked wind and ionised ambient gas, that is similar in size to the surrounding HII region. Due to early pressure confinement, shocks outside of the contact discontinuity were not seen, but the cavities were found to continue to grow. The cavity size in each model plateaus as the expansion of the HII region stagnates, which could be due to the Kelvin-Helmholtz instabilities at the interface mixing in cooler gas. SEDs (spectral energy distributions) of the models are similar to those from identical stars evolving in uniform density fields. The turn-over frequency is lower in the power-law models due to a higher proportion of low density gas covered by the HII regions.

Following from this I have simulated CORNISH surveys for stars, varying the local density at the location of stellar birth. I have shown that the models used

can reproduce the observed size and flux distributions in the CORNISH survey. Higher density environments generally lead to better fits to the observed size and flux distributions. A good match between the overall number of UCHII regions in the simulated surveys for a SFR $= 1.5\,\mathrm{M}_{\odot}\,\mathrm{yr}^{-1}$ can be achieved if it is considered that stars are born in a distribution of local densities rather than a single density.

Table of contents

List of figures

List of tables

Acronyms

AMR adaptive mesh refinement. 141–143

CFD computational fluid dynamics. 22

CORNISH Co-Ordinated Radio 'N' Infrared Survey for High-mass star formation. vii, viii, xiii, xviii–xxi, xxv, 9, 10, 16, 17, 74, 108, 114–116, 118, 121, 125–131, 133–137, 140, 141, 143

EUV extreme ultra-violet. 55

EVLA Extended VLA. 125, 126

FUV far ultra-violet. 55–57, 86

FVM finite-volume method. 21, 22

GLIMPSE the Galactic Legacy Infrared Mid-Plane Survey Extraordinaire. 16

GMC giant molecular cloud. 3, 4

HCHII hyper-compact HII. 16

HEALPix Hierarchical Equal-Area isoLatitude Pixelization of the sphere. 142

HLL Harten–Lax–van Leer. xiii, 25, 26, 28, 29, 31

HLLC Harten–Lax–van Leer–Contact. xiii, 25, 27–29, 31

HMC high-mass core. 5

HMPO high-mass protostellar object. 5, 6

HMSC high-mass starless core. 5

IMF initial mass function. xix, 5, 7, 116, 119

IR infra-red. 17, 73

ISM interstellar medium. 1–4, 14, 142

LTE local thermodynamic equilibrium. 68, 70, 71

MHD magneto-hydrodynamic. 4

MS main-sequence. 5, 116, 122, 125

MUSCL Monotonic Upstream-Centered Scheme for Conservation Laws. 34

PMS pre-main-sequence. 5

RMS Red MSX Source. 11, 73, 115

SED spectral energy distribution. vii, 16, 111, 113, 140

SFR star formation rate. 115, 116, 134

SPH smoothed particle hydrodynamics. 6, 7

TORCH The Operator-split Radiation, Cooling, Hydro-code. xiv, 19, 22, 24, 32–36, 39, 40, 42, 46–49, 54, 57, 59, 63, 74, 139, 141

TVD total variation diminishing. xiv, 33–36

UCHII ultra-compact HII. vii, viii, xiii, xvii, xix–xxi, xxv, 2, 9–12, 14–17, 48, 61, 73, 74, 95, 103, 105, 116, 118, 123, 125–130, 133–137, 139–143

YSO young stellar object. 115

ZAMS zero age main sequence. 139

Chapter 1

Introduction

Massive stars are an important component of the universe. They are the main sources of stellar feedback that influences the structure, evolution and chemical composition of a galaxy. High-mass stars are born in the dense parts of the ISM, erupting with powerful jets and radiatively driven winds that contribute to not only the chemical enrichment of the ISM but the destruction of the natal cloud. Extreme ultra-violet radiation is emitted from high-mass stars, which ionises and heats the surrounding gas. This produces an overpressure that drives a shock into the ambient medium, sweeping gas into a shell that ultimately disperses the parent molecular cloud and may also trigger further star formation (Hoare et al., 2007). When massive stars die they undergo one of the most explosive and energetic events in the universe: the supernova. Supernovae cause intense bursts of radiation and expel most of the star's current mass. They form shock waves that travel through the ISM, enriching it with the heavy elements produced by the star and possibly stimulating the formation of a new generation of stars.

How high-mass stars are formed is still poorly understood. They have short lifetimes which, along with their relatively low formation rates, indicates that only a small proportion of stars in the galaxy have very high masses. The scarcity of observational data is a significant problem for the testing of theoretical models;

some important phases of evolution pass very quickly. The youngest massive stars, however, are associated with UCHII regions, a phase that lasts longer than expected (Wood and Churchwell, 1989b). These objects form tantalizingly regular morphologies and, as the stars are very young, their relatively undisturbed birth environments can be studied.

1.1 Structure Formation

1.1.1 The Interstellar Medium

Galaxies are complex gravitationally bound structures. They are composed of dark matter halos, stars, remnants and the ISM, which itself is made up of dust and various phases of gas. The ISM may contribute a small fraction of the mass of a galaxy but in the context of regulating star formation it is important. Stars form in cold dense molecular regions (with temperatures of $\sim 10\,\mathrm{K}$ and densities of $10^2\,\mathrm{cm}^{-3}$ to $10^6\,\mathrm{cm}^{-3}$), which are concentrated around the spiral arms of galaxies. After formation they continuously feed energy, mass and gas enriched in heavy elements back into the ISM via stellar winds. High-mass stars emit radiation with energies high enough to ionise hydrogen. Miller and Cox (1993) modelled high-mass stars in a cloudy interstellar medium and found that the dilute portions of HII regions around O stars compose the warm ionised phase of the ISM. This phase (with temperatures of $\sim 8000\,\mathrm{K}$ and densities of $0.2\,\mathrm{cm}^{-3}$ to $0.5\,\mathrm{cm}^{-3}$) fills 20 % to 50 % of the volume of the Milky Way and therefore contributes significantly to the interstellar pressure. Stellar nucleosynthesis occurs during the life of stars, generating heavier and heavier elements. Upon a star's death heavy elements are ejected instantaneously into the ISM, along with more that are produced by the event itself. Supernovae generate turbulence in the ISM that contributes to the diversity of structure throughout galaxies. They produce very hot ($10^6\,\mathrm{K}$ to $10^7\,\mathrm{K}$) superbubbles of ionised gas, which makes

up the coronal gas phase of the ISM. The distribution of stars, interstellar material, chemical composition, and pressure all affect the overall dynamics of galaxies.

1.1.2 Giant Molecular Clouds

GMCs are the largest structures in the Galaxy. Star formation in the Galaxy is found to mostly occur in GMCs. Research on the dynamics of gas in these regions may therefore lead to an understanding of some galactic-scale statistical properties of star formation. Most of the mass of the ISM is concentrated in GMCs, which are large ($\sim 20\,\mathrm{pc}$ to $\sim 100\,\mathrm{pc}$) gaseous clouds of mass $> 10^4\,\mathrm{M}_\odot$ (McKee, 1999). Larson (1981) found that the clouds he studied are gravitationally bound and that cloud size is inversely proportional to density. He also found that the internal velocity dispersions of GMCs are proportional to a power of their size (~ 0.38), which is similar to the index predicted by Kolmogorov (1941) turbulence. These results can therefore be interpreted as evidence that supersonic turbulence is injected by large-scale kinetic energy cascades from large to small scales. Another piece of evidence for supersonically turbulent GMCs is that the volume-averaged densities in these objects are significantly lower than the densities found near star-forming sites, indicating clumpy media.

Theoretically, turbulence should decay in a time shorter than the lifetime of GMCs if the lifetime is assumed to be much longer than their freefall times. Turbulence therefore should not be observed as ubiquitously in GMCs as it is. It was first thought that magnetic fields could hamper the dampening of turbulence. Simulations of turbulent, self-gravitating, magnetically supercritical clouds were carried out by Avila-Reese and Vázquez-Semadeni (2001); Biskamp and Müller (2000); Mac Low et al. (1998); Padoan and Nordlund (1999); Pavlovski et al. (2006, 2002); Stone et al. (1998). These authors collectively found that magnetic fields cannot cushion the decay of supersonic turbulence. In order to maintain the view that GMCs are

quasi-equilibrium structures turbulence must be prolonged by some mechanism. Maron and Goldreich (2001) and Cho and Lazarian (2003) have shown that MHD (magneto-hydrodynamic) turbulence can decay slowly if there is strong cross-helicity (i.e. a high degree of turbulence imbalance) for compressible and incompressible fluids. Kritsuk et al. (2013) ran MHD simulations of the ISM and found that Larson's laws are reproduced via the process of turbulent energy cascade in which large-scale kinetic energy leads to supersonic turbulence on scales of 0.1 pc to 50 pc. According to Matzner (2002), other possible sources of turbulence are stellar winds, supernovae and, dominantly, HII regions. This idea was confirmed by simulations of driven turbulence via ionising radiation from O stars (Gritschneder et al., 2009; Li and Nakamura, 2006).

An alternative picture describes GMCs as non-equilibrium transient structures that form in a turbulent ISM via, for example, colliding flows that produce large-scale supersonic compressions in the warm neutral phase of the ISM. Colliding flows can occur between supernovae remnants, superbubbles and HII regions and form shock-compressed layers where the flows meet. The compressions are subject to non-linear thin-shell instabilities (Vishniac, 1994) and therefore are theorised to fragment into molecular clouds with supersonic turbulence (Koyama and Inutsuka, 2000, 2002). Clouds may be destroyed soon after the formation of stars that form on the order of a sound-crossing time, explaining why we almost always see turbulence in these clouds (it has not had enough time to decay). A longer discussion of GMC evolution can be found in Vázquez-Semadeni et al. (2006).

1.1.3 High-Mass Star Formation

High-mass star formation is not simply a scaled-up version of low-mass star formation. Radiative forces do not play a role in low-mass star formation but do for high-mass stars as they emit an intense rate of photons with a broad range of energies.

These photons can go on to dissociate molecules or, at even higher energies, ionise the surrounding gas thereby affecting the stellar environment. Unlike low-mass stars, emission from high-mass stars can accelerate nearby gas and dust that blow out cavities. High-mass stars also have a higher tendency to be dynamically ejected from their birthplace, as inferred by the number of observed runaways ($\sim 10\,\%$ to $25\,\%$), something that is rarely observed for low-mass stars. Dense cores have relatively more turbulent motions than less dense cores; high-mass stars tend to form in environments where turbulent motions dominate thermal motions (Caselli and Myers, 1995; Myers and Fuller, 1992). For more thorough reviews of high-mass star formation see Beuther et al. (2007) and Zinnecker and Yorke (2007).

High-mass stars begin their life in regions of HMSCs (high-mass starless cores) that are unstable to gravitational collapse. HMCs (high-mass cores) develop in these regions and accrete gas from the surrounding gas and dust until the growing protostellar object has mass $> 8\,\mathrm{M}_\odot$ after which it is termed a HMPO (high-mass protostellar object). Low-mass stars deviate in their evolutionary sequence here as they blow away their envelopes to become optically visible PMS (pre-main-sequence) stars. High-mass stars have no PMS phase; their Kelvin-Helmholtz timescales are short enough that they start fusing hydrogen atoms (thus starting their main-sequence phase) before they have finished accreting matter (Kahn, 1974). Stars that have finished accreting are termed final stars.

1.1.4 Spontaneous Star Formation

It is still not known how high-mass stars gather enough mass to form. These stars become luminous before they finish accreting and exert enough radiation pressure on the infalling gas to halt it altogether. This severely limits the upper mass limit of the IMF (Larson and Starrfield, 1971) and the lower the predicted accretion rate the higher the discrepancy with observations. There are three major types of models

that aim to explain the formation mechanism of high-mass stars: monolithic collapse (core accretion), competitive accretion and stellar collisions.

Core accretion assumes a process that is essentially a scaled-up version of the mechanism behind low-mass star formation; high-mass stars start as high-mass gravitationally bound cores. In other words, gas that will be accreted onto the star is gathered before the accretion phase begins. The mass of gas required to form a high-mass star is much larger than the Jeans mass, therefore there must be a mechanism for halting gravitational collapse until there is enough gas in the core. The turbulent core model proposed by McKee and Tan (2003) assumes that the high pressures in regions of supersonic turbulence can support a dense core from collapsing as it is forming. This model predicts that the accretion rate increases linearly with time.

Conservation of angular momentum of infalling gas should imply the formation of a disk around high-mass stars. Simulations that include multi-frequency continuum radiative transfer show that radiative acceleration is reduced in the plane of disks due to the "flashlight effect" (Krumholz et al., 2005; Yorke and Bodenheimer, 1999; Yorke and Sonnhalter, 2002). Krumholz et al. (2005) calculated the radiative transfer through dense disks accreting onto HMPOs and found that outflows evacuate optically thin polar cavities through which radiation can escape, significantly increasing the radiative flux along the polar axis and therefore reducing the radiation pressure on the disk. These results were backed up by the 3D radiation-hydrodynamic simulations of Cunningham et al. (2011) and by the simulations including self-gravity of Kuiper et al. (2011).

In the competitive accretion model stars in a cluster are competing for the available gas in their birth cloud. Accretion in this model is well described by the Bondi-Hoyle-Lyttleton accretion process (Bondi, 1952; Hoyle and Lyttleton, 1939), which has been studied numerically by Ruffert and Arnett (1994) and Ruffert (1994). Competitive accretion was analysed by Bonnell et al. (2001) who, via SPH (smoothed particle hydrodynamics) simulations, found that stars closer to the centre

of a cluster have higher accretion rates. Stars born close to the centre tend have a clear advantage in this model as gas from anywhere in the cloud will tend to fall towards the bottom of the cloud's potential well. A star that successfully increases its mass also increases its gravitational attraction and therefore improves its chances of accreting more gas. Early on in the formation of stars in this model there is a lot of available gas, and so stars born earlier are more likely to gather a substantial portion of it.

SPH simulations by Bonnell et al. (2011) show that a single cloud can produce clustered and distributed populations. Clustered populations formed in gravitationally bound regions with star formation efficiencies of $\sim 10\,\%$ and followed a full IMF. Competitive accretion was therefore found to be too efficient. However, the effects of radiative feedback and magnetic fields could suppress fragmentation and lead to lower efficiencies that are more consistent with observations. Distributed populations mostly formed in unbound regions with much lower star formation efficiencies ($\sim 1\,\%$) and were missing low and high-mass stars.

Stellar mergers can occur in dense clusters if the population of high-mass stars is dense enough i.e. if the time between stellar collisions is shorter than the timescale for stellar evolution (Hills and Day, 1976). In the monolithic collapse model massive stars are closely packed, so stellar collisions may occur and almost certainly will have an impact on star formation. This model was proposed before there were solutions to the radiation pressure problem. Now that there are, the area of research continues but has focused more on outliers such as blue stragglers (see Glebbeek et al., 2013, and references therein).

1.1.5 Triggered Star Formation

It was initially proposed by Elmegreen and Lada (1977) that spatially distinct co-eval OB subgroups in OB associations are the result of sequential self-propagating

triggered star formation via the collect and collapse model. The collect and collapse model (Dale et al., 2007; Elmegreen, 1998; Whitworth et al., 1994) starts with an expanding HII region, wind-blown bubble or supernova that drives a shock, sweeping up gas (the collect phase) until the shell becomes self-gravitating. At this point (the collapse phase) the shell becomes gravitationally unstable and shell fragmentation occurs. There is a lot of observational evidence for this process occurring (Preibisch and Zinnecker, 2007, and references therein). Massive star forming regions on the edges of expanding HII regions have also been observed (Deharveng et al., 2003; Zavagno et al., 2010; Zinnecker and Yorke, 2007, and references therein).

Cores could already exist where these expanding shock fronts are passing. Star formation can then be triggered by the sudden increase in external pressure introduced by the shock. Hennebelle et al. (2003) simulated cores that are embedded in a high pressure environment and found that "outside-in" collapse can ensue. It was also noted by this author that the increased external pressure is unlikely to be, as in their model, isotropic. For an anisotropic compression, the complex interaction of pressure waves within the core could instead lead to multiple systems, in which most stars are found (Mathieu, 1994). This idea was reinforced by Hennebelle et al. (2004) who simulated a rotating pre-stellar core. They found that material with high angular momentum collects at the disk edge faster than it can be redistributed via viscous torques leading to a Toomre instability. The resulting fragmentation can produce a few companion stars.

1.2 Ultra-Compact HII Regions

After the collapse of a dense molecular cloud, a high-mass star forms and begins emitting extreme ultra-violet radiation that ionises and heats the surrounding gas. The optical and near-infrared emission from such stars is not able to penetrate the natal clouds due to high column densities of dust. Radio free-free emission can,

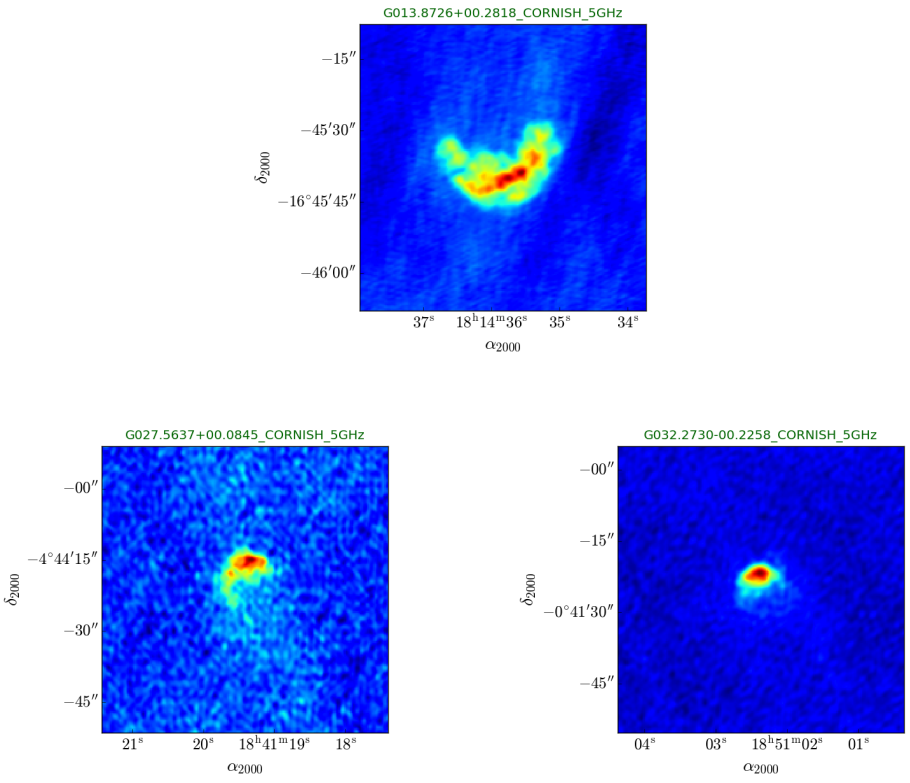

Fig. 1.1 Radio continuum images of cometary CORNISH UCHII regions.

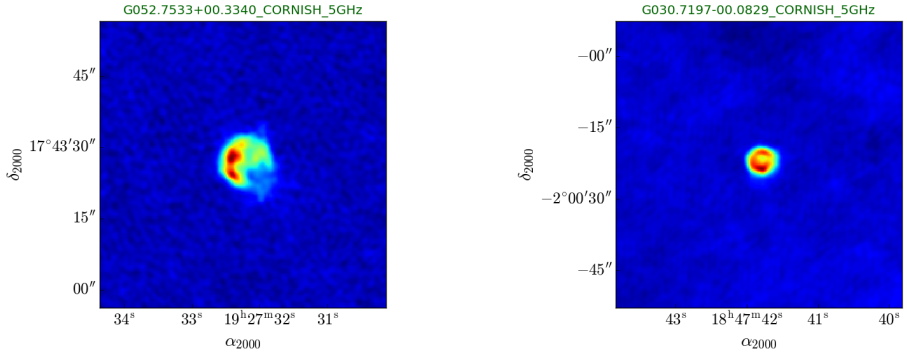

(a) Shell-like.

(b) Spherical.

(c) Irregular/multiply peaked.

(d) Unresolved.

Fig. 1.2 Radio continuum images of CORNISH UCHII regions.

however, be seen right across the Galaxy (Churchwell, 2002). At wavelengths in the far-infrared, emission coming from warm dust re-emitting the stellar radiation can also be observed from ionised nebulae (Cesaroni et al., 2015).

UCHII regions were first defined by Wood and Churchwell (1989b) as photo-ionised nebulae with diameters $\lesssim 0.1\,\mathrm{pc}$, electron number densities $\gtrsim 10^4\,\mathrm{cm}^{-3}$ and emission measures $\gtrsim 10^7\,\mathrm{pc\,cm}^{-6}$ that have not yet expanded out of their natal molecular cloud. The observed ionisation from such stars indicates that the ionising photon emission rates lie approximately between $10^{44}\,\mathrm{s}^{-1}$ and $10^{49}\,\mathrm{s}^{-1}$ corresponding to ZAMS stars with spectral types B2–O5. Wood and Churchwell (1989a) estimated the lifetime of UCHII regions ($\sim 4\times10^5$ yr) using the fraction of main-sequence stars observed in the UCHII phase and an adopted value for the main-sequence lifetime ($\sim 2.4\times10^6$ yr). This lifetime is an order of magnitude longer than that predicted by simple Strömgren sphere expansion ($\sim 4\times10^4$ yr), an inconsistency known as the lifetime problem. This conclusion was corroborated by Mottram et al. (2011), who used RMS (Red MSX Source) sources to calculate the UCHII region lifetime as a function of luminosity.

UCHII regions are interesting to study as they may provide a lot of information about the early life of massive stars including their properties and, due to a few morphological classes, their environments. The Wood and Churchwell (1989b) radio continuum survey included classifications of UCHII regions into morphological types: cometary ($\sim 20\,\%$), core-halo ($\sim 16\,\%$), shell ($\sim 4\,\%$), irregular or multiple peaked structures ($\sim 17\,\%$) and spherical and unresolved ($\sim 43\,\%$). Kurtz et al. (1994) made radio-continuum observations of 75 UCHII regions for which the proportions of morphological types agree remarkably well with those in Wood and Churchwell (1989b). Observed at higher spatial resolution, some apparently spherical morphologies uncover more ordered morphologies (Felli et al., 1984). The radio continuum survey of UCHII regions by Walsh et al. (1998) found that most sources were either cometary or irregular (ignoring the unresolved sources). De Pree et al.

(2005) revised the morphological scheme by adding the bipolar classification and removing the core-halo morphology. The latter was due to the fact that essentially all UCHII regions were observed to be associated with large-scale diffuse emission that could be separated from the compact cores. The proportions of the morphologies in this survey compare well with the Wood and Churchwell (1989b) and Kurtz et al. (1994) surveys except that 28 % of sources were classed as shell-like. Hoare et al. (2007) reviewed the different morphological surveys and noted that a lot of morphologies classified as shell-like could also be classified as cometary. Mac Low et al. (1991) pointed out that the proportion of cometary HII regions may be higher in reality as some other morphologies (shell-like and spherical) can be classed as a cometary viewed along the axis of symmetry.

1.3 Cometary UCHII Regions

As UCHII regions have had little time to significantly alter their natal environments, the morphologies that arise are thought to reflect the ambient density field. Cometary types in particular are interesting to study and to test numerical models against because they have a highly regular shape and can overcome the lifetime problem. In the past there were three major models that aimed to explain how UCHII regions form cometary shapes: the champagne flow model (Israel, 1978), the bow shock model (Van Buren and Mac Low, 1992; Mac Low et al., 1991; Reid and Ho, 1985) and clumpy/mass-loading models (Dyson et al., 1995; Redman et al., 1996; Williams et al., 1996). A more recent idea says that the situation is probably best described by a combination of these i.e. hybrid models (Arthur and Hoare, 2006).

1.3.1 Champagne Flow Model

Cometary HII regions are mostly observed at the edge of molecular clouds (e.g. the Orion Nebula). Along with the shape, this is the reason they were first named "blisters" (Israel, 1978). This led to the champagne flow model, a modification of the simple Strömgren solution in which the ionising star lies in an inhomogeneous (not a uniform) density field. The ionisation front propagates more rapidly through lower density gas, which explains the general shape of cometary HII regions. As the ionised gas is pressurised a shock develops ahead of the front that sweeps up a dense shell and traps the ionising radiation. At the same time ionised gas begins to flow down the density gradient, a feature that can be observed as relative Doppler shifts between lines from ionised and molecular gas.

Early modelling by Bodenheimer et al. (1979), Tenorio-Tagle (1979), Tenorio-Tagle et al. (1979), Whitworth (1979) and Bedijn and Tenorio-Tagle (1981) included discontinuities in density separating molecular clouds with the ISM. Bodenheimer et al. (1979) found that once the ionised gas reaches the edge of the dense cloud, it accelerates up to $\sim 30\,\mathrm{km\,s^{-1}}$. More realistically, Icke (1979a), Icke (1979b), Icke et al. (1980) and Yorke et al. (1983) modelled stars in density gradients, clearly reproducing cometary morphologies and predicting double peaked spectral line profiles corresponding to a velocity splitting of up to $50\,\mathrm{km\,s^{-1}}$ along the symmetry axis. Henney et al. (2005) carried out simulations of the photo-evaporation of a cloud with large-scale density gradients. They showed that an ionised flow is set up that has a transient phase with duration $\sim 10^4$ yr, which then becomes approximately stationary with respect to the ionisation front (the quasi-stationary phase) for a large part of its evolution.

Real HII regions cannot be explained entirely in terms of a density gradient. Not only does the champagne model fail to exhibit limb-brightened morphologies, but also the lifetime problem is not solved due to the unconstrained expansion of the

ionisation front. It also does not take into account that OB stars drive stellar winds that can significantly affect the dynamics of nearby gas.

1.3.2 Bow Shock Model

If an ionising star moves supersonically with respect to a uniform density field, the strong stellar wind driven by that star balances the ram pressure produced by the ambient flow, forming a bow shock ahead of the star. This model was introduced by Van Buren et al. (1990) as an alternative explanation of cometary HII regions and later analysed numerically by Van Buren and Mac Low (1992). They found that behind the bow shock neutral material is swept up into a very dense, thin shell that traps the expanding ionisation front. This was a good result for the bow shock model as it was known that a confining mechanism was necessary to solve the lifetime problem. Limb-brightening was also found to occur in this model and can be explained as ionised gas that has been compressed by the stellar wind into a thin shell, flowing around the stellar wind cavity.

Both Raga et al. (1997b) and Comeron and Kaper (1998) carried out two-dimensional axisymmetric hydrodynamical simulations of runaway OB stars that are driving strong stellar winds and found that bow shocks are unstable for a broad range of parameters. These stars are moving ($30\,\mathrm{km\,s^{-1}}$ to $100\,\mathrm{km\,s^{-1}}$) across the Galactic plane through the ISM and have ionised regions with sizes of $\sim 100\,\mathrm{pc}$, which fully encompasses the bow shock with sizes of $\sim 1\,\mathrm{pc}$ to $5\,\mathrm{pc}$. As the surrounding medium in these models is a lot less dense than that expected near dense molecular clouds the ionising radiation is not trapped. These results are therefore not fully applicable to bow shocks in UCHII regions.

The bow shock model was attractive because the size and shape compared well with observed cometary UCHII regions and it explained velocity gradients commonly seen at the head of cometaries.

1.4 Hybrid Models

Both the bow shock model and the champagne flow model have, however, been found to be inadequate in explaining the recombination line velocity structures. Lumsden and Hoare (1996) investigated the validity of both models in reproducing the velocity structure of the cometary UCHII region G29.96–0.02 and found that individually they poorly describe the object. Gaume et al. (1994) suggested that by including stellar winds and non-uniform ambient density fields more realistic models could be made.

A variety of hybrid models were investigated by Arthur and Hoare (2006) including champagne flow plus stellar wind and a combination of bow shock and champagne flow models in which the density gradient and the strength of the stellar wind were varied. With the inclusion of a stellar wind, it was discovered that it is possible for a champagne flow to produce limb-brightened morphologies. This is due to the fact that the stellar wind creates a dense shell that acts as a barrier to photo-evaporated flows, which divert around it. Arthur and Hoare (2006) found that for simple bow shock models the line widths are highest ahead of the massive star and for simple champagne flow models the widths are highest in the tail. They found that for hybrid models, a slow moving star in a steep density gradient has larger velocity widths toward the tail, but a fast moving star in shallow density gradients has its largest velocity widths nearer the star. Making sure to remove the effect of any cloud velocity, a hybrid model that matches the line data of a cometary HII region could be used to gather information about the density structure of the natal cloud.

Three-dimensional simulations of HII regions expanding off-centre in turbulent, self-gravitating power-law cores were run by Mac Low et al. (2007). They found that the expanding HII regions were roughly spherical and noted that this is consistent with the analytical results of Korycansky (1992). These results were also confirmed

by Arthur (2007) who performed similar simulations for r^{-2} and r^{-3} power-law density cores.

Very recently, deep hydrogen radio recombination line observations of the two cometary UCHII regions in DR 21 were presented with a detailed analysis of the velocity structure (Immer et al., 2014). The bow shock model seems to best describe one of the objects and it is believed a hybrid picture (in which UCHII regions in density gradient also exhibit stellar motion and/or a stellar wind) is required to explain the other.

1.5 Radio Continuum Surveys

Recently a huge effort has been made in mapping the Galactic plane to produce unbiased high-resolution, high-sensitivity surveys in order to understand our Galactic stellar population. Surveys over a wide range of wavelengths have been compiled so that massive stars and their environments, which they are interacting with, can be characterised by their SEDs.

There has been a lack of radio continuum surveys sufficiently high in resolution, sensitivity and coverage to compliment to these data sets until CORNISH. The CORNISH survey (Hoare et al., 2012; Purcell et al., 2013) is an arcsecond resolution 5 GHz radio survey of the northern half of the GLIMPSE region ($10° < l < 65°$, $|b| < 1°$) for compact ionised sources. CORNISH aims to provide an unbiased sample of UCHII regions that is insensitive to HCHII (hyper-compact HII) regions, which are even younger and more compact. At 5 GHz the survey observes at high enough frequency that it detects ionised gas that is optically thin, therefore allowing the structure of HII regions to be probed at high sensitivity. In figures 1.1 and 1.2 I show radio continuum maps of UCHII regions from the CORNISH sample and give their morphological classifications.

For a review on recent IR and radio surveys that have been or are in the process of being conducted, refer to Hoare et al. (2012) and Purcell et al. (2013).

Thesis Overview

In chapter 2 I describe my full numerical method, in which I detail how I simulated HII regions and observations of them. Next, in chapter 3, I present simulations of UCHII regions off-centre in power-law density environments and driving stellar winds. Chapter 4 contains the work I did on generating a Galactic population of UCHII regions that would be included in the CORNISH survey, and I compare the resulting distributions to the CORNISH data. Finally, in chapter 5, I conclude my thesis and suggest, for this area of research, possible avenues to be explored in the future.

Chapter 2

Numerical Methods

To simulate the coupled radiation-hydrodynamics (including additional heating and cooling due to atomic processes around HII regions) I used TORCH. TORCH is a 3D Eulerian fixed grid fluid dynamics code. The grid is a collection of finite volumes, called grid cells, that each hold fluid state information. The hydrodynamics are solved using a rotated hybrid HLL-HLLC Riemann solver to calculate fluxes on each grid cell face. Ionisation from point source radiation is implicitly solved and the column densities required for this are calculated via the method of short characteristics. Heating and cooling from atomic processes are calculated using the approximate functions in Henney et al. (2009).

To get second-order temporal accuracy while integrating the coupled hydrodynamics, radiation and cooling problems I use Strang Splitting (Strang, 1968). Without splitting the solution would be:

$$y(\vec{x},t+dt) = \mathscr{L}(dt)y(\vec{x},t) \tag{2.1}$$

where $y(\vec{x},t)$ is the solution at position $\vec{x}$ and time t and $\mathscr{L}(dt)$ is the solution operator acting over time-step dt. This problem is hard to solve unless it is decomposed (or split) into simpler sub-problems that are integrated separately. With the Strang-

Marchuk splitting scheme the solution is approximately given by:

$$y(\vec{x},t+dt) = \mathscr{L}_H(dt/2)\mathscr{L}_R(dt/2)\mathscr{L}_C(dt)\mathscr{L}_R(dt/2)\mathscr{L}_H(dt/2)y(\vec{x},t) \tag{2.2}$$

with subscripts H, R and C denoting hydrodynamics, radiation and cooling respectively. The order of the operators is shuffled each time step to ensure symmetry.

2.1 Hydrodynamics

Equations governing the dynamical behaviour of a fluid are found by first relating fluxes and conserved variables. The rate of change of a conserved variable in a volume is equal to its associated flux through the volume's boundary into or out of the volume plus any additional source of the variable (for example mass and energy injected by a star to produce a stellar wind). The equation is written, in integral form, as

$$\iiint_V \frac{\partial \vec{U}}{\partial t}\, dV + \oint_A \underline{\underline{F}} \cdot \hat{n}\, dA = \iiint_V \vec{S}\, dV\,, \tag{2.3}$$

where V denotes the volume, A is the bounding surface area, $\vec{U}$ is the vector of conserved variables, $\underline{\underline{F}}$ is the flux tensor, $\hat{n}$ is the unit vector normal to the surface pointing outwards, and $\vec{S}$ is the vector of source terms (the rate of production of each conserved variable in the volume).

The conserved variables are

$$\vec{U} = \begin{pmatrix} \rho \\ \rho u \\ \rho v \\ \rho w \\ e \\ \rho f \end{pmatrix}, \tag{2.4}$$

and the flux tensor is

$$\underline{\underline{F}} = \begin{pmatrix} \rho u & \rho v & \rho w \\ p+\rho u^2 & \rho uv & \rho uw \\ \rho uv & p+\rho v^2 & \rho vw \\ \rho uw & \rho vw & p+\rho w^2 \\ u(e+p) & v(e+p) & w(e+p) \\ \rho fu & \rho fv & \rho fw \end{pmatrix}, \tag{2.5}$$

where fluid density, pressure, velocity, energy density and HII fraction are given by ρ, p, $\vec{u}$, e and f respectively.

Using the divergence theorem we can write equation 2.3 as

$$\iiint_V \left(\frac{\partial \vec{U}}{\partial t} + \nabla \cdot \underline{\underline{F}} - \vec{S} \right) dV = \vec{0}, \tag{2.6}$$

where the divergence of the flux tensor is defined as (in Einstein notation):

$$\nabla \cdot \underline{\underline{F}} \equiv \frac{\partial F_{ij}}{\partial x_j}. \tag{2.7}$$

The integral in equation 2.6 is zero over any volume, therefore the integrand must also equal zero, leading us to the differential form of the conservation laws:

$$\frac{\partial \vec{U}}{\partial t} + \nabla \cdot \underline{\underline{F}} = \vec{S}. \tag{2.8}$$

2.1.1 Finite Volume Method

The FVM (finite-volume method) is a method by which the governing equations for a continuum can be solved on a meshed geometry. This method is highly accurate in modelling physical systems on length scales such that the system can be considered

continuous. For example, the discrete effects of atoms in a fluid are negligible when modelling on astronomical length scales.

TORCH uses the FVM to represent and solve equation 2.8 in conservative form. In 3D the problem domain is generally a cuboid that is discretised into small finite volumes (grid cells). Given the simple geometry of the grid cells it is far easier to start with equation 2.3. The surface integral is calculated as fluxes across the faces of each grid cell. Each grid cell has a constant $\vec{U} = \langle \vec{U} \rangle$ and $\vec{S} = \langle \vec{S} \rangle$ across its volume, which are just volume averages. This means equation 2.3 can be further simplified:

$$V \frac{\partial \langle \vec{U} \rangle}{\partial t} + \oint_A \underline{\underline{F}} \cdot \hat{n} dA = V \langle \vec{S} \rangle \,, \tag{2.9}$$

where V is the volume of the cell. Equation 2.9 is then solved for each finite volume after the fluxes have been calculated.

2.1.2 Godunov's Scheme

Godunov extended the ideas of section 2.1.1 to develop a first-order upwind finite-volume method. It is first-order in the sense that the conserved variables in each cell are uniform and the time integration of equation 2.9 is carried out with the first-order Forward Euler method. In a mesh containing a piece-wise constant distribution of data, for every pair of adjacent cells, the problem set-up is identical to that of the Riemann initial-value problem. Solving the Riemann problem across a cell interface in the mesh ensures the scheme is upwind because the states used in the computation of the fluxes are always found upstream. Godunov's scheme involves the use of an exact Riemann solver. However, its accuracy comes at the price of heavy computational load. This is why approximate solvers are prevalent in CFD (computational fluid dynamics) codes today.

We start with the one-dimensional scalar conservation equation,

$$\frac{\partial u(x,t)}{\partial t} + \frac{\partial f(x,t)}{\partial x} = 0\,, \tag{2.10}$$

which we want to solve on a one-dimensional mesh. The state at the mesh position i at time-step n in the mesh is given by

$$u(x,t) = u_i^n\,, \tag{2.11}$$

where $t = n\Delta t$. Applying the methodology in section 2.1.1 we get a source-less scalar one-dimensional version of equation 2.9:

$$\Delta x \frac{u_i^{n+1} - u_i^n}{\Delta t} = f_{i-1/2} - f_{i+1/2}\,, \tag{2.12}$$

where $f_{i-1/2}$ and $f_{i+1/2}$ are numerical fluxes that are calculated by a Riemann solver. The solution is given by

$$u_i^{n+1} = u_i^n + \frac{\Delta t}{\Delta x}\left(f_{i-1/2} - f_{i+1/2}\right)\,. \tag{2.13}$$

In three dimensions i, j and k are the mesh positions along the x, y and z directions respectively and if $\Delta u_i = u_i^{n+1} - u_i^n$ then we solve for split Riemann problems i.e. we solve in one dimension for all cell interfaces:

$$u_{ijk}^{n+1} = u_{ijk}^n + \Delta u_i + \Delta u_j + \Delta u_k\,. \tag{2.14}$$

For this scheme to be stable the time-step Δt in equation 2.13 must be

$$\Delta t \leq C_{\text{cfl}} \Delta x / S_{\max} \tag{2.15}$$

where $S_{\max}$ is the maximum wave speed in the simulation domain, and C_{cfl} is the maximum Courant number (for the purposes of my research $C_{\text{cfl}} = 1/2$ was a reliable choice). The maximum wave speed is calculated in TORCH as the maximum of bulk speeds plus the sound speeds in each cell in the simulation domain:

$$S_{\max} = \max\{|v| + a\}\,, \tag{2.16}$$

where v is a bulk velocity component and a is the sound speed in a cell. The physical interpretation of this constraint on the time-step is that if waves could cross more than one cell during this time then this information would be lost as only states to the left and right of an interface between two cells contribute in calculating the numerical flux.

2.1.3 Approximate Riemann Solvers

Practical computation of fluid dynamics often requires high resolution, spatially and temporally. Simulating at a sufficient resolution usually requires tens of thousands to millions of finite volumes and therefore interfaces, across each of which a Riemann problem is solved each time-step. The computational effort involved in carrying out this task is usually too high, so approximate solvers are used instead of highly accurate iterative Riemann solvers. Approximate Riemann solvers aim to reproduce important aspects of the solution whilst sacrificing some information (and therefore accuracy in the solution) for speed. These solvers fall into two groups: those that approximate the solution to the state; and those that approximate the fluxes across interfaces.

The Riemann Problem

A Riemann problem is an initial value problem in which there is a discontinuity between constant left and right states; the states of which are involved in conservation equations.

Harten–Lax–van Leer

The HLL approximate Riemann solver assumes a two wave configuration separating three constant states: the left and right Riemann states and the central "Star Region", which is the range of influence of the discontinuity via the left and right waves during a time-step (see figure 2.1). Intermediate waves are averaged out in the "Star Region" and any information about spatial variations here is lost. Consequently, this scheme can be very inaccurate when trying to model contact discontinuities, shear waves and material interfaces, introducing an unacceptable level of dissipation to the resolution of these features. Despite how diffusive this scheme is, it is robust to non-physical perturbations (which get smeared out before they can significantly alter the solution).

The entire scheme is given in Toro (1997), so only the flux calculations are shown here. The resulting flux depends on which direction the left-most and right-most waves are travelling:

$$\vec{F}_{\mathrm{HLL}} = \begin{cases} \vec{F}_{\mathrm{L}}, & \text{if } S_{\mathrm{L}} \geq 0\,, \\ \dfrac{S_{\mathrm{R}}\vec{F}_{\mathrm{L}} - S_{\mathrm{L}}\vec{F}_{\mathrm{R}} + S_{\mathrm{L}}S_{\mathrm{R}}(\vec{U}_{\mathrm{R}} - \vec{U}_{\mathrm{L}})}{S_{\mathrm{R}} - S_{\mathrm{L}}}\,, & \text{if } S_{\mathrm{L}} \leq 0 \leq S_{\mathrm{R}}\,, \\ \vec{F}_{\mathrm{R}}, & \text{if } S_{\mathrm{R}} \leq 0\,. \end{cases} \tag{2.17}$$

Harten–Lax–van Leer–Contact

An improvement was made to the HLL Riemann solver by including the contact wave (Toro, 1997). The HLLC Riemann solver assumes a three-wave structure

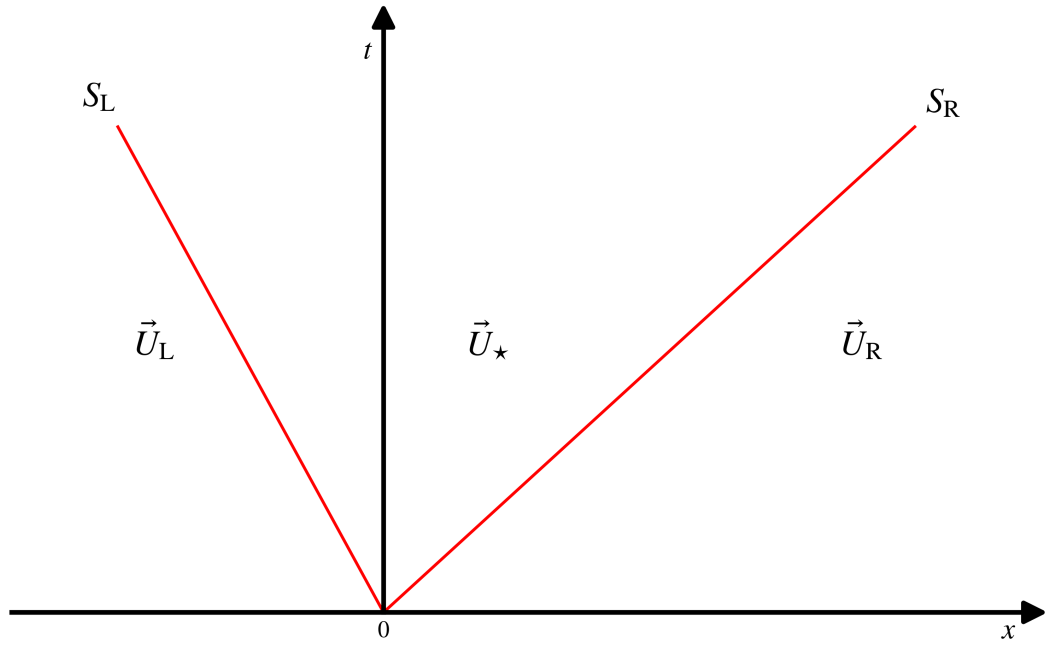

Fig. 2.1 A possible wave configuration that is resolved by the HLL Riemann solver. The solver assumes a two wave configuration separating three constant states. The solver calculates the numerical flux along $x = 0$ in order to update the conservative variables at an inter-cell boundary. The region between the two waves is called the Star Region (Toro, 1997) and is assumed to be a uniform average over the wave structure.

separating four states of which two are intermediate states (see figure 2.2). This scheme is much less diffusive and resolves contact discontinuities, shear waves and phase discontinuities accurately. Robustness suffers with this increase in accuracy, however, with unwanted flow fields (carbuncle instabilities) being produced at shocks aligned with the numerical grid.

Again, the full scheme is in Toro (1997) and the fluxes are given by

$$\vec{F}_{\mathrm{HLLC}} = \begin{cases} \vec{F}_{\mathrm{L}}, & \text{if } S_{\mathrm{L}} \geq 0\,, \\ \vec{F}_{\star\mathrm{L}}, & \text{if } S_{\mathrm{L}} \leq 0 \leq S_\star\,, \\ \vec{F}_{\star\mathrm{R}}, & \text{if } S_\star \leq 0 \leq S_{\mathrm{R}}\,, \\ \vec{F}_{\mathrm{R}}, & \text{if } S_{\mathrm{R}} \leq 0\,, \end{cases} \tag{2.18}$$

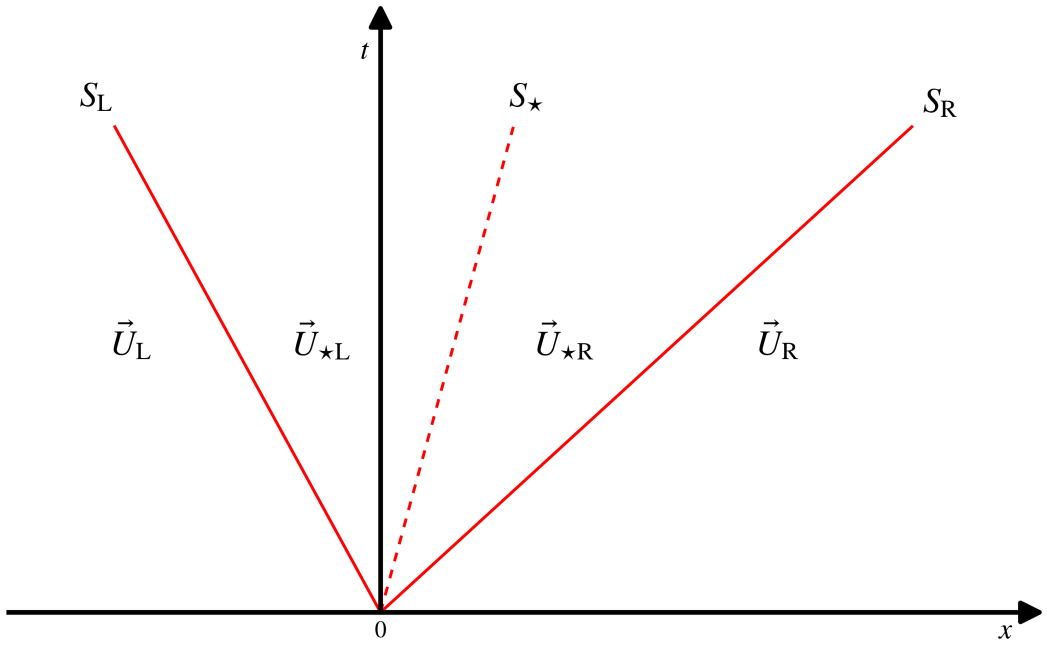

Fig. 2.2 A possible three-wave configuration that is resolved by the HLLC Riemann solver. The waves separate four constant states. The solver calculates the numerical flux along $x = 0$ in order to update the conservative variables at an inter-cell boundary. The region between the outer two waves is called the Star Region (Toro, 1997) and is split into two uniform average states by the middle wave $S_\star$.

with

$$\vec{F}_{\star \mathrm{K}} = \vec{F}_{\mathrm{K}} + S_{\mathrm{K}}(\vec{U}_{\star \mathrm{K}} - \vec{U}_{\mathrm{K}}), \tag{2.19}$$

where K is L or R and

$$\vec{U}_{\star \mathrm{K}} = \rho_{\mathrm{K}} \left(\frac{S_{\mathrm{K}} - u_{\mathrm{K}}}{S_{\mathrm{K}} - S_\star} \right) \begin{pmatrix} 1 \\ S_\star \\ v_{\mathrm{K}} \\ w_{\mathrm{K}} \\ \frac{E_{\mathrm{K}}}{\rho_{\mathrm{K}}} + (S_\star - u_{\mathrm{K}}) \left(S_\star + \frac{p_{\mathrm{K}}}{\rho_{\mathrm{K}}(S_{\mathrm{K}} - u_{\mathrm{K}})} \right) \\ f \end{pmatrix}. \tag{2.20}$$

The middle wave speed, $S_\star$, in the HLLC Riemann solver is obtained by first using the density component of equation 2.19 to get an equation for the left and right

star region densities:

$$\rho_{\star \mathrm{K}} = \frac{S_{\mathrm{K}} - u_{\mathrm{K}}}{S_{\mathrm{K}} - S_{\star}} \rho_{\mathrm{K}} \,. \tag{2.21}$$

We then find the pressures in the left and right star regions by using the linear momentum (in the direction perpendicular to the inter-cell boundary) term in equation 2.19:

$$p_{\star \mathrm{K}} = p_{\mathrm{K}} + (S_{\mathrm{K}} - S_{\star}) \rho_{\star \mathrm{K}} S_{\star} - (S_{\mathrm{K}} - u_{\mathrm{K}}) \rho_{\mathrm{K}} u_{\mathrm{K}} \,, \tag{2.22}$$

and substituting equation 2.21 to get

$$p_{\star \mathrm{K}} = p_{\mathrm{K}} + \rho_{\mathrm{K}} (S_{\mathrm{K}} - u_{\mathrm{K}})(S_{\star} - u_{\mathrm{K}}) \,. \tag{2.23}$$

Finally, we use the fact that the middle wave is a contact discontinuity i.e. $p_{\star \mathrm{L}} = p_{\star \mathrm{R}} = p_{\star}$, eliminate this term from the left and right equations in equation 2.23 and re-arrange to get the middle wave speed,

$$S_{\star} = \frac{p_{\mathrm{R}} - p_{\mathrm{L}} + \rho_{\mathrm{L}} u_{\mathrm{L}} (S_{\mathrm{L}} - u_{\mathrm{L}}) - \rho_{\mathrm{R}} u_{\mathrm{R}} (S_{\mathrm{R}} - u_{\mathrm{R}})}{\rho_{\mathrm{L}} (S_{\mathrm{L}} - u_{\mathrm{L}}) - \rho_{\mathrm{R}} (S_{\mathrm{R}} - u_{\mathrm{R}})} \,. \tag{2.24}$$

Rotated Hybrid HLL-HLLC

To solve equation 2.8 I first implemented a HLLC Riemann solver. After testing it was apparent that this scheme is not robust as unacceptable flow fields can result called carbuncle instabilities (Quirk, 1994). Schemes such as HLL and Rusanov (Rusanov, 1962) do not have this problem as they are highly dissipative. There are a few ways to cure schemes that are prone to the carbuncle phenomenon; the technique I decided to use was to combine HLL and HLLC schemes into a rotated-hybrid Riemann solver (Nishikawa and Kitamura, 2008).

The scheme starts by decomposing the geometric grid cell face normal $\vec{n}$ into two orthogonal directions:

$$\vec{n}_1 = \begin{cases} \dfrac{\Delta\vec{q}}{|\Delta\vec{q}|}, & \text{if } |\Delta\vec{q}| > \varepsilon\,, \\ \vec{n}_\perp, & \text{otherwise,} \end{cases} \tag{2.25}$$

and

$$\vec{n}_2 = \frac{(\vec{n}_1 \times \vec{n}) \times \vec{n}_1}{|(\vec{n}_1 \times \vec{n}) \times \vec{n}_1|}\,, \tag{2.26}$$

where $\Delta\vec{q} = (u_\mathrm{R} - u_\mathrm{L}, v_\mathrm{R} - v_\mathrm{L})$ is the velocity difference vector, $\vec{n}_\perp$ is a direction tangent to the geometric face and ε is a small number. The second case in equation 2.25 ensures that only the HLLC solver is used when streamwise velocity fields are smoothly varying; only at discontinuities will the HLL solver be applied. The flux across this grid cell face is

$$\vec{F} = \vec{n}\cdot\vec{n}_1\vec{F}_\mathrm{HLL}(\vec{n}_1) + \vec{n}\cdot\vec{n}_2\vec{F}_\mathrm{HLLC}(\vec{n}_2)\,. \tag{2.27}$$

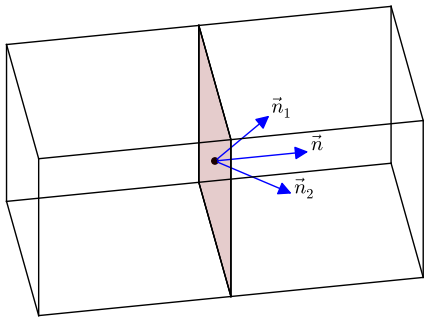

Fig. 2.3 Visualisation of the geometric grid cell face normal $\vec{n}$ decomposed into two orthogonal directions, $\vec{n}_1$ and $\vec{n}_2$, along which the Riemann problem is solved (with the HLL and HLLC Riemann solvers).

Fluxes $\vec{F}_\mathrm{HLL}(\vec{n}_1)$ and $\vec{F}_\mathrm{HLLC}(\vec{n}_2)$ are calculated by first finding the velocity in a new coordinate system:

$$\vec{v}' = \underline{\underline{R}}\vec{v}, \tag{2.28}$$

where $\vec{v}$ is the velocity in the original coordinate system on either the left or right side of the cell interface and $\underline{\underline{R}}$ is the rotation matrix (defined as rotating decomposed Riemann problem directions, $\vec{n}_1$ or $\vec{n}_2$, to align with the geometric cell face normal, $\vec{n}$).

Using the Rodrigues' rotation formula (Rodrigues, 1840) the rotation matrix $\underline{\underline{R}}$, which rotates unit vector $\vec{n}_i$ onto unit vector $\vec{n}$ is given by:

$$\underline{\underline{R}} = \underline{\underline{I}} + [\vec{w}]_\times + \frac{1-c}{s^2}[\vec{w}]_\times^2 , \tag{2.29}$$

where

$$\vec{w} = \vec{n}_i \times \vec{n} , \tag{2.30}$$

$$c = \vec{n}_i \cdot \vec{n} , \tag{2.31}$$

$$s = ||\vec{w}|| , \tag{2.32}$$

and $[\vec{w}]_\times$ is the skew-symmetric cross-product matrix of $\vec{w}$,

$$[\vec{w}]_\times = \begin{pmatrix} 0 & -w_3 & w_2 \\ w_3 & 0 & -w_1 \\ -w_2 & w_1 & 0 \end{pmatrix} . \tag{2.33}$$

With rotated left and right Riemann states for each decomposed Riemann direction we can now solve the one-dimensional Riemann problem. Solving these problems leaves us with momentum fluxes $\vec{L}'$ (calculated using $\vec{v}'$) that need to be rotated back onto the original coordinate system:

$$\vec{L} = \underline{\underline{R}}^{-1}\vec{L}' . \tag{2.34}$$

Along with the rest of the flux components, this gives us $\vec{F}_{\mathrm{HLL}}(\vec{n}_1)$ and $\vec{F}_{\mathrm{HLLC}}(\vec{n}_2)$. Using the rotated Riemann solver effectively applies the HLL solver in the direction normal to shocks (suppressing the carbuncle instability) and applies the HLLC solver across shear layers in order to minimise dissipation.

Liou (2000) argues that intermediate cells across a shock exchange information transversely to their neighbours along the shock, which can develop into a carbuncle instability. Considering a face connecting two neighbouring intermediate cells, any significant perturbation travelling in a direction normal to this face will lead to a velocity difference vector oriented in the same direction (Nishikawa and Kitamura, 2008). This means the HLL Riemann solver will introduce dissipation in this direction, suppressing the instability. The resulting scheme pays for its robustness with an acceptable drop in accuracy (using a dissipative Riemann solver) and speed (using two Riemann solvers).

2.1.4 Wave Speed Estimates

Consider the conservation laws in one dimension,

$$\vec{U}_t + \vec{F}(\vec{U})_x = \vec{0}. \tag{2.35}$$

Using the chain rule this can be written

$$\vec{U}_t + \vec{A}(\vec{U})\vec{U}_x = \vec{0}, \tag{2.36}$$

where

$$\underline{\underline{A}}(\vec{U}) = \frac{\partial \vec{F}}{\partial \vec{U}} \tag{2.37}$$

is the Jacobian matrix. Roe's method for approximately solving the Riemann problem (Roe, 1981) involves linearising equation 2.35 by finding a constant Jacobian matrix,

$\underline{\underline{\tilde{A}}}(\vec{U}_\mathrm{L}, \vec{U}_\mathrm{R})$, which preserves the hyperbolicity of the system, is consistent with the conservation laws and ensures conservation across discontinuities. Once the approximate linearised Riemann problem has been found i.e.

$$\vec{U}_t + \underline{\underline{\tilde{A}}}\vec{U}_x = \vec{0}\,, \tag{2.38}$$

it can be solved exactly (this is the basis of the Roe solver). The eigenvalues of $\tilde{A}$ are considered to be the wave speeds of this problem. TORCH uses the minimum and maximum of these wave speeds to approximate S_L and S_R in the HLL and HLLC Riemann solvers introduced in section 2.1.3:

$$\begin{aligned} S_\mathrm{L} &= \tilde{u} - \tilde{a} \\ S_\mathrm{R} &= \tilde{u} + \tilde{a}\,, \end{aligned} \tag{2.39}$$

where $\tilde{u}$ is the Roe-average bulk speed,

$$\tilde{u} = \frac{\sqrt{\rho_\mathrm{L}}u_\mathrm{L} + \sqrt{\rho_\mathrm{R}}u_\mathrm{R}}{\sqrt{\rho_\mathrm{L}} + \sqrt{\rho_\mathrm{R}}}\,, \tag{2.40}$$

and $\tilde{a}$ is the Roe-average sound speed,

$$\tilde{a} = \left[(\gamma - 1)(\tilde{H} - \frac{1}{2}\tilde{u}^2)\right]^{\frac{1}{2}}\,, \tag{2.41}$$

with the Roe-average of the enthalpy $H = (E + p)/\rho$ given by

$$\tilde{H} = \frac{\sqrt{\rho_\mathrm{L}}H_\mathrm{L} + \sqrt{\rho_\mathrm{R}}H_\mathrm{R}}{\sqrt{\rho_\mathrm{L}} + \sqrt{\rho_\mathrm{R}}}\,. \tag{2.42}$$

2.1.5 The MUSCL-Hancock Method

Suppose that there are two different initial conditions u_i^0 and v_i^0 such that

$$u_i^0 \geq v_i^0, \quad \forall i\,. \tag{2.43}$$

A scheme has the monotone property if

$$u_i^n \geq v_i^n, \quad \forall i \text{ and } \forall n\,. \tag{2.44}$$

Godunov's theorem (Godunov, 1959) states that a linear monotone scheme can at most be first-order accurate. Trying to construct higher spatial accuracy while preserving the monotone property will lead to Gibb's phenomenon i.e. spurious oscillations near high gradients (Bocher, 1906, 123–132). In order to get higher accuracy TORCH relaxes this stability condition such that the scheme does not have the monotone property but satisfies the TVD condition (Harten, 1983). If a scheme is written

$$u_i^{n+1} = u_i^n - C_{i-1/2}\Delta u_{i-1/2} + D_{i+1/2}\Delta u_{i+1/2}\,, \tag{2.45}$$

where $\Delta u_{i+1/2} = u_{i+1} - u_i$, then the scheme satisfies the TVD positivity condition if

$$0 \leq C_{i+1/2}, \quad 0 \leq D_{i+1/2}, \quad 0 \leq C_{i+1/2} + D_{i+1/2} \leq 1\,. \tag{2.46}$$

Satisfying the positivity condition implies that the total variation,

$$TV(u^n) = \sum_i \left| u_{i+1}^n - u_i^n \right|\,, \tag{2.47}$$

cannot increase,

$$TV(u^{n+1}) \leq TV(u^n)\,, \tag{2.48}$$

and the TVD condition implies monotonicity preservation:

$$u_{i+1}^0 \geq u_i^0, \quad \forall i \quad \Longrightarrow \quad u_{i+1}^n \geq u_i^n, \quad \forall i \text{ and } \forall n\,. \tag{2.49}$$

A method that is monotonicity-preserving prevents the generation of new local extrema in the solution and therefore will prevent spurious oscillations. Monotonicity addresses the stability in monotone solutions, but not in non-monotone solutions, something that TVD schemes do address (Laney, 1998).

TORCH uses the MUSCL (Monotonic Upstream-Centered Scheme for Conservation Laws) scheme of Van Leer (1979) to achieve second-order spatial accuracy in the solution. The method starts with the piece-wise constant distribution calculated in a previous time-step and linearly extrapolates these data to the boundaries where the Riemann problem is solved. This is done with primitive variables (i.e. density, pressure, velocities, etc.) because this has a useful consequence of keeping the sound speed piece-wise constant and leads to 2^D (where D is the number of dimensions) less expensive square root calculations per cell per time-step than if the conservative variables were extrapolated.

The boundary extrapolated primitive variables are:

$$\begin{aligned} q_i^{\mathrm{L}} &= q_i^n - \tfrac{1}{2}\phi\left(\frac{\Delta u_{i-1/2}}{\Delta u_{i+1/2}}\right)\frac{\Delta u_{i+1/2}}{\Delta x}\,, \\ q_i^{\mathrm{R}} &= q_i^n + \tfrac{1}{2}\phi\left(\frac{\Delta u_{i-1/2}}{\Delta u_{i+1/2}}\right)\frac{\Delta u_{i+1/2}}{\Delta x}\,, \end{aligned} \tag{2.50}$$

where $\phi(r)$ is a slope limiter. These are then readily converted to conserved variables u_i^{L} and u_i^{R} that form the right and left states of the Riemann problems on the left and right boundaries respectively. The numerical fluxes are

$$\begin{aligned} f_{i-1/2}^{\mathrm{MUSCL}} &= f(u_{i-1}^{\mathrm{R}}, u_i^{\mathrm{L}}) \\ f_{i+1/2}^{\mathrm{MUSCL}} &= f(u_i^{\mathrm{R}}, u_{i+1}^{\mathrm{L}})\,, \end{aligned} \tag{2.51}$$

so that the evolved state is

$$u_i^{n+1} = u_i^n + \frac{\Delta t}{\Delta x}\left(f_{i-1/2}^{\mathrm{MUSCL}} - f_{i+1/2}^{\mathrm{MUSCL}}\right). \tag{2.52}$$

In order to guarantee the algorithm is TVD it was found by Sweby (1984) that the slope limiter function in equation 2.50 must be of the form:

$$\phi(r) = 1 + \theta(r)(r-1), \tag{2.53}$$

where $0 \leq \theta(r) \leq 1$, and be bounded such that

$$0 \leq \left[\frac{\phi(r)}{r}, \phi(r)\right] \leq 2. \tag{2.54}$$

TORCH uses the van Albada slope limiter (Van Albada et al., 1982), which is TVD and symmetric:

$$\phi(r) = \frac{r^2 + r}{r^2 + 1}. \tag{2.55}$$

The limiter is plotted in a Sweby diagram in figure 2.4 along with the region bounded by equations 2.53 and 2.54.

2.1.6 Dirichlet Boundary Conditions

When calculating the fluxes across cell faces, a problem presents itself along the edges of the simulated domain. Equations 2.17 and 2.18 require states on the left and right of these edges. To deal with this, "ghost" cells have been placed outside these boundaries and their states calculated according to what boundary condition is imposed. Considering a boundary on the left side of the computational domain along the x direction the following give the boundary conditions.

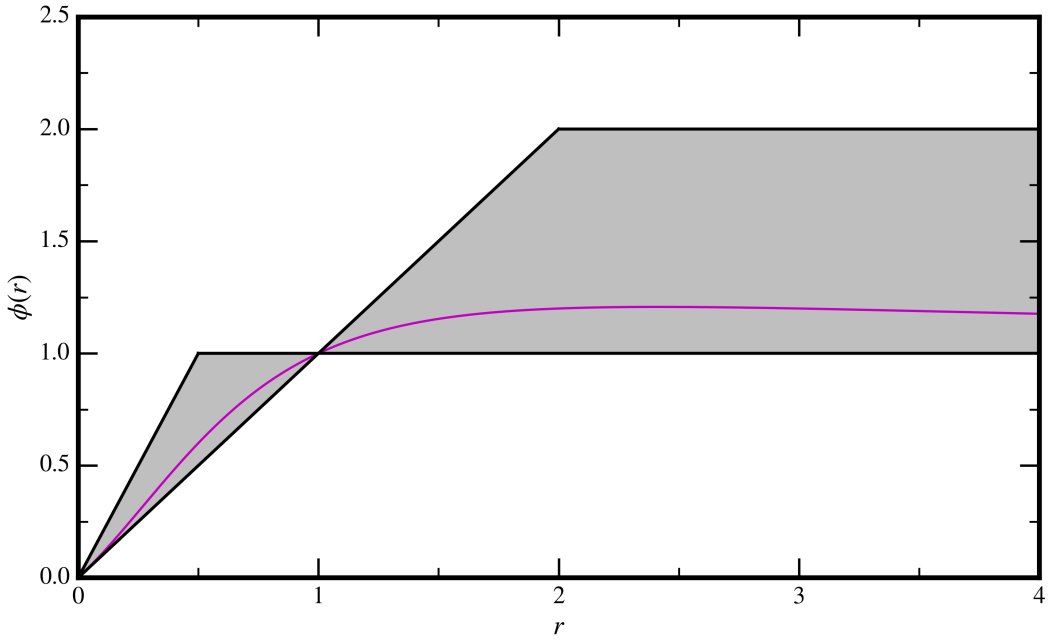

Fig. 2.4 Sweby diagram showing the region (shaded) within which a slope limiter must fit if the resulting scheme is to be second-order and TVD. The purple curve is the van Albada slope limiter used in TORCH.

Free

Free or transmissive boundary conditions allow waves to pass through without altering them.

$$\vec{U}_{\mathrm{L}} = \begin{pmatrix} \rho_{\mathrm{R}} \\ \rho_{\mathrm{R}} u_{\mathrm{R}} \\ \rho_{\mathrm{R}} v_{\mathrm{R}} \\ \rho_{\mathrm{R}} w_{\mathrm{R}} \\ E_{\mathrm{R}} \\ \rho_{\mathrm{R}} f_{\mathrm{R}} \end{pmatrix} \tag{2.56}$$

Reflective

Reflective boundary conditions are achieved by modelling an identical fluid moving in the opposite direction. The boundary acts like a mirror, reversing the sign of the component of velocity parallel to this boundary's normal.

$$\vec{U}_{\mathrm{L}} = \begin{pmatrix} \rho_{\mathrm{R}} \\ -\rho_{\mathrm{R}} u_{\mathrm{R}} \\ \rho_{\mathrm{R}} v_{\mathrm{R}} \\ \rho_{\mathrm{R}} w_{\mathrm{R}} \\ E_{\mathrm{R}} \\ \rho_{\mathrm{R}} f_{\mathrm{R}} \end{pmatrix} \tag{2.57}$$

2.1.7 Symmetry

In an axisymmetric grid the Cartesian coordinates in equation 2.8 are replaced with polar coordinates and a source term is added breaking the strictly conserved nature of a Cartesian grid (Falle, 1991). The "vector of conserved variables" will now include the radial momentum that is not a conserved quantity. The axisymmetric Euler equations look like

$$\frac{\partial \vec{U}}{\partial t} + \nabla \cdot \underline{\underline{F}} = \vec{S}, \tag{2.58}$$

where $\vec{S}$ is the source term to correct for the radial momentum's non-conserved nature:

$$\frac{\partial}{\partial t} \begin{pmatrix} \rho \\ \rho u_r \\ \rho u_z \\ E \\ \rho f \end{pmatrix} + \nabla \cdot \begin{pmatrix} \rho u_r & \rho u_z \\ p + \rho u_r^2 & \rho u_r u_z \\ \rho u_r u_z & p + \rho u_z^2 \\ u_r(E+p) & u_z(E+p) \\ \rho f u_r & \rho f u_z \end{pmatrix} = \begin{pmatrix} 0 \\ \frac{p}{r} \\ 0 \\ 0 \\ 0 \end{pmatrix}. \tag{2.59}$$

The source term comes from the difference between the radial divergence component and radial gradient term. For cylindrical coordinate system it is given by

$$\begin{aligned} S_r &= \frac{\partial(\rho u_r)}{\partial t} + \frac{1}{r}\frac{\partial(r\rho u_r^2 + rp)}{\partial r} + \frac{\partial(\rho u_z u_r)}{\partial z} \\ &= \frac{\partial(\rho u_r)}{\partial t} + \frac{1}{r}\frac{\partial(r\rho u_r^2)}{\partial r} + \frac{\partial(\rho u_z u_r)}{\partial z} + \frac{\partial p}{\partial r} + \frac{p}{r}, \end{aligned} \tag{2.60}$$

and the radial momentum fluid equation is

$$\frac{\partial(\rho u_r)}{\partial t} + \frac{1}{r}\frac{\partial(r\rho u_r^2)}{\partial r} + \frac{\partial(\rho u_z u_r)}{\partial z} + \frac{\partial p}{\partial r} = 0, \tag{2.61}$$

so that

$$S_r = \frac{p}{r}. \tag{2.62}$$

Similarly for a spherical coordinate system the source term is

$$\begin{aligned} S_r &= \frac{\partial(\rho u_r)}{\partial t} + \frac{1}{r^2}\frac{\partial(r^2\rho u_r^2 + r^2 p)}{\partial r} \\ &= \frac{\partial(\rho u_r)}{\partial t} + \frac{1}{r^2}\frac{\partial(r^2\rho u_r^2)}{\partial r} + \frac{\partial p}{\partial r} + \frac{2p}{r} \\ &= \frac{2p}{r}. \end{aligned} \tag{2.63}$$

When evaluating the source term for a grid cell it is obvious to note that it varies across the volume of the cell (it has a dependence on polar radius), therefore we average it over time and volume. For a cylindrical coordinate system:

$$\begin{aligned} \langle \vec{S} \rangle &= \frac{1}{V\Delta t}\int_{t=0}^{t=\Delta t}\int_{\phi=0}^{\phi=2\pi}\int_{z=z_c-\frac{\Delta z}{2}}^{z=z_c+\frac{\Delta z}{2}}\int_{r=r_c-\frac{\Delta r}{2}}^{r=r_c+\frac{\Delta r}{2}} \vec{S} r\, dr\, dz\, d\phi\, dt \\ &= \frac{2\pi p \Delta r \Delta z}{\pi \Delta z\left(\left(r_c+\frac{\Delta r}{2}\right)^2 - \left(r_c-\frac{\Delta r}{2}\right)^2\right)} \\ &= \frac{p}{r_c}, \end{aligned} \tag{2.64}$$

where r_c is the radius half-way between the inner and outer radii of the grid cell. The time and volume averaged source term in a spherical coordinate system is

$$\begin{aligned}\langle\vec{S}\rangle &= \frac{1}{V\Delta t}\int_{t=0}^{t=\Delta t}\int_{\phi=0}^{\phi=2\pi}\int_{\theta=0}^{\theta=\pi}\int_{r=r_c-\frac{\Delta r}{2}}^{r=r_c+\frac{\Delta r}{2}}\vec{S}r^2\,dr\,d\theta\,d\phi\,dt \\ &= \frac{4\pi\left[(r_c+\frac{\Delta r}{2})^2-(r_c-\frac{\Delta r}{2})^2\right]p}{V}.\end{aligned} \tag{2.65}$$

2.1.8 Parallelism

TORCH is a parallel code capable of running on many cores. Each core runs a simulation on a portion of the grid (which is split along one axis) and sends necessary data each time-step to cores that are simulating neighbouring grids. To integrate the hydrodynamics on a face the left and right states of a cell are needed to solve the Riemann problem. Along a boundary with a neighbouring grid, this information is received from the processing core that is simulating that grid and is copied into the "ghost" cells on that boundary. For the radiative transfer the processing core simulating the grid containing the star must ray trace the grid first before sending optical depth information across boundaries. In this way the cores with grids closer to the star simulate a time-step before cores with grids further away.

Parallel overhead is attributed to the memory for the extra "ghost" cells and the time taken to exchange this information. This becomes important (i.e. noticeably reduces the strong scaling efficiency) when the ratio of number of grid cells to number of processors is low. Coupling radiative transfer, heating/cooling and hydrodynamics has a big impact on the scalability of a simulation code. Operator splitting allows the hydrodynamics to be solved in parallel but the radiative transfer and heating/cooling is solved in serial because the ray casting scheme forces causal iteration over the cells. Therefore massive speed-up of simulations involving all these integrators should not be expected on a high number of processors. However, it can get close to

three times faster using a few processors, which was good enough for the purposes of this research.

2.2 Radiative Transfer

As a massive star is born within a dense molecular cloud, it will radiate photons with energies that lie above the ionisation threshold of hydrogen. The number of photons arriving at each cell in a numerical grid depends on the sum of the column densities of all cells between the ionising source and the target cell. Summing the column densities in this way to find the optical depth is called the method of long characteristics. This is the most accurate method, but ray tracing this way is computationally expensive. TORCH uses the short characteristics method, which is a much faster ray tracing scheme (with $O(N)$ time complexity, where N is the number of cells in the grid) as each cell derives its column density from the nearest neighbours between it and the ionising source.

2.2.1 Short Characteristics Ray Tracing

Each grid cell data structure holds a variable for the optical depth to the ionising source and one for the optical depth over the grid cell. The path length of the ray passing through the centre of the cell being ionised is given by

$$\Delta S = \sqrt{1 + \frac{(t_i - s_i)^2 + (t_j - s_j)^2}{(t_k - s_k)^2}} \Delta r \,, \tag{2.66}$$

where i, j and k are vector components, $\vec{t}$ is the target cell centre position vector, $\vec{s}$ is the source position vector and Δr is the physical width of the grid cell (see section A.1 for proof of equation 2.66). The kth direction is chosen such that

$$\hat{k} = \frac{\hat{n} \cdot (\vec{t} - \vec{s})}{|\hat{n} \cdot (\vec{t} - \vec{s})|} \,, \tag{2.67}$$

where $\hat{n}$ is the geometric normal to the grid cell face (pointing into the grid cell) that the ray crosses, entering the cell. The cell face has a normal parallel to the largest component of $|\vec{t} - \vec{s}|$ (which very simply finds the side of the grid cell the ray enters).

The optical depth over the cell is

$$\Delta\tau = n_{\rm HI}\sigma_\nu \Delta S\,, \tag{2.68}$$

where $n_{\rm HI}$ is the number density of neutral hydrogen atoms and σ_ν is the photo-ionisation cross-section. Depending on where the ray enters the target cell, the

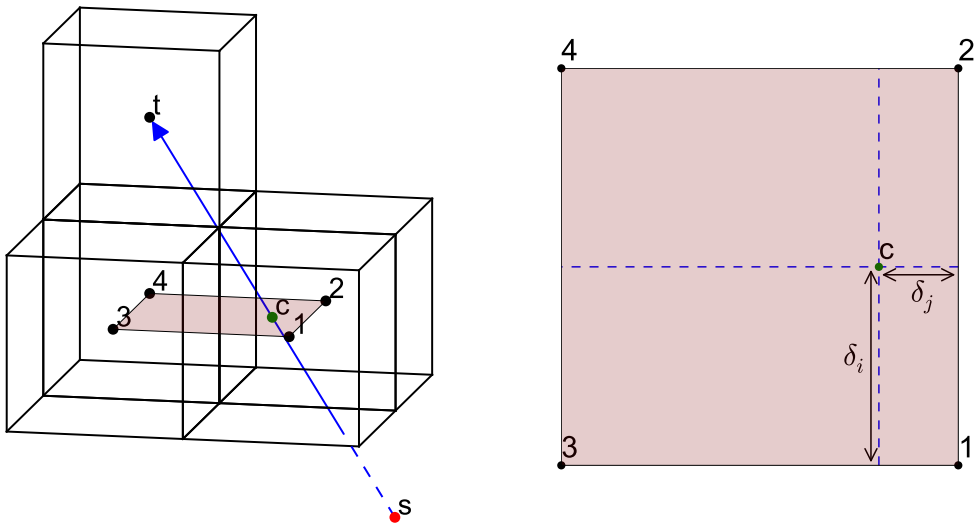

Fig. 2.5 This diagram shows a ray passing from the source (the red dot denoted by 's') passing through the interpolation plane (crossing at the green dot, 'c') to the centre of the target grid cell (black dot, 't'). Four nearest neighbours are chosen such that their cell centres (denoted by IDs 1-4) form corners of a square plane that the ray passes through. A bilinear interpolation is then performed, according to where the crossing point (green dot 'c') is on the square plane, to find the weight each nearest neighbour contributes to a weighted average of optical depths. The optical depth from source to target cell is then equal to this weighted average.

optical depth to the cell is given by a weighting of the nearest four neighbours around the ray just outside the cell (see figure 2.5 and the appendix in Mellema et al. (2006)).

Each weight is given by

$$\begin{aligned} w_1 &= \frac{\delta_i \delta_j}{\max(\tau_0, \tau_1 + \Delta\tau_1)} \\ w_2 &= \frac{(1-\delta_i)\delta_j}{\max(\tau_0, \tau_2 + \Delta\tau_2)} \\ w_3 &= \frac{\delta_i(1-\delta_j)}{\max(\tau_0, \tau_3 + \Delta\tau_3)} \\ w_4 &= \frac{(1-\delta_i)(1-\delta_j)}{\max(\tau_0, \tau_4 + \Delta\tau_4)}, \end{aligned} \tag{2.69}$$

where $\tau_0 = 0.6$, w_{ID} are the weightings associated with the neighbouring cells and $\delta_{i/j}$ are shown in figure 2.5. The optical depth to the target grid cell is

$$\tau = \frac{w_1(\tau_1 + \Delta\tau_1) + w_2(\tau_2 + \Delta\tau_2) + w_3(\tau_3 + \Delta\tau_3) + w_4(\tau_4 + \Delta\tau_4)}{\sum_{i=1}^{4} w_i}. \tag{2.70}$$

2.2.2 Implicit Integration Scheme

The explicit method takes the optical depths and therefore the photo-ionisation rate, Γ, to be constant during a time-step. Accuracy then depends on the time-step being small enough that the optical depths do not change appreciably, i.e. smaller than the ionisation front crossing time. The ionisation front can travel up to highly supersonic speeds so this constraint is much more limiting than the Courant condition. This means coupling with gas dynamics using this kind of scheme is very impractical.

TORCH uses the implicit integration scheme of Mellema et al. (2006), which ensures a high level of photon conservation and relaxes the time constraints an explicit method would have. The implicit scheme uses average values for the optical depths to work out a constant photo-ionisation rate to use over a time step and gives the exact solution if recombinations and collisions are not taken into account. If they are considered, the numerical solution is not exact but only deviates when the time-step is comparable to the recombination time. This is orders of magnitude longer than the minimum time-steps required in explicit schemes making this scheme ideal for coupling to fluid dynamics.

Photon Conservation

It was realised by Abel et al. (1999) that the spatial discretisation introduced in grid based simulations leads to a mismatch between photons entering a grid cell and the sum of the number of ionisations and photons leaving the cell. The local ionisation rate is given exactly by

$$\Gamma_{\rm local} = \frac{1}{4\pi r^2} \int_{\nu_{\rm th}}^{\infty} \frac{L_\nu \sigma_\nu e^{-\tau_\nu(r)}}{h\nu} {\rm d}\nu \,, \tag{2.71}$$

where r is the distance from the ionising source for hydrogen atoms with photo-ionisation cross-section σ_ν (Osterbrock, 1989), $\nu_{\rm th}$ is the Rydberg frequency, L_ν is the source's rate of energy output and $\tau_\nu(r)$ is the optical depth from source to the hydrogen atoms.

Grid cells do not have a single distance to the source; using the distance to the cell centre in order to calculate ionisation rates will not lead to a photon conserving scheme unless grid-cells are small enough to be considered optically thin. Abel et al. (1999) suggested that to deal with the range of distances in a grid cell, the ionisation rate must equal the photons absorbed by attenuation over the distance the ray travels through the target cell.

The fractional rate of neutral hydrogen atoms in a grid cell at distance r from the ionising source and thickness Δs that are ionised is given by the difference between the frequency photons enter, $\dot{N}^{\rm in}_{\rm cell}$, and exit, $\dot{N}^{\rm out}_{\rm cell}$, the cell divided by the number of neutral hydrogen atoms within the cell:

$$\Gamma = \frac{\dot{N}^{\rm in}_{\rm cell} - \dot{N}^{\rm out}_{\rm cell}}{n_{\rm HI} V_{\rm cell}} = \frac{\dot{N}^{\rm ion}_{\rm cell}}{n_{\rm HI} V_{\rm cell}} \,, \tag{2.72}$$

where $V_{\rm cell}$ is the volume of the cell and $\dot{N}^{\rm ion}_{\rm cell}$ is the ionisation rate within the cell. It is, however, hard to calculate $\dot{N}^{\rm ion}_{\rm cell}$ explicitly because it depends on the geometric factor $1/4\pi r^2$, which varies across the cell. In order to overcome this a spherical

shell is imagined centred on the source with radius equal to the distance to the cell centre and thickness equal to the cell crossing path length. The optical depth along all rays that reach the inner surface of the shell are equal to the optical depth along the path to the cell. Assuming the fraction of neutral hydrogen atoms within the shell is equal to that in the cell, this leads to a useful expression: the ratio of ionisation rates in the cell and shell are equal to the ratio of volumes respectively,

$$\frac{V_{\rm cell}}{V_{\rm shell}} = \frac{\dot{N}^{\rm ion}_{\rm cell}}{\dot{N}^{\rm ion}_{\rm shell}}\,, \tag{2.73}$$

where $V_{\rm shell}$ is given by

$$V_{\rm shell} = \frac{4\pi}{3}\left(\left(r+\frac{1}{2}\Delta S\right)^3 - \left(r-\frac{1}{2}\Delta S\right)^3\right)\,, \tag{2.74}$$

and ΔS is the length of the segment of ray passing through the cell.

Using equation 2.73 the fraction of the ionisation rate to the number of neutral hydrogen atoms can now be written

$$\Gamma = \frac{\dot{N}^{\rm in}_{\rm shell} - \dot{N}^{\rm out}_{\rm shell}}{n_{\rm HI}V_{\rm shell}}\,, \tag{2.75}$$

and, in terms of the optical depths, this is

$$\Gamma = \int_{\nu_{th}}^{\infty} \frac{L_\nu}{h\nu}\frac{e^{-\tau_\nu}(1-e^{-\Delta\tau_\nu})}{n_{\rm HI}V_{\rm shell}}{\rm d}\nu\,. \tag{2.76}$$

The explicit dependence on the geometrical factor is removed but remains implicitly through the volume of the shell.

The error in this approximation (for monochromatic photons) is:

$$\Delta\Gamma = \Gamma_{\rm local} - \Gamma \tag{2.77}$$

$$= \frac{1}{4\pi r^2} Q_{\rm Lyc}\sigma_\nu e^{-\tau_\nu} - Q_{\rm Lyc}\frac{e^{-\tau_\nu}(1-e^{-\Delta\tau_\nu})}{n_{\rm HI}V_{\rm shell}} \tag{2.78}$$

$$= \frac{Q_{\rm Lyc}e^{-\tau_\nu}}{4\pi r^2 \Delta S n_{\rm HI}} \left(\frac{\frac{1}{12}\left(\frac{\Delta S}{r}\right)^2 \Delta\tau + \frac{1}{2}\Delta\tau^2 - \frac{1}{6}\Delta\tau^3 + ...}{1+\frac{1}{12}\left(\frac{\Delta S}{r}\right)^2} \right), \tag{2.79}$$

where $Q_{\rm Lyc}$ is the rate of emission of Lyman continuum photons. The error tends to zero as $\Delta\tau \to 0$ and $\Delta S \ll r$. Even in the optically thick regime, with $\Delta\tau > 1$, the error is negligible as the photo-ionisation rate will be low.

Implicit Scheme Algorithm

The ionisation fraction of hydrogen evolves according to the rate of radiative ionisation, collisional ionisation and recombinations and is described by

$$\frac{{\rm d}f}{{\rm d}t} = (1-f)(\Gamma + n_{\rm e}C_{\rm H}) - f n_{\rm e}\alpha_{\rm H}\,, \tag{2.80}$$

where f is the ionisation fraction, $n_{\rm e}$ is the electron density, $C_{\rm H}$ is the collisional ionisation coefficient and $\alpha_{\rm H}$ is the recombination coefficient for hydrogen. We still take $C_{\rm H}$ and $\alpha_{\rm H}$ to be constant as in explicit integration schemes; we also take Γ and $n_{\rm e}$ to be constant but they represent time-averaged values as opposed to the values at the start of the time step. In this case, equation 2.80 has an analytical solution:

$$f(t) = f_{\rm eq} + \left(f_0 - f_{\rm eq}\right) e^{-t/t_{\rm i}}\,, \tag{2.81}$$

where

$$t_{\rm i} = \frac{1}{\Gamma + n_{\rm e}C_{\rm H} + n_{\rm e}\alpha_{\rm H}}\,, \tag{2.82}$$

and

$$f_{\rm eq} = \frac{\Gamma + n_{\rm e} C_{\rm H}}{\Gamma + n_{\rm e} C_{\rm H} + n_{\rm e} \alpha_{\rm H}} \,. \tag{2.83}$$

The time-averaged ionisation fraction is approximately

$$\langle f \rangle = f_{\rm eq} + \left(f_0 - f_{\rm eq} \right) \left(1 - e^{-\Delta t / t_{\rm i}} \right) \frac{t_{\rm i}}{\Delta t} \,. \tag{2.84}$$

All other time-averaged values can then be calculated by replacing variables with time-averaged constants. These then go on to iteratively find a new average ionisation fraction until the value has converged.

The radiative transfer module in TORCH uses the algorithm in the paper by Mellema et al. (2006). At each time-step the following is carried out:

1. Trace source rays to the cell and calculate the time-averaged and non-time-averaged optical depths.

2. Initialise the time-averaged and non-time-averaged HII fractions with values from the previous step (or with initial conditions).

3. Find the updated HII fraction and the time-averaged HII fraction.

   (a) Calculate the time-averaged electron density and photo-ionisation rate.

   (b) Use equation 2.84 to find the new time-averaged HII fraction.

   (c) Compare new time-averaged fraction with the time-averaged fraction from the previous step.

   (d) Repeat step 3 if the time-averaged HII fraction has not converged.

4. Calculate the non-time-averaged HII fraction using equation 2.81 and also the non-time-averaged and time-averaged cell optical depths.

5. Continue to the next cell in the causal list.

2.2.3 Causal Iteration

Iteration over cells in the grid data structure must be causal when solving for the HII fraction because the optical depth to a cell depends on the solved HII fraction of its contributing nearest neighbours. This means the neighbours that contribute to the optical depth to the cell must have their HII fraction solved first. If we were to use the optical depths of nearest neighbours from the previous time-step we would introduce a time-dependent discrepancy in the solution, which is more noticeable between cells close to the source and those far away. For explicit schemes this discrepancy is small because time-steps are small enough that the optical depths don't change appreciably.

An Iteration Algorithm

Here I present the way TORCH iterates causally over the grid. Firstly, given that the star is in the cell located at (i_s, j_s, k_s), there are eight starting positions: $\vec{b} = (i_s, j_s, k_s)$, $(i_s - 1, j_s, k_s)$, $(i_s, j_s - 1, k_s)$, $(i_s, j_s, k_s - 1)$, $(i_s - 1, j_s - 1, k_s)$, $(i_s - 1, j_s, k_s - 1)$, $(i_s, j_s - 1, k_s - 1)$ or $(i_s - 1, j_s - 1, k_s - 1)$. If any of these starting positions do not exist then ignore them e.g. in 2D the number of starting positions collapses to four (or less if the star is placed on a cell that is next to a boundary). Separately then there are eight sections of the grid that are to be traversed. Whether iteration should proceed in the positive or negative direction along an axis is determined by the sign of the corresponding component of

$$\vec{b} - (i_s - 0.5,\, j_s - 0.5,\, k_s - 0.5)\,. \tag{2.85}$$

The algorithm is then (for all eight starting positions):

1. Start at $\vec{b}$ and keep handles $\vec{h_j}$ and $\vec{h_k}$ that for now both point at $\vec{b}$.
2. From $\vec{h_j}$ iterate along the ith dimension until a grid boundary is reached.

3. Move $\vec{h}_j$ once along the jth dimension. If a cell exists there repeat step 2.
4. Move $\vec{h}_k$ once along the kth dimension and move $\vec{h}_j$ to the same position. If a cell exists there repeat step 2.
5. Finish.

2.2.4 R-type Expansion and Shadowing

Two tests were carried out to ensure the accuracy of the radiative transfer scheme. The first test compares the radius of a simulated Strömgren sphere (with no gas dynamics) with the analytical solution for the Strömgren radius (Strömgren, 1939):

$$R_{\rm st} = \left(\frac{3Q_{\rm Lyc}}{4\pi n_{\rm H}^2 \alpha_{\rm H}}\right)^{1/3} \left(1 - e^{-t/t_{\rm rec}}\right)^{1/3}, \tag{2.86}$$

where $n_{\rm H}$ is the number density of hydrogen atoms, $\alpha_{\rm H}$ is the total recombination rate and $t_{\rm rec}$ is the recombination time, which is given by

$$t_{\rm rec} = 1/n_{\rm H}\alpha_{\rm H}\,. \tag{2.87}$$

The results of this test are shown in figure 2.6 along with a comparison between first-order and second-order explicit schemes and the implicit scheme TORCH uses. Clearly the implicit scheme outperforms the other schemes, converging to the analytical solution in a time much smaller than the recombination time.

Simulations of UCHII regions with stellar winds should show trapping of the ionisation front behind the swept up wind bubble. To see if the code will work accurately in such a situation, the Strömgren sphere test was repeated but with a dense square clump positioned near the ionising source. The clump effectively blocks photo-ionising radiation from propagating into the "shadow" region. There is, however, some numerical diffusion into the shadow region, which would not be present if the method of long characteristics was implemented instead. This will

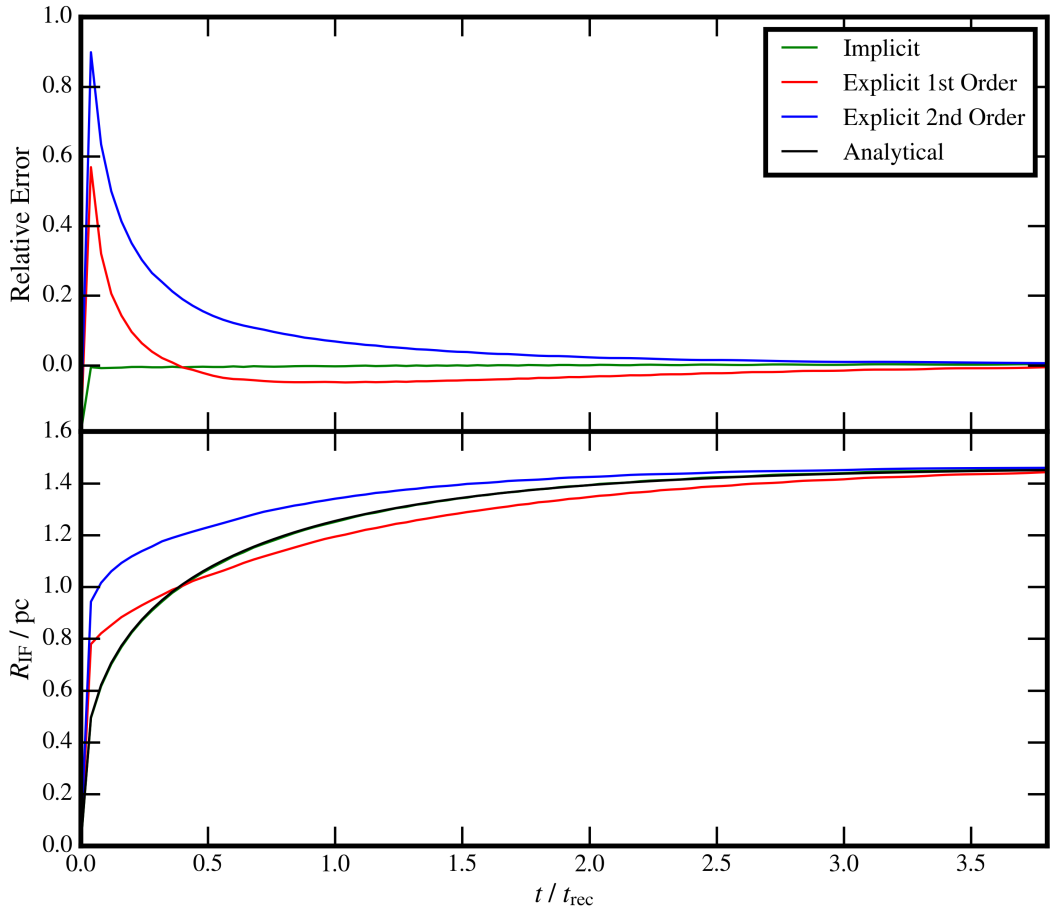

Fig. 2.6 Expansion of a HII region as a function of time in a uniform density environment. There is no coupling to the hydrodynamics. The black curve represents the analytical solution, which is partially obscured by the green curve (simulated with the implicit scheme).

have a negligible effect on the dynamics of any simulated HII region. Figure 2.7 shows the evolution of the ionised HII fraction in the shadow test.

2.2.5 D-type Expansion

Before developing a non-equilibrium heating/cooling module for TORCH, a simple thermal equilibrium model was used. Coupling between gas and radiation physics was achieved for an isothermal equation of state by setting the temperature of a gas

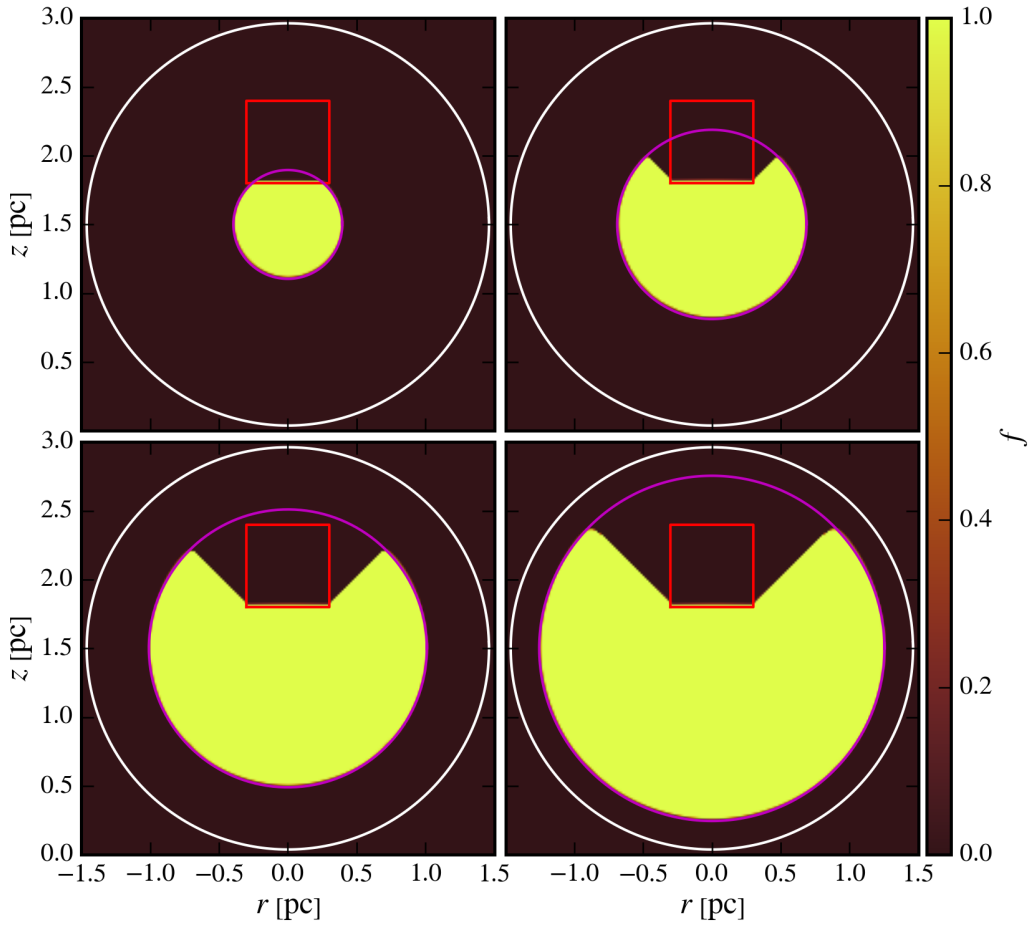

Fig. 2.7 HII fraction evolution in a uniform density medium with a dense square clump (in red) nearby. The magenta circle traces the analytical Strömgren sphere, which approaches the white circle as $t \to \infty$. The snapshots were taken at: 200 yr (top left); 5000 yr (top right); 10 000 yr (bottom left); and 20 000 yr (bottom right). The star was positioned at $(0\,\mathrm{pc}, 1.5\,\mathrm{pc})$ and the centre of the square clump (of side-length 0.6 pc) was positioned at $(0\,\mathrm{pc}, 2.1\,\mathrm{pc})$.

element according to the ionised fraction of hydrogen x in that element:

$$T = T_{\mathrm{HI}} + (T_{\mathrm{HII}} - T_{\mathrm{HI}}) f_{\mathrm{HII}}\,, \tag{2.88}$$

where T_{HI} is the temperature of fully neutral hydrogen and T_{HII} is the temperature of fully ionised hydrogen. With this scheme, I used the code to simulate D-type ionisation front expansion into an initially uniform density ($n_{\mathrm{H}} = 400\,\mathrm{cm}^{-3}$) isothermal gas. The ionising star in this simulation has a Lyman continuum photon rate

of $Q_{\rm Lyc} = 1.0 \times 10^{49}\,{\rm phot\,s^{-1}}$, which produces an initial Strömgren sphere of radius $R_{\rm st} = 1.25\,{\rm pc}$.

Early on in the evolution (a few recombination times) a weak-R ionisation front expands according to equation 2.86. The gas is heated to a temperature of 10^4 K so that the ionised region is overpressured with respect to the neutral gas. As the ionisation front slows down it becomes R-critical; the pressure wave overtakes the front and steepens into a shock wave, compressing the gas behind it. The R-critical ionisation front transitions into a D-critical front with an isothermal shock ahead of it. Expansion is then driven by the overpressure on the sound crossing time-scale $t_{\rm s} = R_{\rm st}/c_{\rm i}$, where $R_{\rm st}$ is the Strömgren radius given in equation 2.86 and $c_{\rm i}$ is the sound speed of the ionised gas.

Spitzer (1978) found that, if the ionised gas pressure is much higher than the pressure in the neutral gas and the neutral gas mass in the swept up shell is much greater than that in the ionised region, the ionisation radius evolves according to

$$R_{\rm spitzer} = R_{\rm st}\left(1 + \frac{7}{4}\frac{t}{t_{\rm s}}\right)^{4/7}. \tag{2.89}$$

According to Raga et al. (2012) this solution neglects the inertia of the expanding neutral material. Once included the solution is

$$R_{\rm raga} = R_{\rm st}\left(1 + \frac{7}{4}\sqrt{\frac{4}{3}}\frac{t}{t_{\rm s}}\right)^{4/7}. \tag{2.90}$$

A comparison between the simulated HII region expansion, equation 2.89 and equation 2.90 is shown in figure 2.8, which shows close agreement with the Raga solution. The relative error quickly drops below 5 % and remains so for the duration of the simulation.

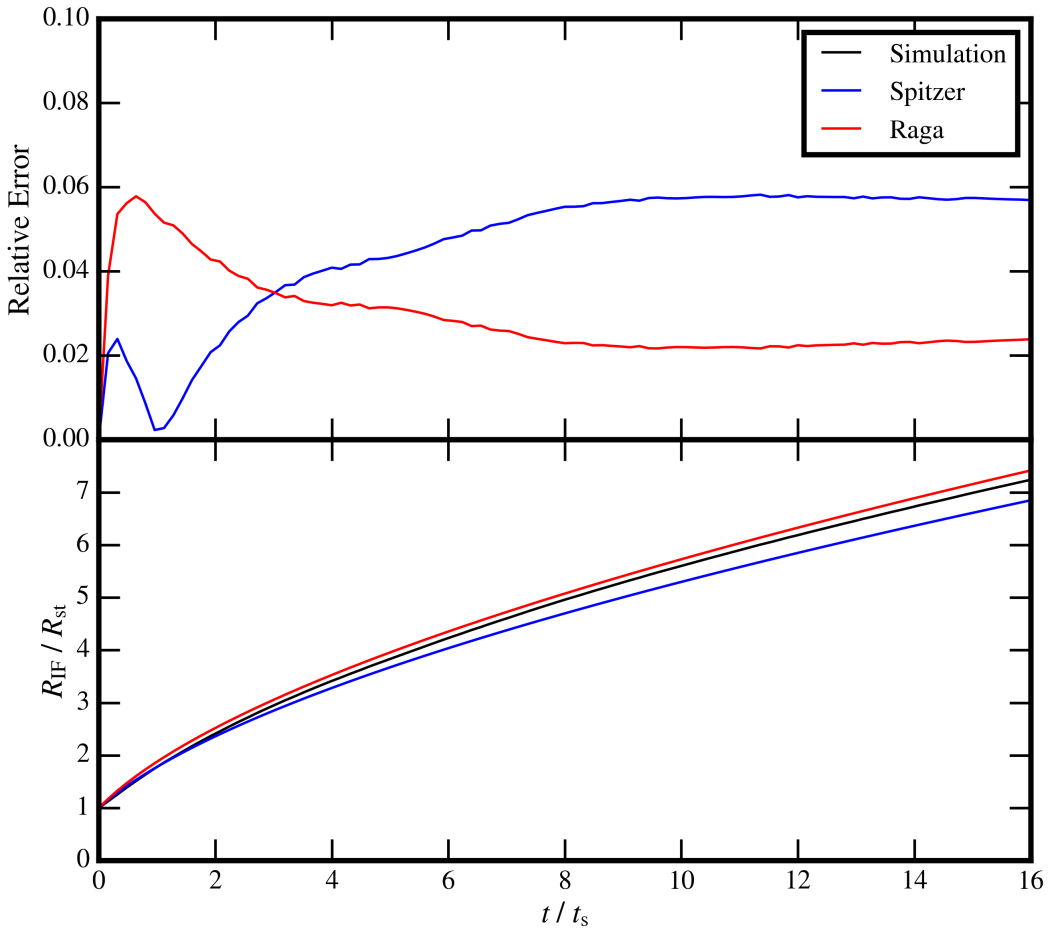

Fig. 2.8 Radius (bottom) and the relative error in the radius (top) of a HII region in a uniform density medium as a function of time in units of the sound crossing time t_s. The analytical solutions to the radius predicted by equations 2.89 and 2.90 are also plotted. Comparing to the Raga solution the relative error of the radius of the simulated HII region is below 5 % for $2 \leq t/t_s \leq 16$, and converges to an error of $\simeq 2\,\%$. The simulation was run on a $1000 \times 1 \times 1$ spherically symmetric grid.

2.2.6 Champagne Flow

A final test for the radiation transport module involves simulating a champagne flow. This model corresponds to Model A in Arthur and Hoare (2006) in which an ionising star, with an ionising photon rate of $Q_{\rm Lyc} = 2.2 \times 10^{48}\,{\rm s}^{-1}$, is embedded in an exponential density distribution where the density is $n_0 = 8000\,{\rm cm}^{-3}$ at the location of the star and the scale height is $H = 0.05\,{\rm pc}$. The density field is then

$$n_{\rm H} = n_0 \exp(z/H)\,, \tag{2.91}$$

where z is a polar coordinate and corresponds to the distance along the polar axis. The temperature of the ambient medium is $T_{\mathrm{HI}} = 300\,\mathrm{K}$ and the temperature of fully ionised gas is $T_{\mathrm{HII}} = 10^4\,\mathrm{K}$. Simulation snapshots are shown in figure 2.9 and figure 2.10; a photo-evaporated flow is set up and a parabolic-like ionisation front forms ahead of the star (up the density gradient). The results match those in Arthur and Hoare (2006) giving further evidence that the code works properly.

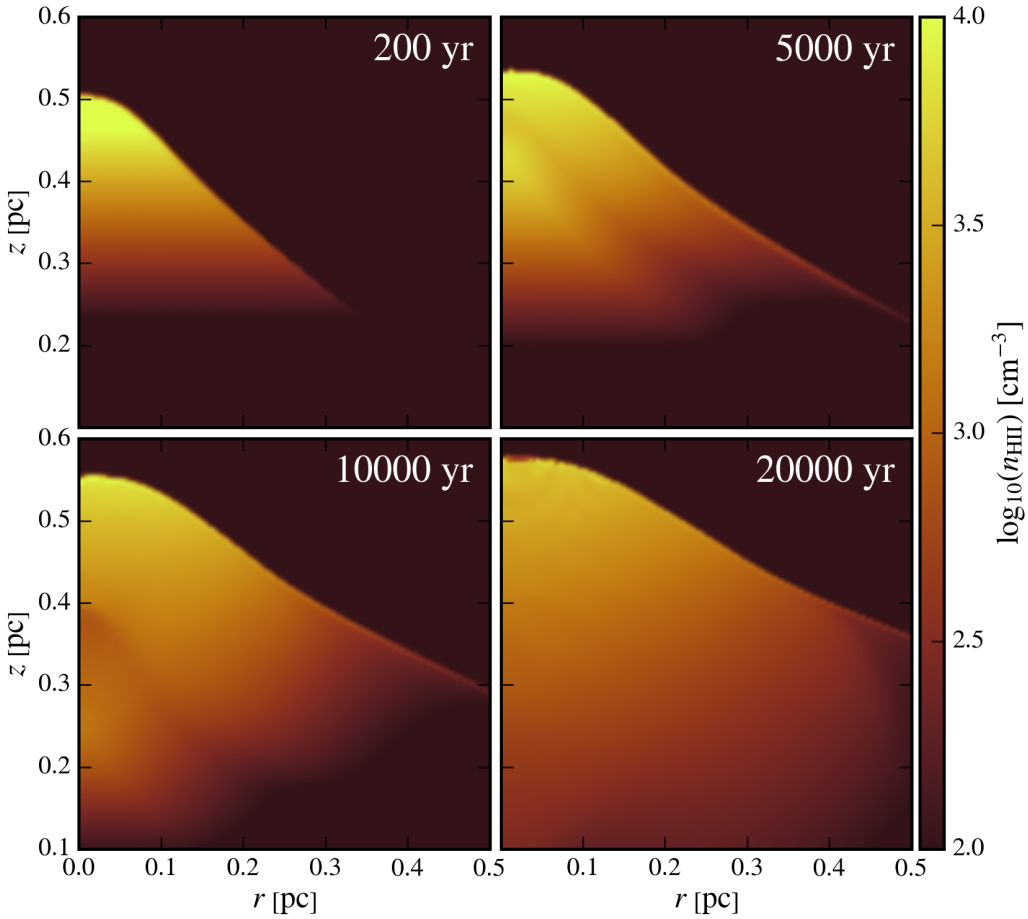

Fig. 2.9 Evolution of $\log_{10}$ of the ionised hydrogen number density n_{HII} resulting from an ionising source, located at the $r = 0\,\mathrm{pc}$ and $z = 0.45\,\mathrm{pc}$, in an exponential density gradient that is increasing along the positive z direction (see section 2.2.6.

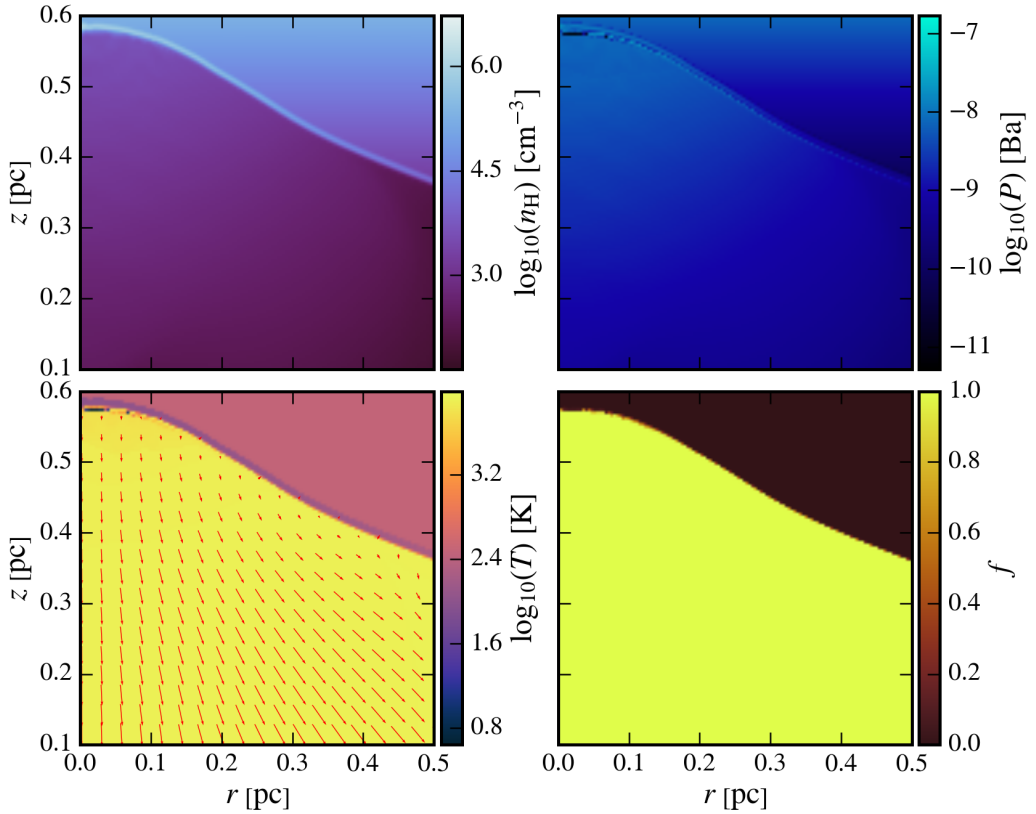

Fig. 2.10 Maps of hydrogen number density (top left), pressure (top right), temperature (bottom left) and hydrogen ionisation fraction (bottom right) of the champagne flow model described in section 2.2.6. The age of the exciting star is 20 kyr.

2.3 Heating and Cooling

The simple equilibrium heating/cooling code used in the previous section only works for an isothermal equation of state. In order to deal with general equations of state a non-equilibrium heating and cooling code was developed for TORCH using the fitting formulae in Henney et al. (2009). Unless specified otherwise the fitting formulae given here come from this author. We introduce a source term to the energy equation in equation 2.8 of $\dot{e} = H - C$. The rate of energy gained by the gas from processes that heat the gas is

$$H = H_{\mathrm{EUV}} + H_{\mathrm{FUV}} + H_{\mathrm{X}} + H_{\mathrm{IR}} + H_{\mathrm{CR}}\,. \tag{2.92}$$

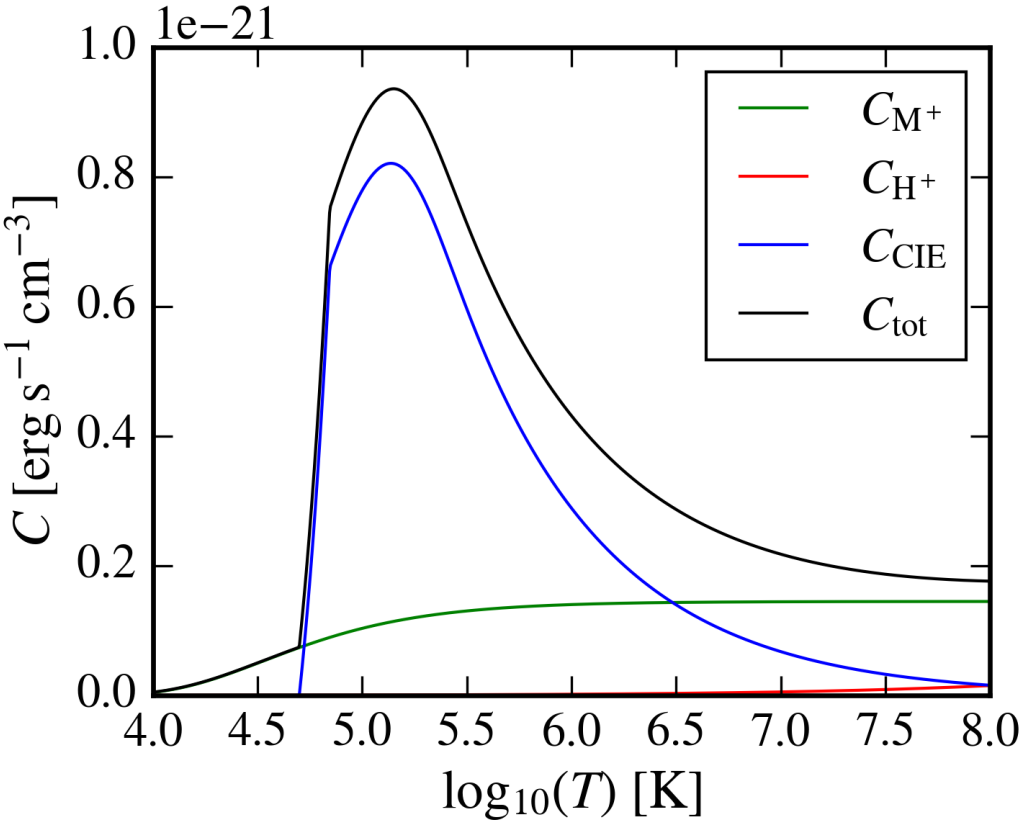

Fig. 2.11 Cooling rates in the hot shocked stellar wind region of model HII regions in section 3.2. To calculate these it was assumed that $n_{\mathrm{H}} = 1\,\mathrm{cm}^{-3}$ and $n_{\mathrm{e}} = n_{\mathrm{HII}} = n_{\mathrm{H}}$ in this region.

Using equation 2.76, the heating due to ionising EUV (extreme ultra-violet) photons is given by

$$H_{\mathrm{EUV}} = \int_{\nu_{\mathrm{th}}}^{\infty} (h\nu - h\nu_{\mathrm{th}}) \frac{L_\nu}{h\nu} \frac{e^{-\tau_\nu}(1 - e^{-\Delta\tau_\nu})}{V_{\mathrm{shell}}} \mathrm{d}\nu \,. \tag{2.93}$$

Heating due to non-ionising FUV (far ultra-violet) photons via dust absorption is approximately

$$H_{\mathrm{FUV}} = 1.9 \times 10^{-26} \frac{\left[\frac{n_{\mathrm{H}}}{\mathrm{cm}^{-3}}\right]^2 G_{0,h} e^{-1.9 A_{\mathrm{V}}}}{\left[\frac{n_{\mathrm{H}}}{\mathrm{cm}^{-3}}\right] + 6.4 G_{0,h} e^{-1.9 A_{\mathrm{V}}}} \quad \mathrm{erg\,s^{-1}\,cm^{-3}}\,, \tag{2.94}$$

where A_{V} is the extinction of the visual band frequencies in magnitudes and $G_{0,h} = \frac{G_0}{\mathrm{Habing}}$ is the unattenuated FUV photon flux in Habing flux units. The visual band

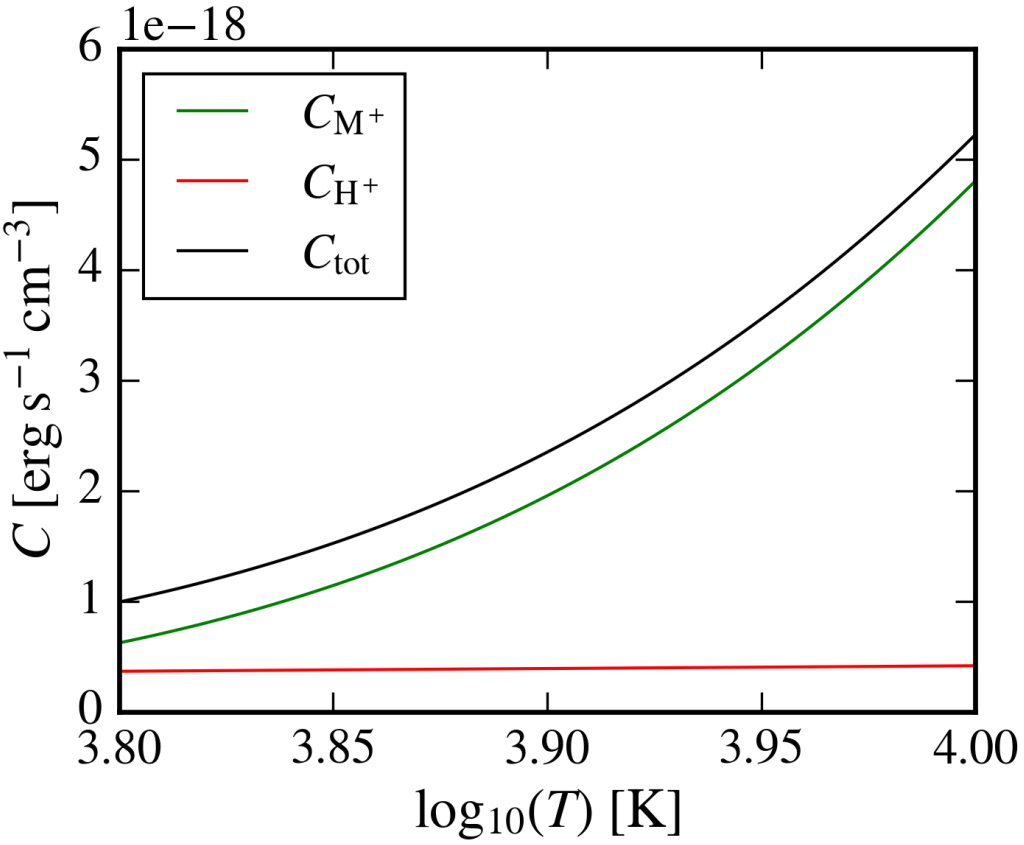

Fig. 2.12 Cooling rates in the ionised region of model HII regions in section 3.2. To calculate these it was assumed that $n_H = 0.1 \times 10^4\,cm^{-3}$ and $n_e = n_{HII} = n_H$ in this region.

extinction in magnitudes is

$$A_V = 1.086 \sigma_V N_H \quad \text{mag}\,, \tag{2.95}$$

where $\sigma_V = 5 \times 10^{-22}\,cm^2$ (Baldwin et al., 1991) and N_H is the column density of hydrogen atoms, which is calculated using the ray tracing scheme described in section 2.2.1. The unattenuated FUV photon flux is given by

$$G_0 = \frac{Q_{FUV}}{4\pi|\vec{r} - \vec{r}_\star|^2}\,, \tag{2.96}$$

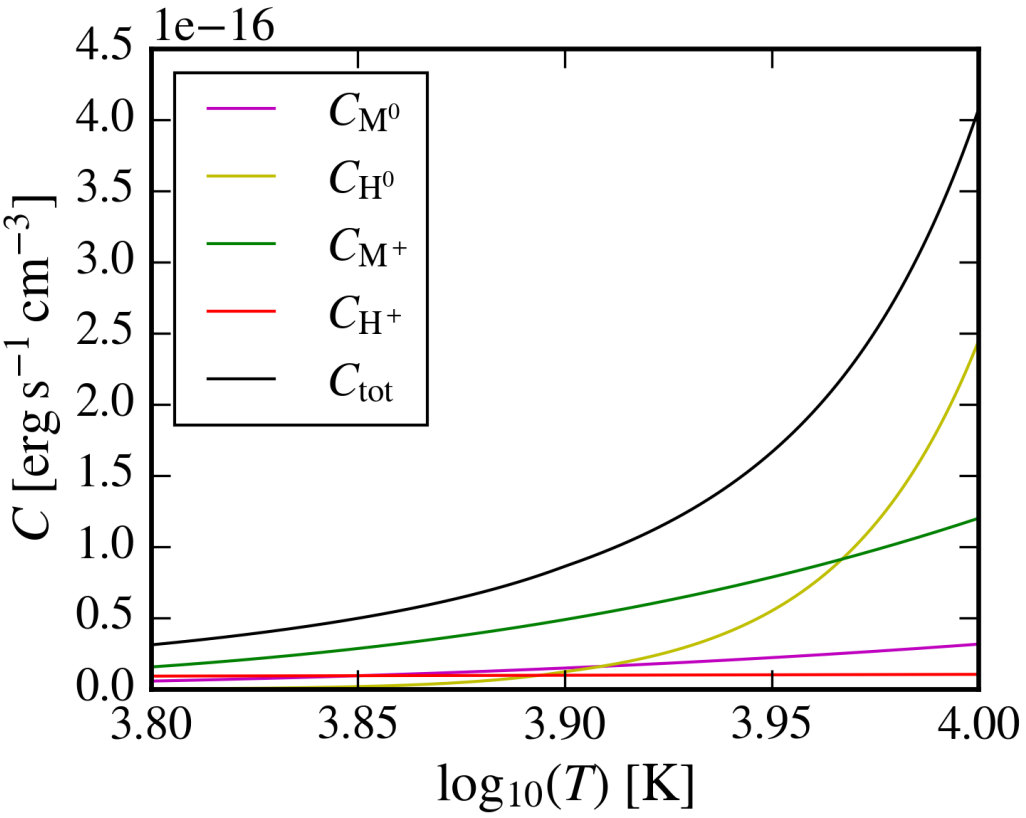

Fig. 2.13 Cooling rates in the ionisation front of model HII regions in section 3.2. To calculate these it was assumed that $n_H = 1 \times 10^4\,cm^{-3}$ and $n_e = n_{HII} = 0.5 n_H$ in this region.

where $|\vec{r} - \vec{r}_\star|$ is the distance to the star and Q_{FUV} is the star's rate of FUV photon emission (taken to be $Q_{FUV} = 0.5 Q_{Lyc}$ in the simulations carried out by TORCH). The rate of heating by hard X-rays is approximately

$$H_X = 6 \times 10^{-23} n_H F_X\,, \tag{2.97}$$

where F_X is the unattenuated x-ray photon flux from the star. Photons can be degraded to infra-red frequencies by dust grains and absorbed by the gas further from the star (this process is most efficient at high densities where the gas and dust grains are well

coupled):

$$H_{\rm IR} = 7.7 \times 10^{-32} \left[\frac{n_{\rm H}}{\rm cm^{-3}}\right] G_{0,h} \left(1 + \frac{n_1}{n_{\rm H}}\right)^{-2} e^{-0.05 A_{\rm V}} \quad {\rm erg\,s^{-1}\,cm^{-3}}\,. \tag{2.98}$$

The smallest contribution is from cosmic ray heating:

$$H_{\rm CR} = 5 \times 10^{-28} \left[\frac{n_{\rm H}}{\rm cm^{-3}}\right] \quad {\rm erg\,s^{-1}\,cm^{-3}}\,. \tag{2.99}$$

The rate of energy removed from the gas by processes that cool is

$$C = C_{\rm M^+} + C_{\rm M^0} + C_{\rm H^+} + C_{\rm H^0} + C_{\rm CIE} + C_{\rm PDR}\,. \tag{2.100}$$

The contribution to cooling from collisionally excited optical lines of ionised metals is

$$C_{\rm M^+} = a_1 z_{\rm O} \left[\frac{n_{\rm e}}{\rm cm^{-3}}\right] \left[\frac{n_{\rm HII}}{\rm cm^{-3}}\right] e^{-\left(\frac{T_1}{T} + \left[\frac{T_2}{T}\right]^2\right)} \quad {\rm erg\,s^{-1}\,cm^{-3}}\,, \tag{2.101}$$

where $a_1 = 2.905 \times 10^{-19}$, $T_1 = 33\,610\,{\rm K}$ and $T_2 = 2180\,{\rm K}$. Cooling due to collisionally excited lines of neutral metals is

$$C_{\rm M^0} = a_2 z_{\rm O} \left[\frac{n_{\rm e}}{\rm cm^{-3}}\right] \left[\frac{n_{\rm HI}}{\rm cm^{-3}}\right] e^{-\left(\frac{T_3}{T} + \left[\frac{T_4}{T}\right]^2\right)} \quad {\rm erg\,s^{-1}\,cm^{-3}}\,, \tag{2.102}$$

where $a_2 = 4.477 \times 10^{-20}$, $T_3 = 28\,390\,{\rm K}$ and $T_4 = 1780\,{\rm K}$. Hydrogen case B recombination cooling rates are calculated using cubic spline interpolation on the data in Hummer (1994):

$$C_{\rm H^+} = n_{\rm e} n_{\rm HII} k_{\rm B} T \beta_{\rm B}\,, \tag{2.103}$$

where $\beta_{\rm B}$ is the case B energy-loss coefficient. The collisional excitation cooling rate of neutral hydrogen is also calculated using cubic spline interpolation but on

data in Raga et al. (1997a):

$$C_{\mathrm{H}^0} = n_{\mathrm{e}} n_{\mathrm{HI}} k_{\mathrm{B}} T q(T)\,, \tag{2.104}$$

where $q(T)$ is the collisional excitation rate coefficient. The collisional ionization equilibrium-cooling curve for gas temperatures $T > 50\,000\,\mathrm{K}$ (mainly from highly ionized metals) is approximately:

$$C_{\mathrm{CIE}} = a_3 z_{\mathrm{O}} \left[\frac{n_{\mathrm{e}}}{\mathrm{cm}^{-3}}\right] \left[\frac{n_{\mathrm{HII}}}{\mathrm{cm}^{-3}}\right] \left[\frac{T}{\mathrm{K}}\right]^{-0.63} \left(1 - e^{-\left[\frac{T}{10^5 K}\right]^{1.63}}\right) \quad \mathrm{erg\,s^{-1}\,cm^{-3}}\,, \tag{2.105}$$

where $a_3 = 3.485 \times 10^{-15}$. The contribution from collisional line cooling of highly ionised metals and neutral/molecular gas is approximately:

$$C_{\mathrm{PDR}} = 3.981 \times 10^{-27} \left[\frac{n_{\mathrm{H}}}{\mathrm{cm}^{-3}}\right]^{1.6} \left[\frac{T}{\mathrm{K}}\right]^{0.5} e^{-T_0(n_{\mathrm{HI}})/T} \quad \mathrm{erg\,s^{-1}\,cm^{-3}}\,, \tag{2.106}$$

where

$$T_0(n_{\mathrm{HI}}) = 70 + 220 \left[\frac{n_{\mathrm{HI}}}{10^6\,\mathrm{cm}^{-3}}\right]^{0.2} \quad \mathrm{K}\,. \tag{2.107}$$

The cooling rates in the hot shocked stellar wind region, the ionised region, and the ionisation front of a typical HII region are shown in figure 2.11, figure 2.12, and figure 2.13 respectively. It should be pointed out that the recombination cooling term, equation 2.103, in figure 2.11 is extrapolated beyond $T > 1 \times 10^7\,\mathrm{K}$ as this is the maximum temperature available from Hummer (1994).

2.3.1 Sub-cycling

Due to the operator split nature of TORCH, the module with the shortest time-step can bottleneck the integration. The energy gained/lost in a grid cell from heating and cooling processes is limited to 10 % of the existing energy in the cell. This can end up being quite a lot smaller than the time-steps calculated from radiation transport and

hydrodynamics. One remedy is to use sub-cycling: integrate the heating and cooling in small sub-steps until the minimum time-step from radiation hydrodynamics is reached. The coupling error will still be higher than if sub-cycling was not used but the integration will be a lot faster (which is preferable).

The heating/cooling rate at the start of the time-step is

$$\dot{E}_0 = \frac{dE}{dt}(t=0) = H - C(T_0)\,, \tag{2.108}$$

where T_0 is the temperature at the beginning of the time-step and it is assumed that the neutral and ionised density fields do not evolve throughout this procedure. The limiting time-step for the heating/cooling sub-problem is

$$\Delta t_{\mathrm{C}} = \frac{0.1E_0}{\dot{E}_0}\,. \tag{2.109}$$

The limiting time-step from the radiation and hydrodynamics sub-problems is Δt_{RH} so the number of sub-cycling steps is

$$N = \begin{cases} \left\lfloor \frac{\Delta t_{\mathrm{RH}}}{\Delta t_{\mathrm{C}}} \right\rfloor\,, & \text{if } \frac{\Delta t_{\mathrm{RH}}}{\Delta t_{\mathrm{C}}} - \left\lfloor \frac{\Delta t_{\mathrm{RH}}}{\Delta t_{\mathrm{C}}} \right\rfloor = 0\,, \\ \left\lfloor \frac{\Delta t_{\mathrm{RH}}}{\Delta t_{\mathrm{C}}} \right\rfloor + 1\,, & \text{otherwise}\,. \end{cases} \tag{2.110}$$

The sub-cycling time-step is then $\Delta t_{\mathrm{sub}} = \Delta t_{\mathrm{RH}}/N$. Iterating from $i = 0$ to $i = N-1$ we carry out these calculations:

$$\begin{aligned} T_i &= T(E_i)\,, \\ \dot{E}_i &= H - C(T_i)\,, \\ E_{i+1} &= E_i + \Delta t_{\mathrm{sub}}\dot{E}_i\,, \end{aligned} \tag{2.111}$$

and finally the total heating/cooling rate in the full time-step Δt_{RH} is

$$\dot{E} = \frac{E_N - E_0}{\Delta t_{\mathrm{RH}}}. \tag{2.112}$$

2.3.2 Wind-Blown Bubble

Stellar winds are important to consider when dealing with UCHII regions as they greatly influence the dynamics. Wind-blown bubbles are useful objects to simulate as their evolution is well described in the literature and so can highlight possible problems with the heating/cooling module. The model I used when simulating a bubble is almost identical to one of the scenarios set out in Strickland and Stevens (1998). A stellar wind with mass loss rate $\dot{M}_W = 5 \times 10^{-5}\,\mathrm{M}_\odot\,\mathrm{yr}^{-1}$ and terminal wind speed $v_W = 2000\,\mathrm{km\,s}^{-1}$ was modelled by including source terms $\dot{\rho}_W$ and $\dot{e}_W$ within a radius of 10 grid cells. The source terms are, respectively, the mass loss rate and mechanical luminosity $L_W = \frac{1}{2}\dot{M}_W v_W^2$ both divided by the volume of the region they are added to.

As was found in Strickland and Stevens (1998) the wind sweeps material into a shock-heated shell. The shell starts out thick, but rapidly cools and collapses as it grows. Eventually the shell is so thin that it becomes unstable to thin shell and Vishniac instabilities (Vishniac, 1983). The evolution of the ionised hydrogen number density during the simulation is shown in figure 2.14 and agrees well with the model in Strickland and Stevens (1998).

2.3.3 Shadowing Instability

This final test utilises both the radiation and cooling modules in order to reproduce the shadowing instability (Williams, 1999). A wind was set-up in the same way as in section 2.3.2 with wind, star and initial gas parameters taken from the shadowing instability test in Arthur and Hoare (2006). If the cooling time is too short the

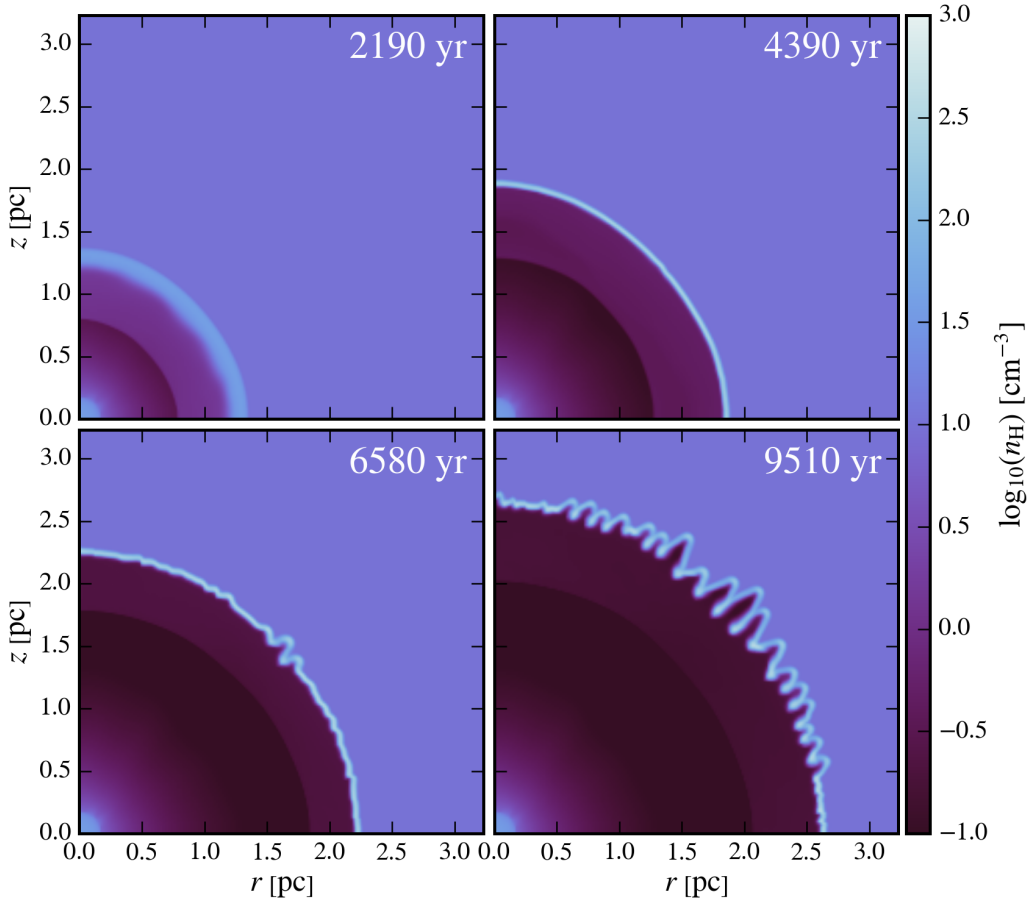

Fig. 2.14 Snapshots of $\log_{10}$ of the hydrogen number density n_H taken during a simulation of a wind-blown bubble.

dense swept-up shell can collapse while the effects of the staggered grid are still appreciable (i.e. the shell has a low resolution). For this reason the energy flux from the heating and cooling module was artificially reduced by a factor of 100 in order to increase the cooling length and so delay the onset of the cooling instability.

Figure 2.15 shows the evolution of the ionised gas density (similar to figure 2 in Arthur and Hoare, 2006), which behaves as expected. The cooling instability discussed in section 2.3.2 occurs and produces a variation in the optical depth, leading to the tell-tale spokes of the shadowing instability.

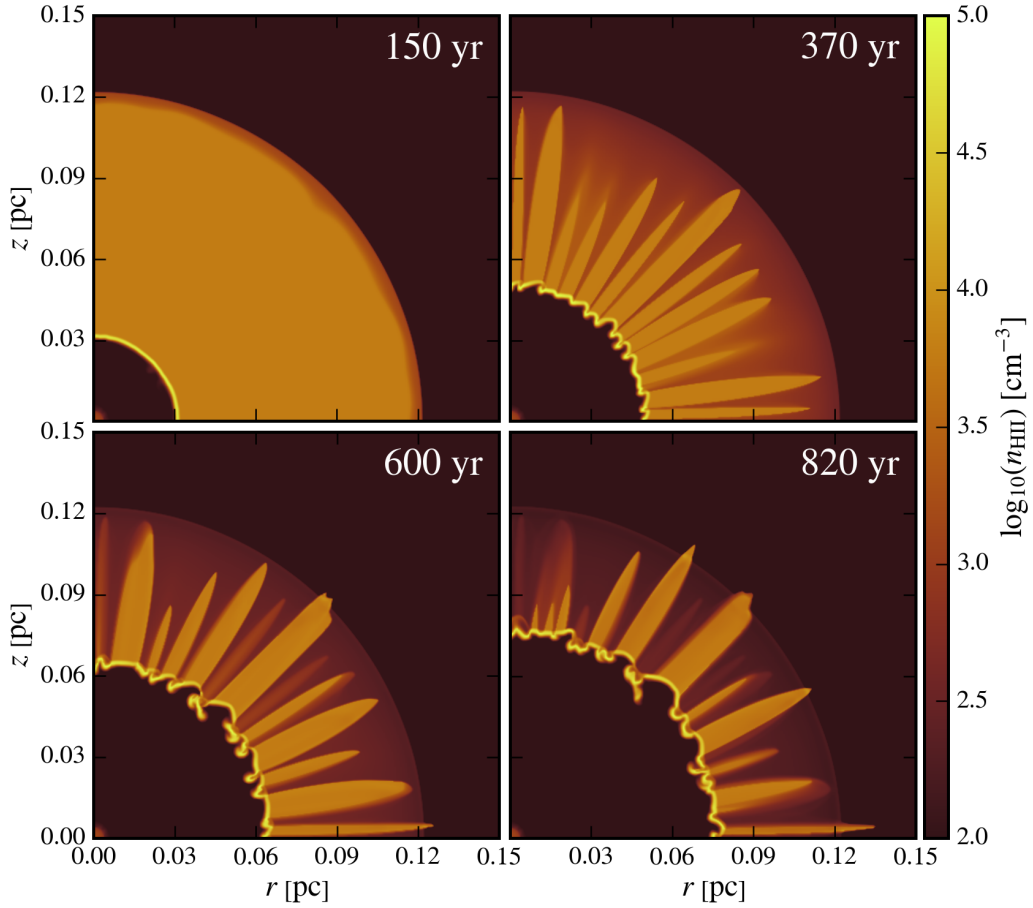

Fig. 2.15 Snapshots of $\log_{10}$ of the ionised hydrogen number density n_H taken during a simulation of a photo-ionised wind-blown bubble.

2.4 Simulated Observations

To produce synthetic radio continuum observations the scheme presented in the appendix of Dougherty et al. (2003) is used, which traces rays through the grid data TORCH outputs. Emission and absorption coefficients are calculated to accumulate intensity along a ray that passes through the numerical grid and ends up on an image plane.

Defining the source function

$$S_\nu \equiv \frac{j_\nu}{\alpha_\nu}, \tag{2.113}$$

where j_ν and α_ν are the emission and absorption coefficients, and using the fact that the optical depth is

$$\tau_\nu = \int \alpha_\nu ds\,, \tag{2.114}$$

we have the formal radiative transfer equation:

$$\frac{dI_\nu}{d\tau_\nu} = S_\nu - I_\nu\,. \tag{2.115}$$

We then multiply equation 2.115 by an integrating factor of e^{τ_ν} to give us

$$e^{\tau_\nu}\frac{dI_\nu}{d\tau_\nu} + e^{\tau_\nu} I_\nu = \frac{d(e^{\tau_\nu} I_\nu)}{d\tau_\nu} = e^{\tau_\nu} S_\nu\,, \tag{2.116}$$

which we then integrate over a path segment

$$I_\nu = e^{-\Delta\tau_\nu} I_0 + e^{-\Delta\tau_\nu}\int_0^{\Delta\tau_\nu} e^{\tau} S_\nu d\tau\,, \tag{2.117}$$

where I_0 is the intensity at the start of the path segment and $\Delta\tau_\nu$ is the optical depth across the segment. This integral is simpler for rays that pass through a numerical grid cell because the source function will be constant over the path. In this case the change in intensity across a ray segment in a grid cell is

$$I_\nu - I_0 = \left(1 - e^{-\Delta\tau_\nu}\right)\left(S_\nu - I_0\right)\,. \tag{2.118}$$

2.4.1 Radio Continuum

The electric field of a system of many charges moving non-relativistically is given (ignoring the velocity field contribution and retardation effects) by

$$\vec{E}_{\rm rad}(\vec{r},t) = \sum_i \frac{q_i}{4\pi\varepsilon_0}\frac{1}{|\vec{R}_i|c^2}\hat{R}_i \times \left(\hat{R}_i \times \ddot{\vec{r}}_i\right)\,, \tag{2.119}$$

where q_i are the particle charges, $\vec{R}_i$ are the distances between the particle positions $\vec{r}_i$ and the field position $\vec{r}$. As the field-point distance is a lot higher than the $\vec{r}_i$, the $\vec{R}_i$ are all approximately equal. Hence, using the definition of the dipole moment

$$\vec{d} = \sum_i q_i \vec{r}_i \,, \tag{2.120}$$

the electric and magnetic fields are

$$\vec{E}_{\rm rad}(\vec{r},t) = \frac{1}{4\pi\varepsilon_0}\frac{1}{|\vec{R}|c^2}\hat{R}\times\left(\hat{R}\times\ddot{\vec{d}}_i\right) \tag{2.121}$$

and

$$\vec{B}_{\rm rad}(\vec{r},t) = \frac{1}{c}\hat{R}\times\vec{E}_{\rm rad}(\vec{r},t)\,. \tag{2.122}$$

The aim is to get the free-free volume emissivity $j_\nu^{\rm ff} = dW/dVdtd\nu$ so we start with the magnitude of the Poynting vector, which is the rate of electromagnetic energy transfer dW/dt per unit area dA:

$$\frac{dW}{dtdA} = \frac{1}{\mu_0 c}|\vec{E}_{\rm rad}|^2 = \frac{\mu_0}{16\pi^2 c}\frac{|\ddot{\vec{d}}|^2}{|\vec{R}|^2}\sin^2\theta\,, \tag{2.123}$$

where θ is the angle between $\hat{R}$ and $\dot{\vec{v}}$. We arrive at the Larmor formula after integrating equation 2.123 over the surface of a sphere:

$$\frac{dW}{dt} = \frac{\mu_0|\ddot{\vec{d}}(t)|^2}{6\pi c}\,. \tag{2.124}$$

Using Parseval's theorem,

$$\int_{-\infty}^{+\infty}|\ddot{\vec{d}}(t)|^2dt = \int_{-\infty}^{+\infty}|\ddot{\vec{d}}(\omega)|^2d\omega = 2\int_0^{+\infty}|\ddot{\vec{d}}(\omega)|^2d\omega\,, \tag{2.125}$$

and differentiating the Fourier transform twice with respect to time, i.e. $\ddot{\vec{d}}(\omega) = -\omega^2 \vec{d}(\omega)$, we get

$$\frac{dW}{d\omega} = \frac{\mu_0}{3\pi c}|\ddot{\vec{d}}(\omega)|^2 = \frac{\mu_0}{3\pi c}\omega^4 |\vec{d}(\omega)|^2 \,. \tag{2.126}$$

For Bremsstrahlung, consider an electron moving past an ion with an impact parameter of b in the small-angle scattering regime. We have

$$\vec{d}(\omega) = \frac{e}{2\pi\omega^2}\int_{-\infty}^{\infty} \dot{\vec{v}} e^{i\omega t} dt \,. \tag{2.127}$$

The electron interacts with the ion over a brief collision time,

$$\tau = \frac{b}{v}, \tag{2.128}$$

during which either the exponential in equation 2.127 oscillates rapidly ($\omega t \gg 1$) and therefore contributes little to the integral or is of order unity ($\omega t \ll 1$) so that the integral becomes

$$\vec{d}(\omega) = \begin{cases} \frac{e}{(2\pi)^{1/2}\omega^2}\Delta\vec{v}, & \text{if } \omega t \ll 1 \,, \\ 0, & \text{if } \omega t \gg 1 \,. \end{cases} \tag{2.129}$$

The radiation spectrum is therefore

$$\frac{dW}{d\omega} = \begin{cases} \frac{\mu_0 e^2}{6\pi^2 c\omega^2}|\Delta\vec{v}|^2, & \text{if } \omega t \ll 1 \,, \\ 0, & \text{if } \omega t \gg 1 \,. \end{cases} \tag{2.130}$$

The strongest component of acceleration is perpendicular to the path of the electron so the change in velocity is approximately, in the small-angle scattering regime,

$$\Delta v \approx \frac{1}{4\pi\varepsilon_0}\frac{Ze^2}{m_e}\int_{-\infty}^{+\infty}\frac{b}{(b^2+v^2t^2)^{3/2}}dt = \frac{1}{4\pi\varepsilon_0}\frac{Ze^2}{m_e}\frac{2}{bv}, \tag{2.131}$$

so that

$$\frac{dW}{d\omega} \approx \begin{cases} \frac{1}{(4\pi\varepsilon_0)^3}\frac{8Z^2e^6}{3\pi c^3 m_e^2 b^2 v^2}, & \text{if } \omega t \ll 1, \\ 0, & \text{if } \omega t \gg 1. \end{cases} \tag{2.132}$$

To get the total spectrum for a gas with ion density n_i, electron density n_e and a fixed electron speed v we multiply equation 2.132 by the flux of electrons $n_e v$ and integrate over the area around n_i ions (with element $2\pi b db$):

$$\frac{dW}{d\omega dV dt} \approx \frac{1}{(4\pi\varepsilon_0)^3}\frac{16 n_e n_i Z^2 e^6}{3c^3 m_e^2 v}\ln\left(\frac{b_{\max}}{b_{\min}}\right), \tag{2.133}$$

where $b_{\min}$ is the minimum impact parameter for the small-angle scattering regime to hold and $b_{\max}$ is a value beyond which the approximation made at $\omega t \ll 1$ is no longer viable. Re-expressing this in terms of the Gaunt factor,

$$g_{\rm C}(v,\omega) = \frac{\sqrt{3}}{\pi}\ln\left(\frac{b_{\max}}{b_{\min}}\right), \tag{2.134}$$

gives us

$$\frac{dW}{d\omega dV dt} \approx \frac{1}{(4\pi\varepsilon_0)^3}\frac{16\pi n_e n_i Z^2 e^6}{3^{3/2}c^3 m_e^2 v} g_{\rm ff}(v,\omega). \tag{2.135}$$

A photon cannot be produced if $v < (2h\nu/m)^{1/2}$ and also $d\omega = 2\pi d\nu$ so the thermal Bremsstrahlung volume emissivity is equation 2.135 averaged over a thermal distribution of speeds to give

$$j_{\nu,{\rm C}} = \frac{dW}{dV dt d\nu} = \frac{1}{(4\pi\varepsilon_0)^3}\frac{32\pi e^6}{3m_e^{3/2}c^3}\sqrt{\frac{2\pi}{3k_{\rm B}T}} Z^2 n_e n_i \exp\left(\frac{-h\nu}{k_{\rm B}T}\right) g_{\rm ff}(v,\omega). \tag{2.136}$$

Finally the source function is the vacuum brightness of a black-body radiator,

$$S_{\nu,\mathrm{C}} = B_\nu(T) = \frac{2h\nu^3}{c^2}\frac{1}{e^{\frac{h\nu}{k_\mathrm{B}T}}-1}\,, \tag{2.137}$$

therefore the thermal free-free volume absorption coefficient is

$$\alpha_{\nu,\mathrm{C}} = \frac{1}{(4\pi\varepsilon_0)^3}\frac{16\pi e^6}{3m_e^{3/2}ch\nu^3}\sqrt{\frac{2\pi}{3k_\mathrm{B}T}}Z^2 n_e n_i \left(1-\exp\left(-\frac{h\nu}{k_\mathrm{B}T}\right)\right) g_{\mathrm{ff}}(\nu,\omega)\,. \tag{2.138}$$

2.4.2 Radio Recombination Lines

For absorptions causing a transition from state n to m the absorptivity (corrected for stimulated emission) is

$$\alpha_{\nu,\mathrm{L}} = \frac{h\nu}{4\pi}\left(N_n B_{nm} - N_m B_{mn}\right)\phi(\nu)\,, \tag{2.139}$$

where B_{nm} and B_{mn} are Einstein B-coefficients, N_n and N_m are number densities of atoms in level n and m respectively and $\phi(\nu)$ is a line profile function. Using the Einstein relations,

$$g_n B_{nm} = g_m B_{mn} \tag{2.140}$$

and

$$A_{mn} = \frac{2h\nu^3}{c^2}B_{mn}\,, \tag{2.141}$$

we can write equation 2.139 as

$$\alpha_{\nu,\mathrm{L}} = \frac{c^2 N_n g_m}{8\pi\nu^2 g_n n_\nu^2}A_{mn}\left(1-\frac{g_n N_m}{g_m N_n}\right)\phi_{mn}(\nu)\,, \tag{2.142}$$

where g_n are the statistical weights of energy level n, n_ν is the index of refraction of the gas (~ 1) and N_n is the population of electrons at level n which, under LTE

(local thermodynamic equilibrium) conditions, is

$$N_n^{\mathrm{LTE}} = \frac{N_e N_i h^3}{(2\pi m_e k_{\mathrm{B}} T_e)^{3/2}} \frac{g_n}{2} \exp\left(-\frac{\chi_n}{k_{\mathrm{B}} T_e}\right), \tag{2.143}$$

where χ_n is the energy of level n with sign convention $\chi_n < 0$. From equation 2.143 we get the useful relation:

$$\frac{g_n N_m^{\mathrm{LTE}}}{g_m N_n^{\mathrm{LTE}}} = \exp\left(-\frac{h\nu_0}{k_{\mathrm{B}} T}\right). \tag{2.144}$$

An Hα line that has final level number n will have $m = n+1$ therefore, using equations 2.142 and 2.144, the absorption coefficient can be written

$$\alpha_{\nu,\mathrm{L}}^{\mathrm{LTE}} = \frac{c^2 N_n^{\mathrm{LTE}}}{8\pi\nu^2} A_{n+1,n} \left(1 - \exp\left(-\frac{h\nu_0}{k_{\mathrm{B}} T}\right)\right) \phi(\nu), \tag{2.145}$$

with $g_n = 2n^2$ for Hydrogen atoms. To find the Einstein A-coefficient we use the correspondence principle: in the limit of large quantum numbers, a system reproduces classical physics. Radio photons are emitted by atomic transitions between high quantum numbers so, going ahead with this approximation, we can get the time-averaged power radiated from Larmor's equation,

$$\langle P \rangle = \frac{2e^2}{3c^3} (\omega^2 a_{n+1})^2 \langle \cos^2(\omega t) \rangle = \frac{16\pi^4 e^2 \nu^4 a_{n+1}^2}{3c^3}, \tag{2.146}$$

where a_{n+1} is the Bohr radius at level $n+1$ and the dipole moment has been taken as $e a_{n+1}$. For high quantum numbers $\Delta n \ll n$ the Rydberg formula is approximately

$$\nu = R_\infty c \left(\frac{1}{n^2} - \frac{1}{(n+1)^2}\right) \approx \frac{2R_\infty c}{n^3}. \tag{2.147}$$

Lastly, using

$$a_{n+1} \approx \frac{n^2 h^2}{4\pi^2 m_e e^2} \tag{2.148}$$

and

$$R_\infty = \frac{m_e e^4}{8\varepsilon_0^2 h^3 c}\,, \tag{2.149}$$

we have the Einstein A-coefficient:

$$A_{n+1,n} \approx \frac{64\pi^6 m_e e^{10}}{3(4\pi\varepsilon_0)^6 c^3 h^6 n^5}\,. \tag{2.150}$$

Line Profile

The full line profile can be represented as a convolution of the Doppler broadening profile, $\phi^{\mathrm{D}}(\nu)$, and the electron pressure profile, $\phi^{\mathrm{P}}(\nu)$ (Brocklehurst and Seaton, 1972). In LTE the atoms in the gas have a Maxwellian speed distribution and, along with the Doppler formula, the spectral line intensity profile due to Doppler broadening is given by

$$\phi^{\mathrm{D}}(\nu) = \frac{1}{\sqrt{2\pi\sigma^2}} \exp\left(\frac{(\nu-\nu_0)^2}{2\sigma^2}\right). \tag{2.151}$$

The variance includes thermal and microturbulent broadening:

$$\sigma^2 = \frac{1}{2}\left(\frac{\nu_0}{c}\right)^2 \left(\frac{2k_{\mathrm{B}}T}{m_p} + V_{\mathrm{turb}}^2\right), \tag{2.152}$$

where V_{turb} is the most probable turbulent velocity if the turbulent velocities are assumed to have a Maxwellian distribution (Lang, 1978, ch. 2.18).

The profile for electron pressure broadening is

$$\phi^{\mathrm{P}}(\nu) = \frac{\delta}{\pi}\frac{1}{(\nu-\nu_0)^2+\delta^2}\,, \tag{2.153}$$

where, using the results of Brocklehurst and Leeman (1971), δ may be approximated as

$$\delta = 4.7 \left(\frac{n}{100\,\mathrm{cm}^{-3}} \right)^{4.4} \left(\frac{T}{1.0 \times 10^4\,\mathrm{K}} \right)^{-0.1} \left(\frac{n_\mathrm{e}}{\mathrm{cm}^{-3}} \right) \quad \mathrm{Hz}\,. \tag{2.154}$$

Departure Coefficients

The line absorptivity and emissivities under the assumption of LTE are good approximations if the time to thermalise the gas is much shorter than than the recombination time, i.e. if $n \gg 1$ and the electron number densities are high (Gordon and Sorochenko, 2009).

Departure coefficients parameterise the departures from LTE and are defined as the ratio of the real population in level k to the population predicted under LTE conditions:

$$b_k \equiv \frac{N_k}{N_k^\mathrm{LTE}}\,. \tag{2.155}$$

These coefficients can be calculated using the code of (Gordon and Sorochenko, 2009).

The non-LTE absorptivity is then

$$\alpha_{\nu,\mathrm{L}} = \frac{b_n - b_{n+1} \exp\left(-\frac{h\nu_0}{k_\mathrm{B}T}\right)}{1 - \exp\left(-\frac{h\nu_0}{k_\mathrm{B}T}\right)} \alpha_{\nu,\mathrm{L}}^\mathrm{LTE}\,, \tag{2.156}$$

and, with $S_{\nu,\mathrm{L}} = B_\nu(T)$, the corresponding emissivity is

$$j_{\nu,\mathrm{L}} = b_{n+1} j_{\nu,\mathrm{L}}^\mathrm{LTE}\,. \tag{2.157}$$

Chapter 3

Hydrodynamical Models of Cometary HII Regions

3.1 Introduction

New Galactic plane surveys are revisiting the lifetime problem and providing large, well selected samples. The Galaxy-wide RMS survey found ~ 900 mid-IR bright compact HII regions (Lumsden et al., 2013). Mottram et al. (2011) used the results of this survey and determined the lifetime of the compact HII phase to be 300 kyr or ~ 3 % to 10 % of the source's main-sequence lifetime. Davies et al. (2011) simulated the RMS results using a particular Galactic gas distribution and different accretion models and compared with the luminosity distribution of the RMS survey. In this work each ionising star in the Galaxy was assumed to be producing HII regions in a uniform density medium and not blowing a stellar wind (i.e. simple Strömgren expansion).

The aim in this chapter is to produce a grid of more realistic UCHII regions to include in the galaxy model of Davies et al. (2011) by simulating cometary HII regions. I explore a parameter space spanning stellar mass, the density of the stellar environment and the age of the star and note the behaviour of some observables

across this space. In the next chapter I use this model grid to provide more realistic HII region sizes and fluxes in an improved galaxy model that is tested against the CORNISH survey. With such a large unbiased sample of UCHII regions (~ 240) it will be possible to test the models in the context of high-mass star formation on the Galactic scale.

In section 3.2 I introduce the numerical scheme and describe the models I simulated. The results of the simulations are presented in section 3.3 and I discuss the behaviour of the hot stellar wind region, the ionisation front, the emission measures and the spectral indices when stellar mass, age and cloud density are varied. The chapter is concluded in section 3.4 where I summarise my findings.

3.2 The Model

3.2.1 Numerical Scheme

The simulations of this chapter were produced using TORCH (see chapter 2) on a two-dimensional axisymmetric grid (Falle, 1991). In this code, three coupled physics problems (hydrodynamics, radiative transfer, and heating/cooling) are integrated separately and the result of each is combined to update the solution at each step using the Strang splitting scheme (Strang, 1968).

The governing hydrodynamic equations are: conservation of mass,

$$\frac{\partial \rho}{\partial t} + \nabla \cdot (\rho \vec{u}) = \dot{\rho}_{\rm w}(\vec{r}); \tag{3.1}$$

conservation of momentum,

$$\frac{\partial (\rho \vec{u})}{\partial t} + \nabla \cdot (\rho \vec{u} \otimes \vec{u}) + \nabla p = \vec{0}; \tag{3.2}$$

and conservation of energy,

$$\frac{\partial e}{\partial t} + \nabla \cdot (\vec{u}(e+p)) = H - C + \dot{e}_{\rm w}(\vec{r}) \,, \tag{3.3}$$

where ρ is the gas density, $\vec{u}$ is the fluid velocity, p is the thermal pressure, $e = \frac{1}{\gamma-1}p + \frac{1}{2}\rho u^2$ is the total energy density with $\gamma = \frac{5}{3}$, H and C are respectively the heating and cooling rates due to atomic/molecular transitions, $\dot{e}_{\rm w}(\vec{r})$ is the injection rate of stellar wind energy density and $\dot{\rho}_{\rm w}(\vec{r})$ is the injection rate of wind material density as a function of position.

We also have equations describing the advection of the hydrogen ionisation fraction,

$$\frac{\partial (f\rho)}{\partial t} + \nabla \cdot (f\rho\vec{u}) = \dot{\rho}_{\rm w}(\vec{r}) \,, \tag{3.4}$$

and the rate of hydrogen ionisations and recombinations,

$$\frac{{\rm d}f}{{\rm d}t} = (1-f)\,(\Gamma + n_{\rm e} C_{\rm H}) - f n_{\rm e} \alpha_{\rm H} \,, \tag{3.5}$$

where f is the fraction of hydrogen that is ionised, $n_{\rm e}$ is the electron number density, Γ is the photoionisation rate, $C_{\rm H}$ is the collisional ionisation coefficient and $\alpha_{\rm H}$ is the recombination coefficient of hydrogen.

Models were simulated on a numerical grid with square cells that have equal side lengths. The resolution of each grid is given in tables 3.2 and 3.3 along with the physical dimensions.

3.2.2 The Star's Environment

The model environment has the same density structure as in Model F in Arthur and Hoare (2006). Stars in these models are off-centre in a spherically symmetric density

distribution at a distance of 0.35 pc from the cloud centre. The density is given by

$$\rho = \rho_0 \left[1 + \left(\frac{r}{r_c} \right)^2 \right]^{\frac{-\alpha}{2}}, \tag{3.6}$$

where r is the distance from the cloud centre, $r_c = 0.01$ pc is the cloud core radius, ρ_0 is the density at the cloud centre and the power law index α parameterises the dependence on r when $r \gg r_c$. The density at the star's position is then given by

$$\rho_\star = \rho_0 \left[1 + \left(\frac{r_{sc}}{r_c} \right)^2 \right]^{\frac{-\alpha}{2}}, \tag{3.7}$$

where $r_{sc} = 0.35$ pc is the distance of the star from the cloud centre, so that $\rho_\star = \frac{1}{1226}\rho_0$ (assuming $\alpha = 2$).

The power law index, α, has been inferred using a number of different techniques leading to a wide range of values in the literature. Hatchell and Van der Tak (2003) found indices between 1.25 and 2.25. Five of the seven dark cloud envelopes that were investigated by Arquilla and Goldsmith (1985) were best characterized by an index of $\alpha \simeq 2$. A range of 1.0 to 1.5 was found by Van der Tak et al. (2000). Pirogov (2009) found an index of $\alpha = 1.6 \pm 0.3$, which falls more steeply in the outer layers of the dense core. For the current work a value of $\alpha = 2$ was adopted.

The initial pressure in a cloud of constant temperature will have the same structure as the density field. Without gravity, gas will move down the pressure gradient leading to bulk motion that can interfere with the dynamics of the star's stellar wind and ionisation field, especially over the period of 200 kyr each of the simulations here were run for. Instead the pressure of the environment was taken to be uniform such that lower temperatures occur towards the cloud core, and higher temperatures occur away from it (the temperature at the position of the star was 300 K).

3.2.3 Parameters

Using this model environment key parameters were explored, namely the cloud density at the position of the star and the mass of the ZAMS star. Values for these are given in tables 3.2 and 3.3. The stellar wind parameters, mass loss rate and terminal velocity, were calculated using the predictions of Vink et al. (2001). These depend on the metallicity (which was assumed to be solar) and also the effective temperature and luminosity of the star. I took values for these (for certain stellar masses) from Davies et al. (2011), which were calculated using the hydrostatic models of Meynet and Maeder (2000). For the same masses, Lyman continuum fluxes were also taken from Davies et al. (2011) who used calculations from Martins et al. (2005) and Lanz and Hubeny (2007). Effective temperature, luminosity and Lyman continuum flux depend only on stellar mass; hence, this is the only free parameter describing the star.

3.2.4 Stellar Winds

Vink et al. (2001) determined relations for mass-loss rates of O and B stars for a range of metallicities by using a Monte Carlo radiative transfer method (Vink et al., 1999, 2000) on model atmospheres produced by the Improved Sobolev Approximation code (De Koter et al., 1997, 1993). This method allowed them to find the radiative momentum transferred to the wind via photon absorptions and scatterings. Self-consistent solutions, i.e. models for which the radiative momentum was equal to the wind momentum of the model atmosphere, were then used to find mass-loss rates. Strictly speaking, the Vink et al. (2000) model is applicable in the range $15\,\mathrm{M}_{\odot} \leq M_{\star} \leq 120\,\mathrm{M}_{\odot}$; I am assuming the author's results can be extended to predict stellar wind parameters for the model stars with $M_{\star} < 15\,\mathrm{M}_{\odot}$.

Using the recipe in Vink et al. (2001) to find mass-loss rates we first find where the bi-stability jumps are in effective temperature. We then calculate the mass-loss and

Table 3.1 The stellar parameters used for the models. In order, the columns show: stellar mass, $M_\star$; effective temperature, $T_{\rm eff}$; stellar radius, $R_\star$; Luminosity, $L_\star$; Lyman continuum flux, $Q_{\rm Lyc}$; the mechanical luminosity of the wind, $\mathscr{L}$; mass loss rate, $\dot{M}$; the free-flowing wind speed, v_∞.

$M_\star$	$T_{\rm eff}$	$R_\star$	$\log_{10}(L_\star)$	$\log_{10}(Q_{\rm Lyc})$	$\mathscr{L}$	$\dot{M}$	v_∞
$[M_\odot]$	[K]	$[R_\odot]$	$[L_\odot]$	$[s^{-1}]$	$[erg\,s^{-1}]$	$[M_\odot\,yr^{-1}]$	$[km\,s^{-1}]$
6	19 000	3.0	3.01	43.33	5.38×10^{31}	1.33×10^{-10}	1.13×10^{3}
9	22 895	3.9	3.57	44.76	1.30×10^{32}	6.95×10^{-11}	2.43×10^{3}
12	26 743	4.5	3.96	46.02	1.72×10^{33}	8.03×10^{-10}	2.60×10^{3}
15	29 783	5.1	4.26	47.03	1.00×10^{34}	4.30×10^{-9}	2.71×10^{3}
20	33 824	6.0	4.61	48.00	6.67×10^{34}	2.57×10^{-8}	2.86×10^{3}
30	38 670	7.3	5.02	48.69	4.73×10^{35}	1.54×10^{-7}	3.11×10^{3}
40	42 610	8.7	5.34	49.09	1.86×10^{36}	5.74×10^{-7}	3.20×10^{3}
70	47 662	12.0	5.81	49.51	1.07×10^{37}	2.90×10^{-6}	3.41×10^{3}
120	50 853	17.1	6.23	49.81	4.13×10^{37}	1.11×10^{-5}	3.42×10^{3}

Table 3.2 The grid of parameters used for the models: stellar mass, $M_\star$; the number density, $n_\star$, of the cloud of hydrogen gas at the position of the star at the start of the simulation; the number of numerical grid cells along the radial axis, N_r; the number of numerical grid cells along the polar axis, N_z; and the physical extent of the numerical grid along the radial direction, L_r. The other columns are calculated values for each model including: the Strömgren radius to star-cloud distance ratio, $y_{\rm sc}$; the critical luminosity, $\mathscr{L}_{\rm crit}$; the wind start time, $t_{\rm start}$; and the cooling time in the injection region, $t_{\rm cool}$.

$M_\star$ [$M_\odot$]	$n_\star$ [cm^{-3}]	N_r	N_z	L_r [pc]	$y_{\rm sc}$	$R_{\rm inj}$ [pc]	$\mathscr{L}_{\rm crit}$ [erg s^{-1}]	$t_{\rm start}$ [kyr]	$t_{\rm cool}$ [kyr]
6	8.00×10^3	150	400	0.10	0.006	0.007	3.32×10^{38}	0.257	5.503×10^3
9	8.00×10^3	150	300	0.15	0.018	0.010	1.07×10^{39}	0.357	7.468×10^4
12	8.00×10^3	150	200	0.50	0.047	0.033	3.82×10^{39}	1.002	9.027×10^3
15	8.00×10^3	150	200	0.50	0.102	0.033	3.98×10^{39}	0.172	8.634×10^3
20	8.00×10^3	150	200	0.50	0.214	0.033	4.20×10^{39}	0.026	1.703×10^4
30	8.00×10^3	150	200	1.00	0.363	0.067	9.14×10^{39}	0.029	1.475×10^4
40	8.00×10^3	150	200	1.50	0.494	0.100	1.41×10^{40}	0.025	1.069×10^4
70	8.00×10^3	150	200	3.00	0.681	0.200	3.01×10^{40}	0.035	1.086×10^4
120	8.00×10^3	150	200	9.00	0.858	0.601	9.04×10^{40}	0.243	1.164×10^4
6	1.60×10^4	150	300	0.06	0.004	0.004	1.99×10^{38}	0.111	2.577×10^3
9	1.60×10^4	150	300	0.15	0.011	0.010	1.07×10^{39}	0.715	2.879×10^2
12	1.60×10^4	150	250	0.25	0.029	0.017	1.91×10^{39}	0.250	3.539×10^4
15	1.60×10^4	150	200	0.50	0.064	0.033	3.98×10^{39}	0.344	1.425×10^4
20	1.60×10^4	150	200	0.50	0.135	0.033	4.20×10^{39}	0.052	1.579×10^4
30	1.60×10^4	150	200	0.50	0.229	0.033	4.57×10^{39}	0.007	4.868×10^3
40	1.60×10^4	150	200	1.00	0.311	0.067	9.40×10^{39}	0.015	5.620×10^3
70	1.60×10^4	150	200	2.00	0.429	0.134	2.00×10^{40}	0.021	5.391×10^3
120	1.60×10^4	150	200	5.00	0.540	0.334	5.02×10^{40}	0.083	8.106×10^3

Table 3.3 Same as table 3.2 but for higher local number densities.

$M_\star$ [$M_\odot$]	$n_\star$ [cm^{-3}]	N_r	N_z	L_r [pc]	y_{sc}	R_{inj} [pc]	$\mathscr{L}_{crit}$ [erg s^{-1}]	t_{start} [kyr]	t_{cool} [kyr]
6	3.20×10^4	150	300	0.05	0.002	0.003	1.66×10^{38}	0.128	1.290×10^3
9	3.20×10^4	150	400	0.08	0.007	0.005	5.71×10^{38}	0.217	2.778×10^4
12	3.20×10^4	150	300	0.20	0.019	0.013	1.53×10^{39}	0.256	2.828×10^4
15	3.20×10^4	150	200	0.50	0.040	0.033	3.98×10^{39}	0.688	3.957×10^3
20	3.20×10^4	150	200	0.50	0.085	0.033	4.20×10^{39}	0.103	1.449×10^4
30	3.20×10^4	150	200	0.60	0.144	0.040	5.48×10^{39}	0.025	4.869×10^3
40	3.20×10^4	150	200	1.00	0.196	0.067	9.40×10^{39}	0.030	1.559×10^3
70	3.20×10^4	150	200	3.00	0.270	0.200	3.01×10^{40}	0.139	1.052×10^4
120	3.20×10^4	150	200	5.00	0.340	0.334	5.02×10^{40}	0.167	2.381×10^3
6	6.40×10^4	150	300	0.03	0.001	0.002	9.96×10^{37}	0.055	7.395×10^2
9	6.40×10^4	150	300	0.05	0.004	0.003	3.57×10^{38}	0.106	9.792×10^2
12	6.40×10^4	150	200	0.20	0.012	0.013	1.53×10^{39}	0.513	1.746×10^4
15	6.40×10^4	150	300	0.25	0.025	0.017	1.99×10^{39}	0.172	1.477×10^4
20	6.40×10^4	150	200	0.50	0.053	0.033	4.20×10^{39}	0.207	1.139×10^4
30	6.40×10^4	150	200	0.50	0.091	0.033	4.57×10^{39}	0.029	4.873×10^3
40	6.40×10^4	150	200	0.50	0.123	0.033	4.70×10^{39}	0.007	1.559×10^3
70	6.40×10^4	150	200	0.50	0.170	0.033	5.01×10^{39}	0.001	9.800×10^2
120	6.40×10^4	150	200	2.00	0.214	0.134	2.01×10^{40}	0.021	1.565×10^3
6	1.28×10^5	150	300	0.03	0.001	0.002	8.30×10^{37}	0.064	3.734×10^2
9	1.28×10^5	150	300	0.04	0.003	0.003	2.86×10^{38}	0.108	7.410×10^3
12	1.28×10^5	150	300	0.10	0.007	0.007	7.64×10^{38}	0.128	4.389×10^3
15	1.28×10^5	150	300	0.20	0.016	0.013	1.59×10^{39}	0.176	9.584×10^3
20	1.28×10^5	150	200	0.50	0.034	0.033	4.20×10^{39}	0.414	5.538×10^3
30	1.28×10^5	150	200	0.50	0.057	0.033	4.57×10^{39}	0.058	4.829×10^3
40	1.28×10^5	150	200	0.50	0.078	0.033	4.70×10^{39}	0.015	1.559×10^3
70	1.28×10^5	150	200	0.50	0.107	0.033	5.01×10^{39}	0.003	3.986×10^2
120	1.28×10^5	150	200	1.00	0.135	0.067	1.01×10^{40}	0.005	4.178×10^2

terminal velocities depending on what side of the jumps the effective temperature is. Bi-stability jumps are discontinuous changes in the mass-loss as a function of effective temperature attributed to changes in the ionisation balance of heavy elements. For the stars used in the simulated models only one jump occurs. At this jump Fe IV recombines to Fe III, an efficient line driver.

The location of the bi-stability jump depends on the characteristic wind density at 50 % of the terminal velocity of the wind,

$$\log_{10}\left(\frac{<\rho>}{\mathrm{g\,cm^{-3}}}\right) = -14.94 + 0.85\log_{10}\left(\frac{Z}{Z_\odot}\right) + 3.2\Gamma_e\,, \tag{3.8}$$

which itself depends on the metallicity, Z, and the ratio between the gravitational and radiative acceleration due to electron scattering,

$$\Gamma_e = 7.66\times10^{-5}\sigma_\mathrm{e}\left(\frac{L}{\mathrm{L_\odot}}\right)\left(\frac{M}{\mathrm{M_\odot}}\right)^{-1}\,, \tag{3.9}$$

with the electron scattering cross-section, σ_e, taken from Lamers and Leitherer (1993).

The temperature of the bi-stability jump is given by

$$\frac{T_\mathrm{eff}^\mathrm{jump1}}{\mathrm{K}} = 61200 + 2590\log_{10}\left(\frac{<\rho>}{\mathrm{g\,cm^{-3}}}\right)\,. \tag{3.10}$$

Mass-loss rates are then determined by which side of the bi-stability jump the star is on. On the cold side of the bi-stability jump:

$$\begin{aligned}\log_{10}\left(\frac{\dot{M}}{\mathrm{M}_\odot\,\mathrm{yr}^{-1}}\right) = &-6.688 - 1.339\log_{10}\left(\frac{M}{30\,\mathrm{M}_\odot}\right)\\ &- 1.601\log_{10}\left(\frac{v_\infty}{2v_{\mathrm{esc}}}\right)\\ &+ 2.210\log_{10}\left(\frac{L}{10^5\,\mathrm{L}_\odot}\right)\\ &+ 1.070\log_{10}\left(\frac{T_{\mathrm{eff}}}{2\times10^4\,\mathrm{K}}\right)\\ &+ 0.850\log_{10}\left(\frac{Z}{Z_\odot}\right),\end{aligned} \tag{3.11}$$

and on the hot side of the bi-stability jump:

$$\begin{aligned}\log_{10}\left(\frac{\dot{M}}{\mathrm{M}_\odot\,\mathrm{yr}^{-1}}\right) = &-6.697 - 1.313\log_{10}\left(\frac{M}{30\,\mathrm{M}_\odot}\right)\\ &- 1.226\log_{10}\left(\frac{v_\infty}{2v_{\mathrm{esc}}}\right)\\ &+ 2.194\log_{10}\left(\frac{L}{10^5\,\mathrm{L}_\odot}\right)\\ &+ 0.933\log_{10}\left(\frac{T_{\mathrm{eff}}}{2\times10^4\,\mathrm{K}}\right)\\ &+ 0.850\log_{10}\left(\frac{Z}{Z_\odot}\right).\end{aligned} \tag{3.12}$$

The ratios of the terminal flow velocity to the escape velocity were determined by Lamers et al. (1995) to be $\frac{v_\infty}{v_{\mathrm{esc}}} \simeq 1.3$ on the cold side of the jump and $\frac{v_\infty}{v_{\mathrm{esc}}} \simeq 2.6$ on the hot side. The escape velocity is given by

$$v_{\mathrm{esc}} = \sqrt{\frac{2GM_{\mathrm{eff}}}{R_\star}}, \tag{3.13}$$

where the effective mass (corrected for the electron scattering radiation pressure) is

$$M_{\mathrm{eff}} = (1-\Gamma_e)M_\star\,. \tag{3.14}$$

Mass-loss rates and terminal velocities were calculated for each of the model stars using the values in table 3.1 and are plotted in figures 3.1 and 3.2 respectively. As can be seen in the table the mass injection rate increases for higher-mass stars except between $6\,\mathrm{M}_\odot$ and $9\,\mathrm{M}_\odot$ where there is a decrease. This is due to the bi-stability jump; the star with $M_\star = 6\,\mathrm{M}_\odot$ is the only one that lies on the cold side of the bi-stability jump where Fe IV recombines to Fe III, an efficient line driver.

In order to simulate the effects of a stellar wind the thermal energy injection method developed by Chevalier and Clegg (1985) was used, which has also been used by Comeron (1997) and Arthur and Hoare (2006). Due to the resolution of the numerical grid used to simulate the models it was not possible to define a free flowing wind region around the star (as in Rozyczka, 1985) that is sufficiently resolved (low resolution regions seed instabilities that grow enough to render the simulation results unphysical). The stellar wind power is mostly converted to thermal energy at the reverse shock (Castor et al., 1975) so we do not need to reproduce the structure of the unshocked wind region. Instead we can inject the wind luminosity as a rate of mass, $\dot{M}$, and energy, $\frac{1}{2}\dot{M}v_\infty^2$, into the shocked wind region as it is this power that determines the evolution and structure of the bubble (Weaver et al., 1977).

Wind material density and energy density are added within the injection radius each time-step such that their integrated rates over the volume are $\dot{M}$ and $\frac{1}{2}\dot{M}v_\infty^2$ respectively. The rate of injected wind energy density is given by $\dot{e}_\mathrm{w} = \frac{1}{2}\dot{\rho}_\mathrm{w}v_\infty^2$, where $\dot{\rho}_\mathrm{w}$ is the rate of injected wind material density:

$$\dot{\rho}_\mathrm{w}(\vec{r}) = \begin{cases} \frac{\dot{M}}{\frac{4}{3}\pi R_\mathrm{inj}^3}\,, & \text{if } |\vec{r}| < R_\mathrm{inj}\,, \\ 0\,, & \text{otherwise}\,, \end{cases} \tag{3.15}$$

where R_inj is the injection radius, which is given in tables 3.2 and 3.3 for each model.

I tested and confirmed that the evolution of a spherically symmetric wind-blown bubble in a neutral medium with no radiative cooling is as predicted using this

method. The size of the injection region (~ 10 cells) in all the models was chosen to be large enough that the region is well resolved by the numerical grid and small enough that the injection region has little effect on the evolution of the bubble. The injection radius will act as a lower bound for the radius of the wind bubble; bubbles smaller than this will have the wrong size. Another undesirable effect is that the injection radius is the radius the wind bubble starts with so that the wind has had a head-start. It does, however, take time to inject enough pressure in the region to blow a wind. This is approximately the time it takes to add pressure into the injection region that is comparable to the ambient pressure i.e.

$$t_{\rm start} = \frac{p_{\rm a}}{\dot{p}} = \frac{n_{\rm a} k_{\rm B} T_{\rm a} (\gamma - 1)}{\dot{e}_{\rm w}} \,, \tag{3.16}$$

where $p_{\rm a}$, $n_{\rm a}$ and $T_{\rm a}$ are the pressure, hydrogen number density and temperature of the ambient gas, $k_{\rm B}$ is the Boltzmann constant and $\gamma = \frac{5}{3}$ is the ratio of heat capacities. The start times, $t_{\rm start}$, are given in tables 3.2 and 3.3 for all the models.

To confirm that the gas in the injection region of the models is adiabatic the maximum initial radius from which gas parcels can cool radiatively before exiting the injection region was calculated. The initial radius in units of the injection radius (Cantó et al., 2000):

$$r_{\rm i} = \exp\left(- \left[\frac{A v_\infty t_{\rm cool}}{R_{\rm inj}} \right] \right) , \tag{3.17}$$

where

$$A = \left(\frac{\gamma - 1}{\gamma + 1} \right)^{1/2} \left(\frac{\gamma + 1}{6\gamma + 2} \right)^{(3\gamma+1)/(5\gamma+1)} , \tag{3.18}$$

and the cooling time within the injection radius is

$$t_{\rm cool} \approx \frac{k_{\rm B} T_{\rm inj}}{n_{\rm inj} \Lambda_{\rm inj}} \,, \tag{3.19}$$

where $T_{\rm inj}$, $n_{\rm inj}$, and $\Lambda_{\rm inj}$ are the temperature, the hydrogen number density, and the cooling function values in the injection region. The cooling times, $t_{\rm cool}$, for the models were calculated at snapshots of $t = 50\,{\rm kyr}$ and are given in tables 3.2 and 3.3. I calculated the initial radii in equation 3.17 using these cooling times and found that they are all tiny fractions of the injection radius, hence the gas within the injection region is adiabatic for all of the models.

Radiative cooling may dominate the mechanical wind luminosity in the injection radius leading to the catastrophic cooling (or bi-modal) regime in which a stationary wind solution does not exist (Silich et al., 2003, 2004). In this regime the stagnation radius, where the gas velocity is zero, is not located at the centre of the injection region, but is instead located between the centre and the injection radius. Within the stagnation radius radiative cooling dominates and therefore mass will accumulate here. Between the stagnation radius and the injection radius the stationary wind solution still exists.

Tenorio-Tagle et al. (2007) found that a threshold luminosity, $\mathscr{L}_{\rm crit}$, exists above which the wind is in the bi-modal regime. The semi-analytical treatment by Wünsch et al. (2007) yielded the following formula for the threshold luminosity:

$$\mathscr{L}_{\rm crit} = \frac{6(\gamma-1)\pi\eta\alpha^2\mu_i^2 R_{\rm inj} v_\infty^4}{(\gamma+1)\Lambda_{\rm st}} \left(\frac{\eta v_\infty^2}{2} - \frac{c_{\rm st}^2}{\gamma-1} \right), \tag{3.20}$$

where η is the fraction of the injected wind power that is transferred to the shocked wind region, $\alpha = 0.28$ is a fiducial coefficient (with its best-fit value) and $c_{\rm st}$ and $\Lambda_{\rm st}$ are the sound speed and cooling function values at the stagnation radius respectively. Equation 3.20 can be reduced (Pittard 2016, in prep.) to

$$\mathscr{L}_{\rm crit} \approx 4.4 \times 10^{40} \left(\frac{R_{\rm inj}}{\rm pc} \right) \left(\frac{v_\infty}{1000\,{\rm km\,s^{-1}}} \right) \quad {\rm erg\,s^{-1}}. \tag{3.21}$$

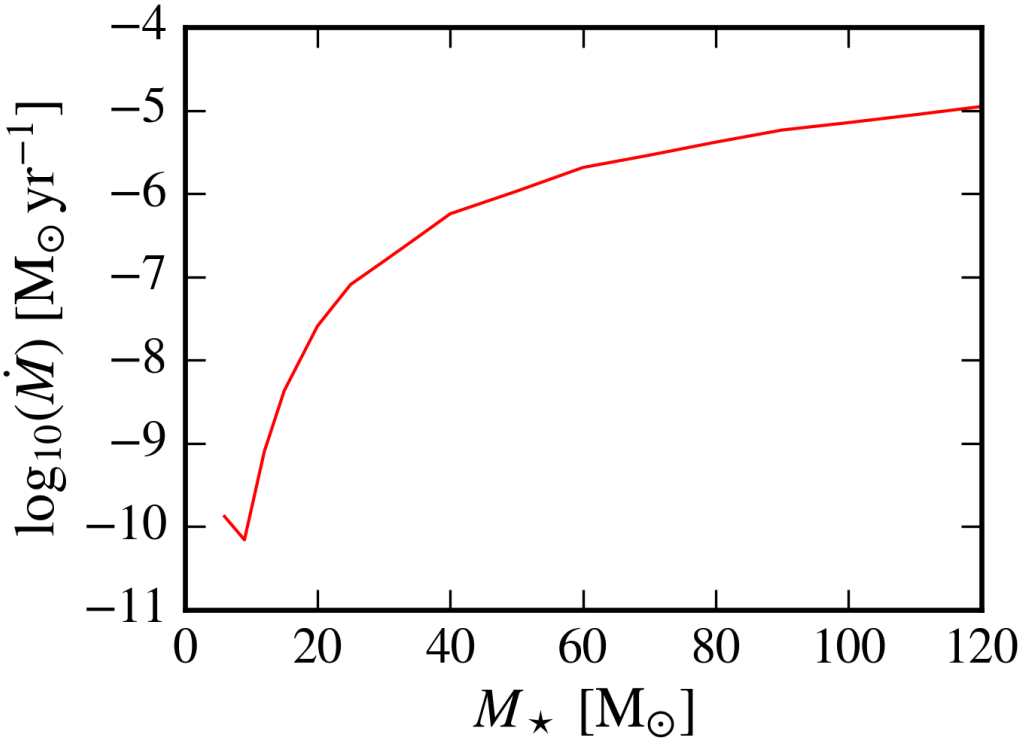

Fig. 3.1 The mass loss rate of stars plotted against stellar mass.

The threshold luminosity for all of the models, given in tables 3.2 and 3.3, is higher than the mechanical luminosity. The models are therefore in the stationary wind regime.

3.2.5 Radiation Field

Ionising radiation from each star was assumed to be monochromatic. Non-ionising FUV radiation was also included to heat the gas. It was assumed that recombinations to the ground state of hydrogen are locally reabsorbed i.e. the diffuse field was treated under the on-the-spot approximation. The recombination coefficient was therefore calculated using cubic spline interpolation of the case-B recombination coefficient data in Hummer (1994). Similarly, the collisional ionisation of neutral hydrogen was calculated by cubic spline interpolation of the data in Raga et al. (1997a). The

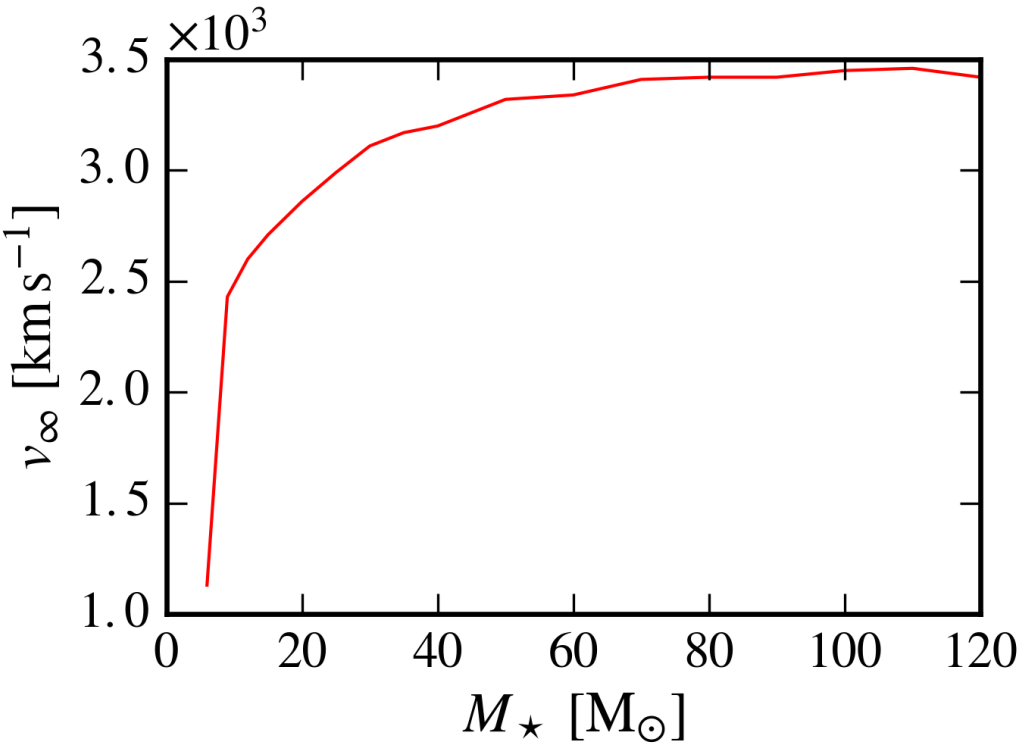

Fig. 3.2 The terminal velocity of stellar winds plotted against the driving star's mass.

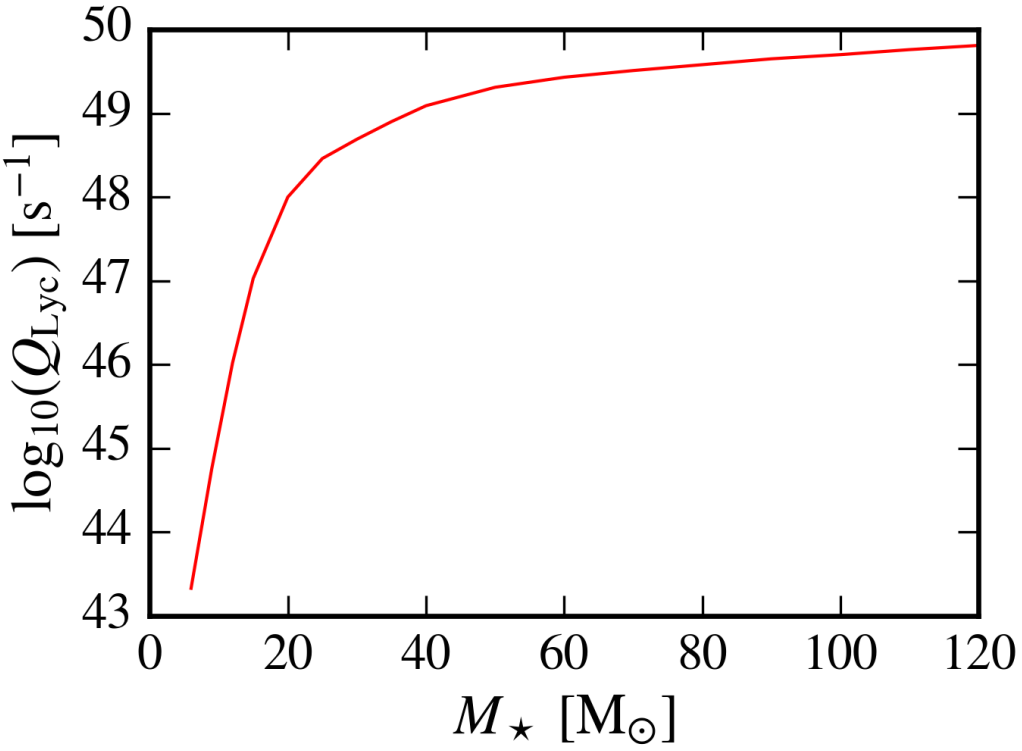

Fig. 3.3 The Lyman continuum photon rate of stars plotted against stellar mass.

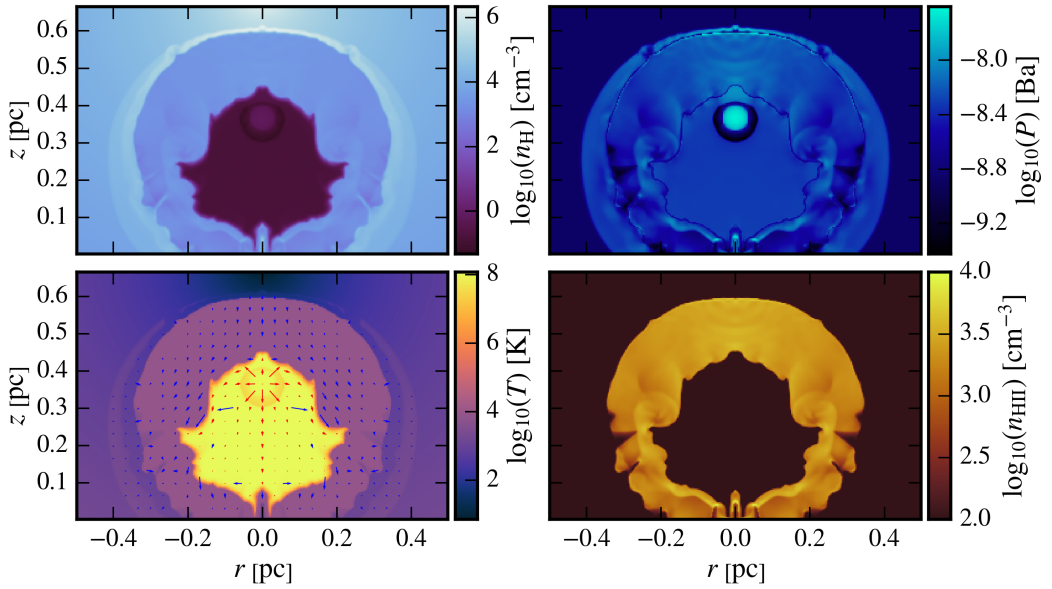

Fig. 3.4 Maps of hydrogen number density (top left), pressure (top right), temperature (bottom left) and ionised hydrogen number density (bottom right) of a model HII region around a star of mass $M_\star = 30\,\mathrm{M}_\odot$ with a local hydrogen number density of $n_\star = 3.2 \times 10^4\,\mathrm{cm}^{-3}$ at an age of $t = 50\,\mathrm{kyr}$. The star is located at $z = 0.37\,\mathrm{pc}$ and $r = 0\,\mathrm{pc}$, and the cloud centre is at the top of each frame. The black arrows on the bottom left plot represent velocities of $3\,\mathrm{km\,s}^{-1} < v \leq 30\,\mathrm{km\,s}^{-1}$ and the red arrows represent velocities of $30\,\mathrm{km\,s}^{-1} < v \leq 2700\,\mathrm{km\,s}^{-1}$.

cross-section for ionising photons was taken from Osterbrock (1989). Figure 3.3 shows the Lyman continuum flux plotted against stellar mass for the models.

3.3 Results and Discussion

Plots of hydrogen number density, pressure, temperature and ionised hydrogen number density are given in figure 3.4 for a typical cometary HII region. Nearest the star is the wind injection region of radius 0.04 pc from which a wind flows outwards becoming supersonic at its edge. The central temperature is $\sim 10^8$ K and decreases outside of the injection radius to the wind reverse shock. Gas outside the injection region is accelerated to supersonic speeds. I refer to the gas between the wind injection region and the reverse shock as the "unshocked stellar wind region". Downstream of the reverse shock is low density shocked stellar wind material, which

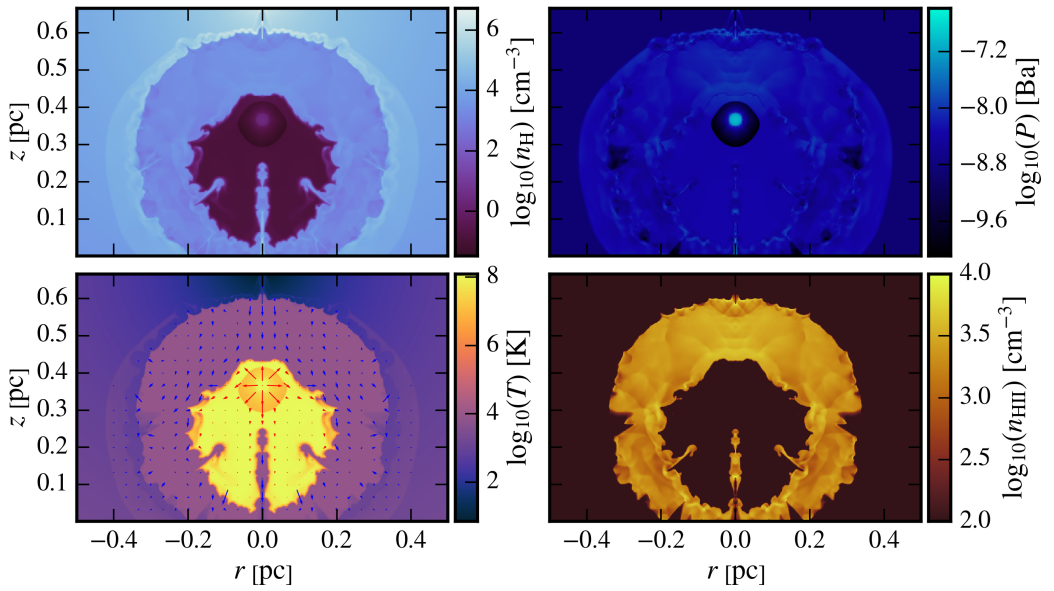

Fig. 3.5 Same as figure 3.4 but the simulation was run at twice the resolution in both dimensions.

is at a uniform temperature of $\sim 10^8$ K and subsonic. Further downstream lies the contact discontinuity separating the shocked stellar wind region and the cooler (~ 8000 K) ionised ambient gas. Earlier on in the evolution of this HII region I would expect to see a shock ahead of the contact discontinuity, but pressures either side of the shock have equilibrated so that the shock no longer exists. Finally, the ionised region is bounded by an ionisation front that separates ionised gas and the neutral gas shock. Photo-ionisation has heated the gas in the ionised region and therefore has created an overpressure with respect to the surrounding ambient gas, which explains the presence of the shock just outside of the ionisation front.

In figure 3.5 plots of the same HII region in figure 3.4 are shown but at double the resolution in both dimensions. We see that although there is more smaller-scale structure in these plots, the large-scale structure is unchanged.

Table 3.4 Measurements of $D_{\rm i}(\theta)$, which is the distance from the star to the edge of the ionised region along a direction with polar angle θ. The analytical Strömgren radius, $R_{\rm raga}$ (see equation 3.24) and the stagnation radius, $R_{\rm stag}$ (see equation 3.25) are also given by setting $n_{\rm H}$ equal to the local hydrogen number density, $n_\star$. These measurements were made for stars of age of 50 kyr.

$M_\star$	Dist.	$n_\star$ [10^4 cm^{-3}]				
[$M_\odot$]	[pc]	0.8	1.6	3.2	6.4	12.8
	$D_{\rm i}(0)$	0.034	0.019	0.010	0.0097	0.0056
	$D_{\rm i}(\frac{\pi}{2})$	0.037	0.023	0.014	0.010	0.0062
6	$D_{\rm i}(\pi)$	0.043	0.026	0.016	0.011	0.0076
	$R_{\rm raga}$	0.078	0.064	0.053	0.043	0.035
	$R_{\rm stag}$	0.036	0.022	0.014	0.0089	0.0056
	$D_{\rm i}(0)$	0.078	0.053	0.039	0.021	0.014
	$D_{\rm i}(\frac{\pi}{2})$	0.085	0.060	0.039	0.023	0.014
9	$D_{\rm i}(\pi)$	0.11	0.071	0.042	0.025	0.015
	$R_{\rm raga}$	0.13	0.10	0.084	0.069	0.057
	$R_{\rm stag}$	0.11	0.067	0.042	0.027	0.017
	$D_{\rm i}(0)$	0.15	0.095	0.077	0.062	0.035
	$D_{\rm i}(\frac{\pi}{2})$	0.17	0.12	0.088	0.062	0.040
12	$D_{\rm i}(\pi)$	0.19	0.15	0.11	0.071	0.045
	$R_{\rm raga}$	0.19	0.16	0.13	0.10	0.086
	$R_{\rm stag}$	0.28	0.18	0.11	0.070	0.044
	$D_{\rm i}(0)$	0.20	0.16	0.14	0.093	0.070
	$D_{\rm i}(\frac{\pi}{2})$	0.26	0.20	0.15	0.11	0.079
15	$D_{\rm i}(\pi)$	0.31	0.24	0.18	0.13	0.096
	$R_{\rm raga}$	0.27	0.22	0.18	0.15	0.12
	$R_{\rm stag}$	0.61	0.38	0.24	0.15	0.096
	$D_{\rm i}(0)$	0.26	0.24	0.19	0.17	0.13
	$D_{\rm i}(\frac{\pi}{2})$	0.40	0.32	0.24	0.19	0.15
20	$D_{\rm i}(\pi)$	0.48	0.38	0.30	0.22	0.17
	$R_{\rm raga}$	0.38	0.31	0.25	0.20	0.17
	$R_{\rm stag}$	1.3	0.81	0.51	0.32	0.20
	$D_{\rm i}(0)$	0.30	0.26	0.23	0.21	0.18
	$D_{\rm i}(\frac{\pi}{2})$	0.56	0.43	0.34	0.26	0.21
30	$D_{\rm i}(\pi)$	0.78	0.58	0.42	0.34	0.24
	$R_{\rm raga}$	0.48	0.39	0.31	0.26	0.21
	$R_{\rm stag}$	2.2	1.4	0.87	0.55	0.34

Table 3.5 Same as table 3.4 but for higher masses.

$M_\star$	Dist.	$n_\star$ [10^4 cm^{-3}]				
[$M_\odot$]	[pc]	0.8	1.6	3.2	6.4	12.8
	$D_i(0)$	0.31	0.30	0.26	0.24	0.20
	$D_i(\frac{\pi}{2})$	0.74	0.56	0.44	0.34	0.26
40	$D_i(\pi)$	1.1	0.75	0.56	0.47	0.33
	R_{raga}	0.56	0.45	0.36	0.29	0.24
	R_{stag}	3.0	1.9	1.2	0.74	0.47
	$D_i(0)$	0.33	0.32	0.33	0.26	0.24
	$D_i(\frac{\pi}{2})$	1.2	0.87	0.77	0.48	0.39
70	$D_i(\pi)$	1.4	1.0	0.88	0.60	0.47
	R_{raga}	0.66	0.52	0.42	0.34	0.28
	R_{stag}	4.1	2.6	1.6	1.0	0.64
	$D_i(0)$	1.3	0.39	0.39	0.32	0.28
	$D_i(\frac{\pi}{2})$	2.0	1.2	1.1	0.71	0.54
120	$D_i(\pi)$	2.4	1.6	1.3	0.88	0.75
	R_{raga}	0.75	0.59	0.47	0.38	0.31
	R_{stag}	5.2	3.2	2.0	1.3	0.81

3.3.1 Ionisation Fronts

The sizes of the ionisation fronts are shown in tables 3.4 to 3.7 along with analytical radii of ionised regions that would evolve around stars with the same stellar parameters but in a uniform density medium. Assuming balance between photo-ionisations and recombinations, for a star in a uniform medium with no stellar wind we have:

$$Q_{\rm Lyc} = \frac{4\pi}{3} n_{\rm i}^2(t)\,\alpha_{\rm B} R_{\rm IF}^3(t)\,, \tag{3.22}$$

where $n_{\rm i}$ is the hydrogen number density inside the ionised region, $\alpha_{\rm B}$ is the case-B recombination coefficient for hydrogen and $R_{\rm IF}^3(t)$ is the time-dependent radius of the ionised region. The Strömgren radius is the initial radius of the ionised region:

$$R_{\rm st} = \left(\frac{3Q_{\rm Lyc}}{4\pi n_{\rm H}^2 \alpha_{\rm B}}\right)^{1/3}, \tag{3.23}$$

Table 3.6 Measurements of $D_{\rm i}(\theta)$, which is the distance from the star to the edge of the ionised region along a direction with polar angle θ. The analytical Strömgren radius, $R_{\rm raga}$ (see equation 3.24) and the stagnation radius, $R_{\rm stag}$ (see equation 3.25) are also given by setting $n_{\rm H}$ equal to the local hydrogen number density, $n_\star$. These measurements were made for stars in a local number density of 3.2×10^4 cm^{-3}.

$M_\star$	Dist.	Age [kyr]				
[M$_\odot$]	[pc]	20	40	60	80	100
	$D_{\rm i}(0)$	0.015	0.012	0.012	0.016	0.014
	$D_{\rm i}(\frac{\pi}{2})$	0.016	0.014	0.015	0.016	0.016
6	$D_{\rm i}(\pi)$	0.019	0.015	0.019	0.019	0.018
	$R_{\rm raga}$	0.031	0.046	0.058	0.069	0.078
	$R_{\rm stag}$	0.014	0.014	0.014	0.014	0.014
	$D_{\rm i}(0)$	0.038	0.041	0.041	0.038	0.038
	$D_{\rm i}(\frac{\pi}{2})$	0.036	0.041	0.040	0.039	0.038
9	$D_{\rm i}(\pi)$	0.041	0.044	0.043	0.039	0.050
	$R_{\rm raga}$	0.050	0.074	0.094	0.11	0.13
	$R_{\rm stag}$	0.042	0.042	0.042	0.042	0.042
	$D_{\rm i}(0)$	0.059	0.078	0.085	0.092	0.096
	$D_{\rm i}(\frac{\pi}{2})$	0.069	0.087	0.097	0.10	0.11
12	$D_{\rm i}(\pi)$	0.079	0.11	0.12	0.12	0.13
	$R_{\rm raga}$	0.076	0.11	0.14	0.17	0.19
	$R_{\rm stag}$	0.11	0.11	0.11	0.11	0.11
	$D_{\rm i}(0)$	0.11	0.13	0.15	0.17	0.18
	$D_{\rm i}(\frac{\pi}{2})$	0.11	0.15	0.17	0.19	0.21
15	$D_{\rm i}(\pi)$	0.12	0.16	0.19	0.23	0.25
	$R_{\rm raga}$	0.11	0.16	0.20	0.23	0.27
	$R_{\rm stag}$	0.24	0.24	0.24	0.24	0.24
	$D_{\rm i}(0)$	0.13	0.18	0.21	0.24	0.26
	$D_{\rm i}(\frac{\pi}{2})$	0.15	0.22	0.26	0.30	0.33
20	$D_{\rm i}(\pi)$	0.17	0.24	0.31	0.35	0.40
	$R_{\rm raga}$	0.15	0.22	0.27	0.32	0.37
	$R_{\rm stag}$	0.51	0.51	0.51	0.51	0.51
	$D_{\rm i}(0)$	0.17	0.21	0.24	0.26	0.29
	$D_{\rm i}(\frac{\pi}{2})$	0.21	0.30	0.36	0.43	0.47
30	$D_{\rm i}(\pi)$	0.24	0.38	0.45	0.50	0.63
	$R_{\rm raga}$	0.19	0.28	0.35	0.41	0.46
	$R_{\rm stag}$	0.87	0.87	0.87	0.87	0.87

Table 3.7 Same as table 3.6 but for higher masses.

$M_\star$	Dist.	Age [kyr]				
[$M_\odot$]	[pc]	20	40	60	80	100
	$D_{\rm i}(0)$	0.19	0.24	0.26	0.29	0.31
	$D_{\rm i}(\frac{\pi}{2})$	0.26	0.24	0.47	0.54	0.61
40	$D_{\rm i}(\pi)$	0.31	0.47	0.59	0.73	0.82
	$R_{\rm raga}$	0.22	0.32	0.40	0.47	0.53
	$R_{\rm stag}$	1.2	1.2	1.2	1.2	1.2
	$D_{\rm i}(0)$	0.24	0.34	0.29	0.34	0.34
	$D_{\rm i}(\frac{\pi}{2})$	0.36	0.67	0.81	1.00	1.1
70	$D_{\rm i}(\pi)$	0.50	0.70	0.87	0.95	1.1
	$R_{\rm raga}$	0.26	0.37	0.46	0.54	0.61
	$R_{\rm stag}$	1.6	1.6	1.6	1.6	1.6
	$D_{\rm i}(0)$	0.32	0.40	0.44	0.42	0.48
	$D_{\rm i}(\frac{\pi}{2})$	0.70	0.96	1.1	1.3	1.5
120	$D_{\rm i}(\pi)$	0.81	1.3	1.3	1.5	1.6
	$R_{\rm raga}$	0.30	0.42	0.52	0.60	0.68
	$R_{\rm stag}$	2.0	2.0	2.0	2.0	2.0

where $n_{\rm H}$ is the initial hydrogen number density of the uniform medium. Ionisation heats the gas, which therefore sets up an overpressure; expansion thereafter is driven by this overpressure. The analytical radius of the ionised region (Raga et al., 2012) is given by:

$$R_{\rm raga} = R_{\rm st}\left(1+\frac{7}{4}\sqrt{\frac{4}{3}}\frac{t}{t_{\rm s}}\right)^{4/7}, \tag{3.24}$$

where $t_{\rm s} = R_{\rm st}/c_{\rm i}$ is the sound crossing time-scale and $c_{\rm i}$ is the sound speed of the ionised gas. The isothermal sound speed in the ionised ambient gas was assumed to be $c_{\rm i} = \sqrt{\frac{RT}{\mu_{\rm H}}}$, where the ionised gas temperature is $T \simeq 8000\,{\rm K}$, the average molar mass of ionised hydrogen is $\mu_H = 0.5\,{\rm g\,mol^{-1}}$ and R is the gas constant, giving a sound speed of $c_{\rm a} = 11.5\,{\rm km\,s^{-1}}$.

In tables 3.4 and 3.5 the measured ionisation regions show a decrease in size for higher local densities as expected. The sizes also increase for higher masses due to higher Lyman continuum photon fluxes. Equation 3.24 is only a good approximation

at early times i.e. when the radius is much smaller than the stagnation radius,

$$R_{\rm stag} = \left(\frac{4}{3}\right)^{2/3} \left(\frac{c_{\rm i}}{c_{\rm a}}\right)^{4/3} R_{\rm st}\,, \tag{3.25}$$

where $c_{\rm a}$ is the isothermal sound speed of the neutral ambient gas that, assuming the temperature of this gas is $T \simeq 300\,{\rm K}$, has the value $c_{\rm a} \simeq 1.58\,{\rm km\,s^{-1}}$. In the models we therefore have $R_{\rm stag} \simeq 17.2 R_{\rm st}$. We can see that for smaller Strömgren radii the stagnation time occurs earlier. Tables 3.6 and 3.7 show a stagnating ionisation front, which occurs at earlier ages for smaller-mass stars.

The lower the ratio of the analytical radius (equation 3.24) of the ionised region to stagnation radius (equation 3.25) the better the analytical radius is at approximating the measured radius. The analytical radius will over-estimate the measured radius for ratios that are closer to or larger than one. This effect is seen in tables 3.4 to 3.7. Higher-mass stars have larger Strömgren radii so their stagnation times occur later and therefore the analytical to measured radius ratio will be lower for these stars compared to lower-mass stars in the same density field and at the same age. At high enough stellar masses, $M_\star \geq 20\,{\rm M}_\odot$, the analytical radius under-estimates the ionisation front distance and is worse the higher the mass is. This is due to a number of factors. Higher-mass stars have more energetic winds and therefore larger regions of hot stellar wind; recombination rates are lower in these higher temperature regions meaning ionisation balances will occur at further distances from the star. The wind injection region is initially fully ionised so the ionisation front has had a head-start. For these stars the ionisation front (in the "radial" direction) has travelled far enough that it starts to travel down the density gradient rather than along a density contour.

Most of the simulations did not show the unbounded ionisation front expansion predicted by Franco et al. (1990) for $\alpha > 3/2$. Only for stars with masses $M_\star \geq 40\,{\rm M}_\odot$ and local densities $n_\star \leq 1.6 \times 10^4\,{\rm cm^{-3}}$ did the ionisation front break free of the cloud and almost always in finger-like structures (a.k.a. the shadowing instability,

see Williams, 1999). In all other models the regions are bounded approximately by a sphere, which is consistent with the three-dimensional simulations of off-centre UCHII regions by Mac Low et al. (2007). The regions are at a roughly constant density throughout the simulation and grow to a maximum radius that coincides with when the pressures either side of the ionisation front have equalised.

These results very closely match those in Arthur (2007), in which the condition necessary for HII regions in power-law density environments to remain bounded during their initial formation stage was given by:

$$\frac{1}{3}y_{\rm sc}^3 < \frac{2}{(2\alpha-1)(2\alpha-2)(2\alpha-3)}, \tag{3.26}$$

where $y_{\rm sc} = R_{\rm st}/r_{\rm sc}$ i.e. the ratio of the Strömgren radius for a star in a uniform medium to the distance between the star and the cloud centre. Values of this ratio for each set of model parameters were calculated and are given in tables 3.2 and 3.3 by setting $n_{\rm H}$ in equation 3.23 equal to the local hydrogen number density, $n_\star$. The power-law density environments have $\alpha = 2$, so equation 3.26 reduces to $y_{\rm sc} < 1$, which is true for all of the models. Arthur (2007) also found that in $\alpha = 2$ power-law environments, if $y_{\rm sc} \lesssim 0.02$ then pressure balance can halt the breakout of the HII region during the expansion stage. As previously mentioned the pressures do equalise before the HII regions can become unbounded for most models. However, this is also seen for models with $y_{\rm sc} > 0.02$.

3.3.2 Wind Forward Shock

Tables 3.8 to 3.11 list the sizes of the shocked stellar wind regions as a function of density and time respectively. In tables 3.10 and 3.11 the sizes of the shocked stellar wind regions show a plateau at early times for low-mass stars. The plateau occurs at later times for higher-mass stars. This suggests that the bubbles are becoming pressure confined (plots of the pressure confirm this).

Table 3.8 Measurements of $D_s(\theta)$, which is the distance from the star to the edge of the shocked stellar wind region along a direction with polar angle θ. The analytical radius for a radiative bubble at the pressure confinement time, R_P (see equation 3.28 and equation 3.29), is also given. These measurements were made for stars of age 50 kyr.

$M_\star$	Dist.	$n_\star$ [10^4 cm^{-3}]				
[$M_\odot$]	[pc]	0.8	1.6	3.2	6.4	12.8
6	$D_s(0)$	0.018	0.0097	0.0059	0.0062	0.0035
	$D_s(\frac{\pi}{2})$	0.024	0.017	0.0088	0.0073	0.0043
	$D_s(\pi)$	0.032	0.018	0.012	0.0093	0.0062
	R_P	0.0071	0.0050	0.0033	0.0027	0.0019
9	$D_s(0)$	0.016	0.024	0.0097	0.0035	0.0029
	$D_s(\frac{\pi}{2})$	0.015	0.018	0.017	0.0062	0.0037
	$D_s(\pi)$	0.085	0.018	0.023	0.014	0.0066
	R_P	0.0062	0.0047	0.0034	0.0023	0.0016
12	$D_s(0)$	0.041	0.011	0.022	0.021	0.012
	$D_s(\frac{\pi}{2})$	0.037	0.022	0.025	0.022	0.018
	$D_s(\pi)$	0.14	0.11	0.063	0.038	0.021
	R_P	0.018	0.014	0.011	0.0083	0.0060
15	$D_s(0)$	0.031	0.044	0.040	0.026	0.022
	$D_s(\frac{\pi}{2})$	0.051	0.044	0.040	0.031	0.020
	$D_s(\pi)$	0.22	0.16	0.12	0.082	0.066
	R_P	0.032	0.027	0.021	0.017	0.013
20	$D_s(0)$	0.040	0.047	0.057	0.065	0.043
	$D_s(\frac{\pi}{2})$	0.079	0.074	0.062	0.057	0.050
	$D_s(\pi)$	0.34	0.26	0.19	0.14	0.11
	R_P	0.063	0.054	0.044	0.036	0.030
30	$D_s(0)$	0.074	0.079	0.079	0.071	0.071
	$D_s(\frac{\pi}{2})$	0.15	0.14	0.13	0.13	0.14
	$D_s(\pi)$	0.65	0.38	0.36	0.25	0.17
	R_P	0.14	0.12	0.098	0.080	0.067

Table 3.9 Same as table 3.8 but for higher masses.

$M_\star$	Dist.	$n_\star$ [10^4 cm^{-3}]				
[$M_\odot$]	[pc]	0.8	1.6	3.2	6.4	12.8
40	$D_s(0)$	0.13	0.11	0.15	0.12	0.094
	$D_s(\frac{\pi}{2})$	0.28	0.24	0.18	0.27	0.18
	$D_s(\pi)$	0.94	0.62	0.44	0.40	0.29
	R_P	0.27	0.22	0.18	0.15	0.12
70	$D_s(0)$	0.22	0.21	0.22	0.18	0.18
	$D_s(\frac{\pi}{2})$	1.1	0.79	0.63	0.43	0.37
	$D_s(\pi)$	1.1	0.91	0.77	0.56	0.47
	R_P	0.70	0.55	0.51	0.35	0.30
120	$D_s(0)$	1.2	0.34	0.31	0.25	0.22
	$D_s(\frac{\pi}{2})$	1.9	1.2	1.1	0.63	0.49
	$D_s(\pi)$	2.2	1.5	1.3	0.81	0.71
	R_P	1.7	1.2	1.1	0.79	0.64

I use the results of an analysis of stellar wind evolution by Koo and McKee (1992) to see if this behaviour is physical. The terminal wind velocity in all of the models is lower than the critical wind velocity defined in Koo and McKee (1992, see their equation 2.5), indicating that the wind-bubbles are radiative. In this regime the cooling time of the shocked wind is shorter than the time it takes to accumulate a significant mass of gas ahead of the shock. I found that the radii of the shocked stellar wind regions are consistent with pressure-confined fully radiative bubbles.

Numerical diffusion can cause extra cooling, i.e. the cooling length might not be sufficiently resolved and therefore intermediate temperatures are found in a higher volume of the gas. Kelvin-Helmholtz instabilities can also enhance cooling by increasing the surface area of the contact discontinuity. Increasing the resolution of the numerical grid increases the growth of these instabilities to further enhance cooling. Resolution tests were carried out that confirm that the cooling across the contact discontinuity was not enhanced significantly by numerical effects.

Table 3.10 Measurements of $D_s(\theta)$, i.e. the distance from the star to the edge of the shocked stellar wind region along a direction with polar angle θ. The analytical radius for a radiative bubble at the pressure confinement time, R_P (see equation 3.28 and equation 3.29), is also given. These measurements were made for stars in a local number density of 3.2×10^4 cm^{-3}.

$M_\star$	Dist.	Age [kyr]				
[$M_\odot$]	[pc]	20	40	60	80	100
6	$D_s(0)$	0.0088	0.0062	0.0059	0.0094	0.0094
	$D_s(\frac{\pi}{2})$	0.011	0.010	0.010	0.011	0.011
	$D_s(\pi)$	0.013	0.0098	0.013	0.012	0.013
	R_P	0.0038	0.0035	0.0036	0.0039	0.0038
9	$D_s(0)$	0.0088	0.011	0.015	0.011	0.018
	$D_s(\frac{\pi}{2})$	0.010	0.0086	0.012	0.0082	0.0088
	$D_s(\pi)$	0.022	0.026	0.022	0.0071	0.0059
	R_P	0.0032	0.0036	0.0035	0.0034	0.0034
12	$D_s(0)$	0.018	0.013	0.028	0.022	0.044
	$D_s(\frac{\pi}{2})$	0.016	0.018	0.021	0.028	0.028
	$D_s(\pi)$	0.050	0.078	0.053	0.081	0.066
	R_P	0.0090	0.011	0.012	0.012	0.012
15	$D_s(0)$	0.041	0.038	0.035	0.042	0.048
	$D_s(\frac{\pi}{2})$	0.033	0.038	0.041	0.039	0.044
	$D_s(\pi)$	0.049	0.099	0.14	0.18	0.19
	R_P	0.017	0.021	0.023	0.025	0.027
20	$D_s(0)$	0.035	0.059	0.057	0.044	0.047
	$D_s(\frac{\pi}{2})$	0.041	0.059	0.081	0.065	0.059
	$D_s(\pi)$	0.11	0.18	0.23	0.28	0.33
	R_P	0.031	0.041	0.046	0.052	0.055
30	$D_s(0)$	0.092	0.071	0.079	0.088	0.074
	$D_s(\frac{\pi}{2})$	0.088	0.10	0.12	0.12	0.12
	$D_s(\pi)$	0.18	0.33	0.37	0.41	0.51
	R_P	0.067	0.088	0.10	0.11	0.12

Table 3.11 Same as table 3.10 but for higher masses.

$M_\star$	Dist.	Age [kyr]				
[$M_\odot$]	[pc]	20	40	60	80	100
40	$D_s(0)$	0.12	0.15	0.15	0.11	0.14
	$D_s(\frac{\pi}{2})$	0.21	0.18	0.21	0.21	0.26
	$D_s(\pi)$	0.28	0.41	0.41	0.65	0.73
	R_P	0.12	0.12	0.19	0.21	0.23
70	$D_s(0)$	0.18	0.22	0.19	0.20	0.23
	$D_s(\frac{\pi}{2})$	0.32	0.56	0.70	0.64	0.71
	$D_s(\pi)$	0.47	0.70	0.81	0.88	1.1
	R_P	0.29	0.46	0.53	0.61	0.68
120	$D_s(0)$	0.32	0.29	0.26	0.33	0.37
	$D_s(\frac{\pi}{2})$	0.36	0.90	1.1	1.2	1.4
	$D_s(\pi)$	0.58	1.1	1.3	1.4	1.6
	R_P	0.77	0.98	1.1	1.2	1.3

Figure 3.6 shows a plot of the injected energy and total energy within the shocked stellar wind region over time for one of the model stars. The total energy is a few orders of magnitude lower than the total injected energy indicating that most of the energy is radiated away. We can also see a plateau in the total energy i.e. eventually energy is lost at the same rate that it is injected, which implies that the wind bubbles are radiative.

The time it takes for a radiative bubble to transition to the pressure confined stage is approximately

$$t_P = \left(\frac{3\mathscr{L}}{16\pi\rho_i c_i^4 v_\infty} \right)^{1/2}, \tag{3.27}$$

where $\mathscr{L} = \frac{1}{2}\dot{M}v_\infty^2$ is the mechanical wind luminosity, ρ_a is the ambient density and c_i is the isothermal sound speed in the ambient medium. The ambient density, ρ_i, was determined for each snapshot as the density upstream of the shock in the ionised ambient region in the radial direction. Using equation 3.22 we can get an

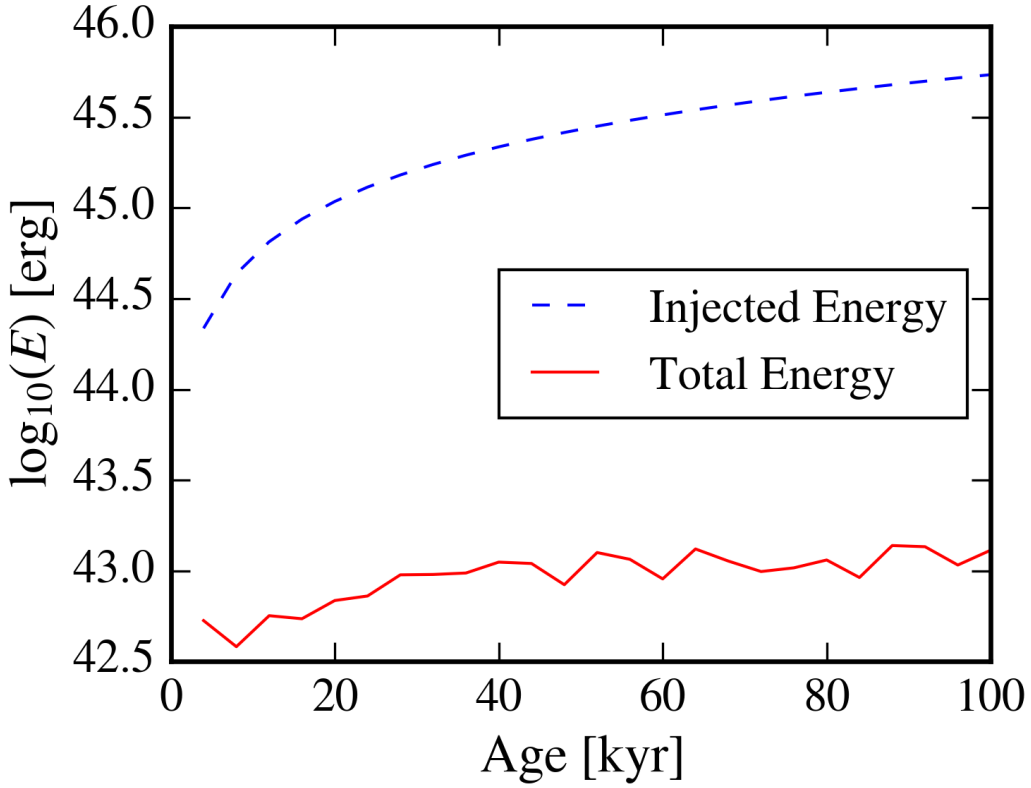

Fig. 3.6 The evolution of the injected energy (dashed blue curve) and the total energy within the shocked stellar wind region (solid red curve) for a model star of mass $M_\star = 12\,\mathrm{M}_\odot$ in a local hydrogen number density of $n_\star = 3.2 \times 10^4\,\mathrm{cm}^{-3}$.

approximation for this density:

$$\rho_{\rm i} = \left(\frac{R_{\rm st}}{D_{\rm i}(\frac{\pi}{2})}\right)^{3/2} \rho_{\star}\,, \tag{3.28}$$

where $D_{\rm i}(\frac{\pi}{2})$ is the measured radial distance from star to ionisation front given in tables 3.4 to 3.7 ($D_{\rm i}(\frac{\pi}{2})$ gives an "average" value for the bubble radius).

For all of the models the transition time is too short to be seen either because the earliest data snapshot was taken at 2 kyr or because the bubble is small and therefore not well resolved. As a result the bubbles quickly stall and consequently are missing the shock outside of the contact discontinuity that separates shocked stellar wind material and the ionised ambient medium.

As the shock is missing in all snapshots of all of the models and the wind-blown bubbles are behaving like radiative bubbles, the radial distance from the star to the contact discontinuity, $D_{\rm s}(\frac{\pi}{2})$ in tables 3.8 to 3.11, should be comparable to the analytical radius of the shock at the confinement time given in equation 3.27. The shell radius for a radiative bubble is given by

$$R_{\rm shell} = \left(\frac{3\mathscr{L}}{\pi\rho_{\rm i} v_{\infty}}\right)^{1/4} t^{1/2}\,, \tag{3.29}$$

so that the approximate final radius of the shocked wind region in the radial direction is

$$R_{\rm P} = R_{\rm shell}(t_{\rm P}) = \left(\frac{3\mathscr{L}}{4\pi\rho_{\rm i} c_{\rm i}^2 v_{\infty}}\right)^{1/2}\,, \tag{3.30}$$

which is also given for each model in tables 3.8 to 3.11. Looking at these tables, the measured transverse distances, $D_{\rm s}(\frac{\pi}{2})$, show close agreement with the confinement radius, $R_{\rm P}$, for stars with masses $M_{\star} \geq 20$. In tables 3.8 and 3.9 and tables 3.10 and 3.11, we can see generally better agreement for stars in lower density environments and at later times respectively.

In all the models the contact discontinuity eventually stalls (possible explanations are given earlier in the text). For stars with mass $6\,\mathrm{M}_\odot \leq M_\star \leq 30\,\mathrm{M}_\odot$ in tables 3.10 and 3.11 the stellar wind size in the transverse direction, $D_\mathrm{s}(\frac{\pi}{2})$, plateaus before they reach an age of 100 kyr. This behaviour is easily seen for the star with mass $M_\star = 30\,\mathrm{M}_\odot$ but is harder to see for lower-mass stars because the interface between the shocked stellar wind region and the ionised ambient region is unstable.

3.3.3 Emission Measures

In order to see what the models would look like if the ionised region were optically thin the emission measure was calculated:

$$EM = \int n_\mathrm{e}^2 \, ds \,, \tag{3.31}$$

where n_e is the number density of free electrons and the integration is along a line of sight.

To do this integration I used the cylindrically symmetric ray tracing scheme presented in the appendix of Dougherty et al. (2003). Grids of the resulting emission measures at a viewing projection angle of 45° are shown spanning two-dimensional parameter spaces in figures 3.7 to 3.10. In figures 3.7 and 3.8 the effects of varying stellar mass and the star's local density were explored at a time of 50 kyr. The evolution over time of emission measures for different stellar masses is plotted in figures 3.9 and 3.10 at a local number density of $n_\star = 3.2 \times 10^4\,\mathrm{cm}^{-3}$.

The figures show that for stars with mass $M_\star \leq 9\,\mathrm{M}_\odot$ the morphology of the cavity blown out by the stellar wind is unstable. This is also seen for $M_\star = 12\,\mathrm{M}_\odot$ and $n_\star > 3.2 \times 10^4\,\mathrm{cm}^{-3}$. However, these cavities are very small and would not be resolved in real radio continuum images. At higher stellar masses, $15\,\mathrm{M}_\odot \leq M_\star \leq 40\,\mathrm{M}_\odot$, the morphology of the HII regions do not change appreciably over a period of 200 kyr and all show limb-brightening. Stars with masses $M_\star \geq 70\,\mathrm{M}_\odot$ also show

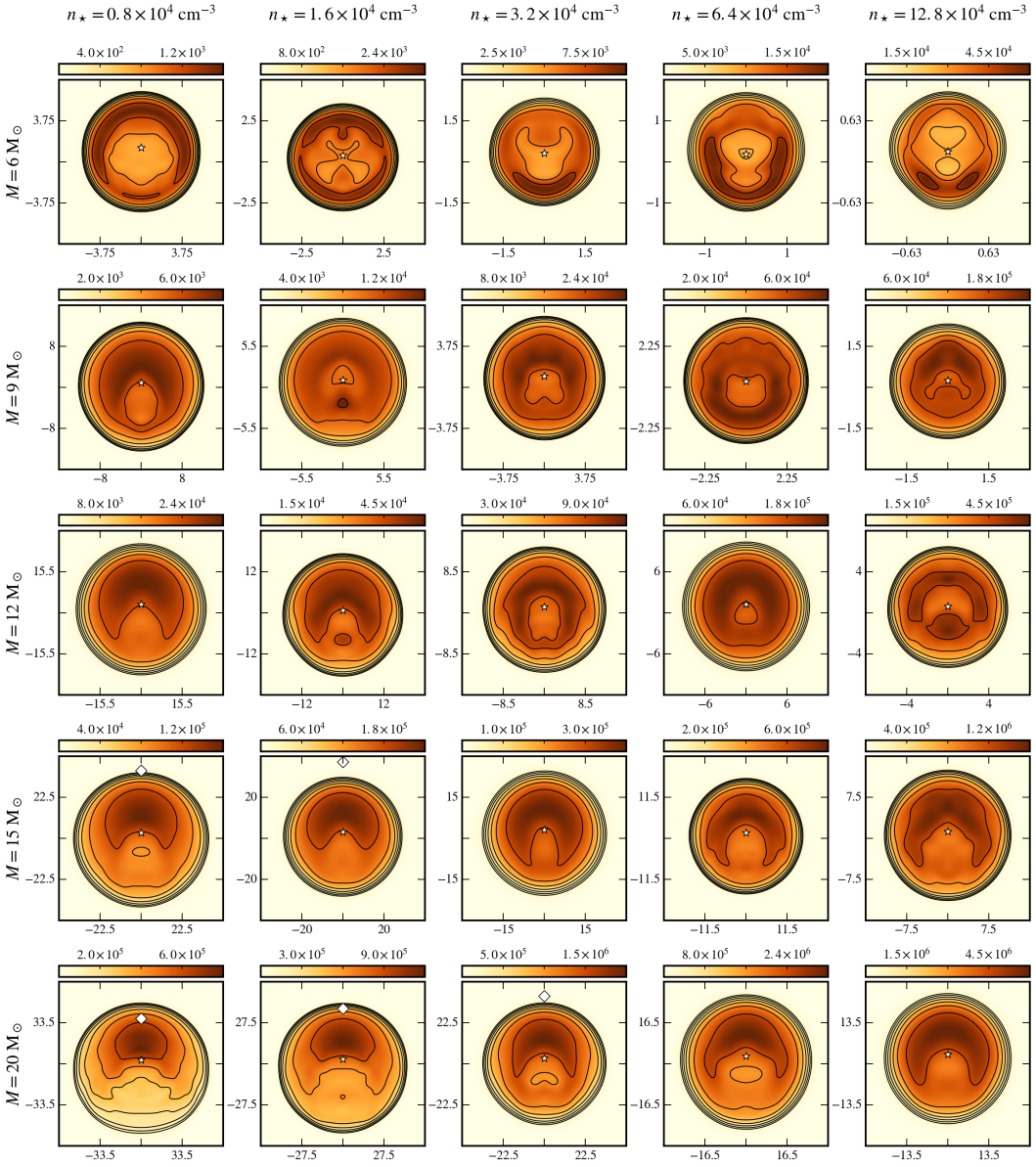

Fig. 3.7 The emission measures (in pc cm^{-6}) of simulated UCHII regions at an age of $t = 50\,000$ yr and viewed at a projection angle (see equation 3.32) of $\theta_\mathrm{i} = 45°$. Each row shows the emission measure for a star of a specified stellar mass (given on the far left) at increasing local number densities going right (number densities are given at the top of each column). The axes are in units of arcseconds and the object is assumed to be at a distance of 1.5 kpc from the observer. Each map also shows logarithmic contours at $\sqrt{2}$ intervals from the maximum emission measure. The star marker on each plot shows the position of the star and the diamond marker (where visible) shows the position of the cloud centre.

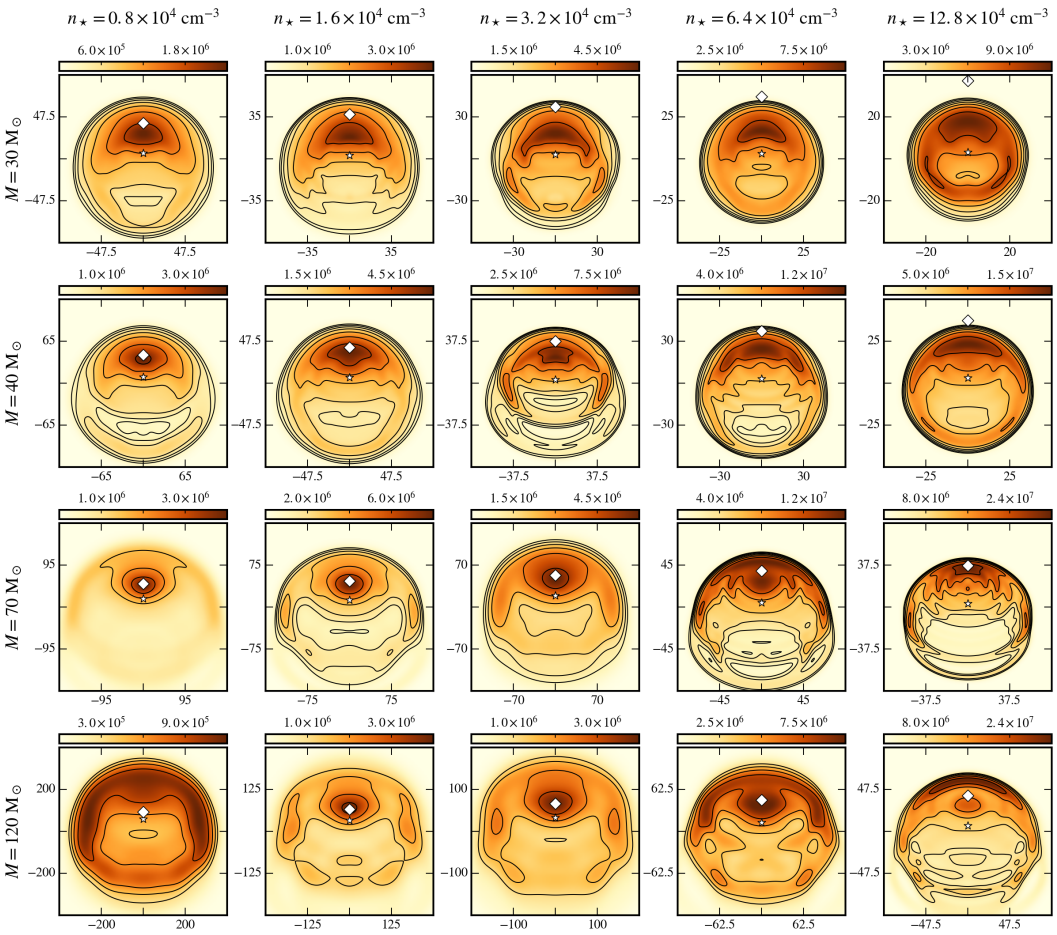

Fig. 3.8 Same as for figure 3.7 but for higher stellar masses.

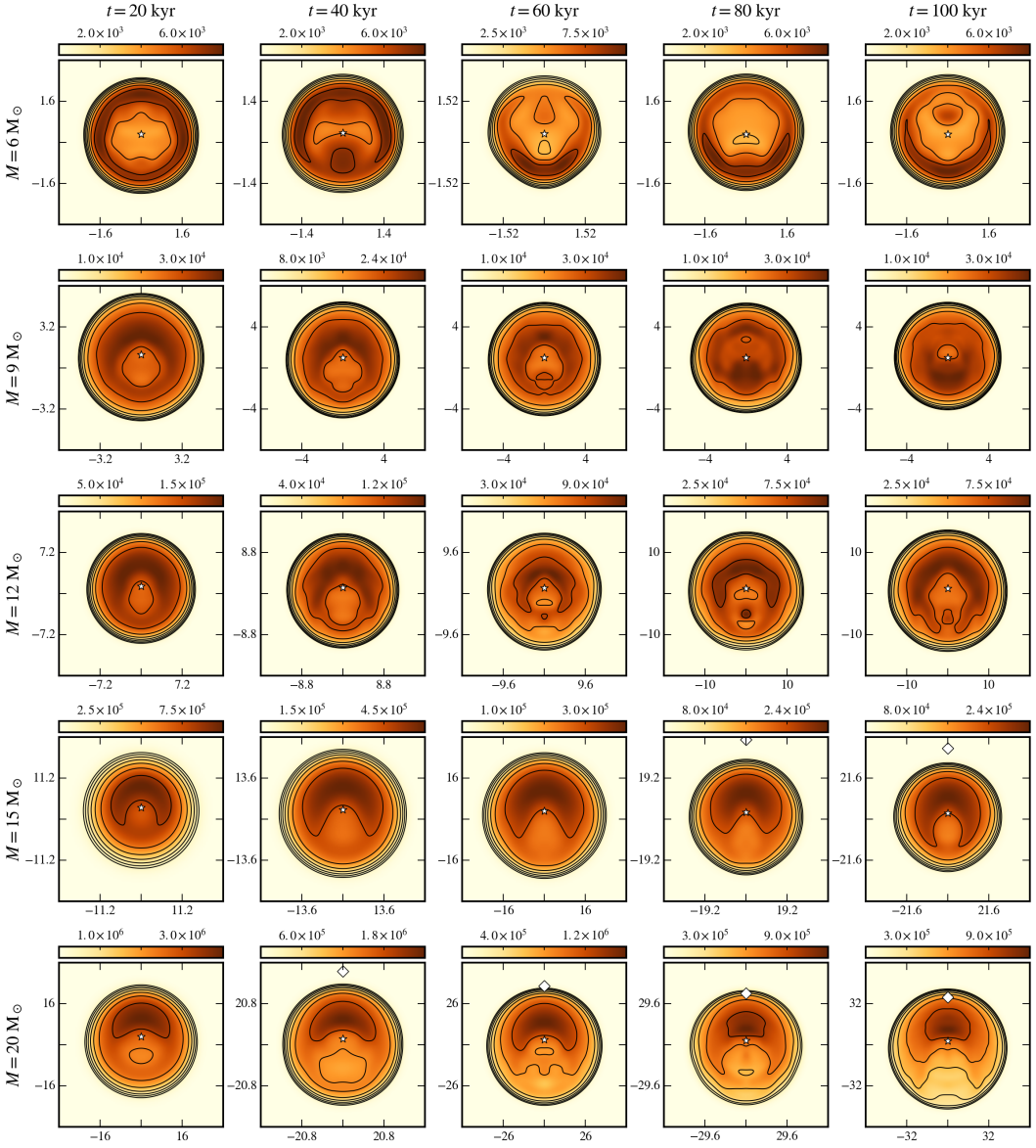

Fig. 3.9 The emission measures (in pc cm^{-6}) of simulated UCHII regions in a local hydrogen number density of $n_\star = 3.2 \times 10^4\,\mathrm{cm}^{-3}$ and viewed at a projection angle (see equation 3.32) of $\theta_\mathrm{i} = 45°$. Each row shows the emission measure for a star of a specified stellar mass (given on the far left) at ages going right (age is given at the top of each column). The axes are in units of arcseconds and the object is assumed to be at a distance of 1.5 kpc from the observer. Each map also shows logarithmic contours at $\sqrt{2}$ intervals from the maximum emission measure. The star marker on each plot shows the position of the star and the diamond marker (where visible) shows the position of the cloud centre.

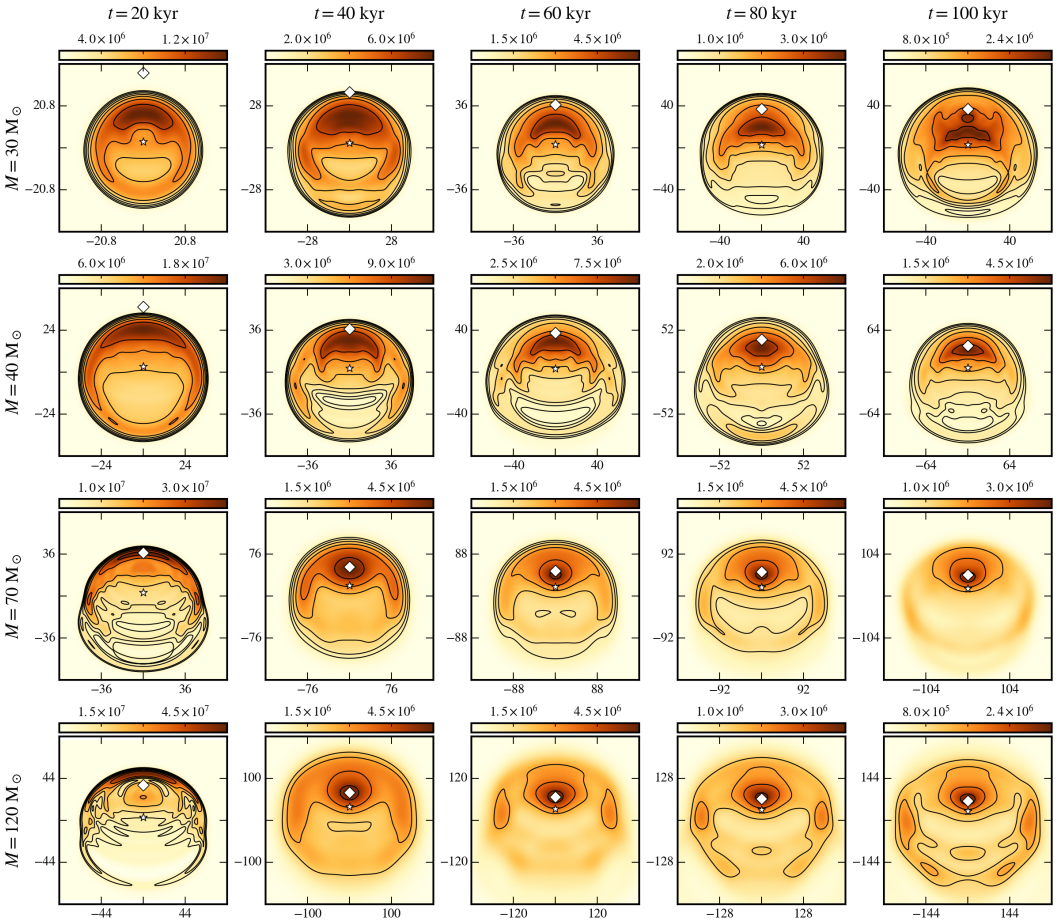

Fig. 3.10 Same as for figure 3.9 but for higher stellar masses.

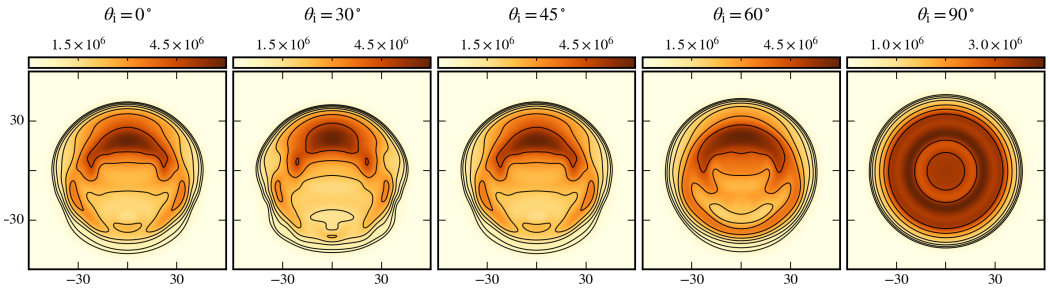

Fig. 3.11 The emission measures (in pc cm^{-6}) of a simulated HII region around a star with mass $M_\star = 30\,\mathrm{M}_\odot$ in a local hydrogen number density of $n_\star = 3.2\times10^4\,\mathrm{cm}^{-3}$ at an age of $t = 50\,\mathrm{kyr}$ viewed at different projection angles (see equation 3.32), which are given at the top of each plot. The axes are in units of arcseconds and the object is assumed to be at a distance of 1.5 kpc from the observer.

limb-brightening if $n_\star > 3.2\times10^4\,\mathrm{cm}^{-3}$. The rest have HII regions that expand past the centre of the dense cloud so that this is the only feature picked up in the emission measure images. For the HII region in the lower left of figure 3.8 we see limb-brightening because the high density core is destroyed by the stellar wind.

For one of the models that does exhibit limb-brightening and has a cavity that is larger than the wind injection region I show in figure 3.11 the effects of changing the projection angle on the morphology. The projection angle is defined as

$$\theta_\mathrm{i} = \arccos\left(\hat{z}\cdot\hat{d}\right), \tag{3.32}$$

where $\hat{z}$ is a unit vector directed from star to cloud centre and $\hat{d}$ is a unit vector directed from star to observer. At projection angles closer to 90° limb-brightening is more pronounced i.e. the "limbs" wrap further around the centre of the object. Using the classification scheme of De Pree et al. (2005) the projected morphology is less cometary and more shell-like the closer the axis of symmetry of the HII region is oriented towards the observer. These results suggest that HII regions classified as having a shell-like morphology may be cometaries viewed along their axis of symmetry (as noted by Mac Low et al., 1991).

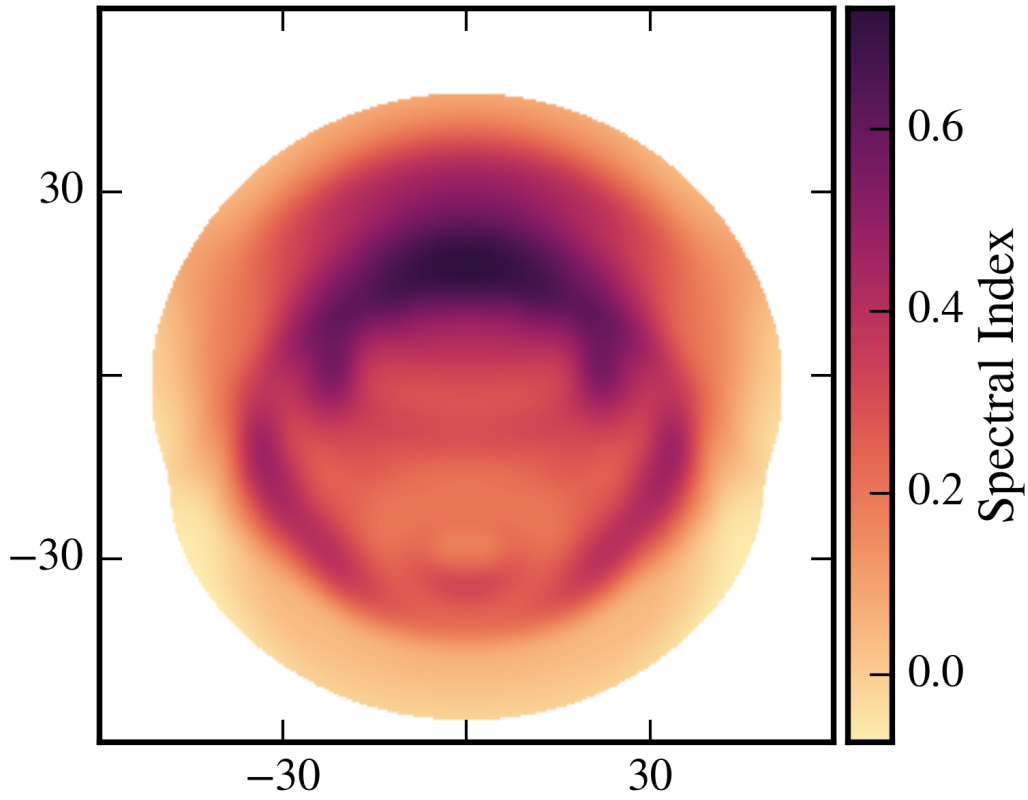

Fig. 3.12 A spectral index map of radio continuum emission from a model HII region around a star of mass $M_\star = 30\,\mathrm{M}_\odot$ in a local hydrogen number density of $n_\star = 3.2 \times 10^4\,\mathrm{cm}^{-3}$ and at an age of $t = 50\,\mathrm{kyr}$. The object was viewed at a projection angle (see equation 3.32) of $\theta_\mathrm{i} = 45°$. Spectral indices for each pixel were calculated using two flux density images of the model for frequencies of 1.4 GHz and 5.0 GHz. The axes are in units of arcseconds and the object is assumed to be at a distance of 1.5 kpc from the observer. The region in white is below the noise level of the CORNISH survey ($\sim 0.4\,\mathrm{mJy\,beam}^{-1}$) so a spectral index was not calculated. The integrated spectral index of this image is $\alpha = 0.36$ (see table 3.12).

3.3.4 Spectral Indices

Synthetic radio continuum maps (including the effects of optical depth) were also calculated using the emissivity and absorption coefficient in section 2.4.1. A spectral index map for radio continuum emission is plotted in figure 3.12 for a star in the centre of the parameter space for frequencies 1.4 GHz and 5.0 GHz. As expected the intermediate spectral indices (between -0.1 and 2) are found at the head and the limbs of the HII region, where the emission measure is highest. The cavity blown

Table 3.12 Spectral indices of model HII regions at an age of 50 kyr and viewing projection angle (see equation 3.32) of $\theta_i = 45°$. The spectral indices were calculated using total fluxes for each model at frequencies of 1.4 GHz and 5.0 GHz.

$M_\star$	$n_\star$ [10^4 cm^{-3}]				
[$M_\odot$]	0.8	1.6	3.2	6.4	12.8
6	−0.11	−0.11	−0.10	−0.10	−0.10
9	−0.10	−0.10	−0.10	−0.09	−0.07
12	−0.10	−0.10	−0.09	−0.07	−0.03
15	−0.09	−0.07	−0.05	−0.01	0.07
20	−0.03	0.02	0.10	0.21	0.38
30	0.08	0.20	0.36	0.56	0.83
40	0.15	0.30	0.49	0.76	1.04
70	0.12	0.30	0.36	0.78	1.08
120	0.04	0.16	0.27	0.66	1.05

Table 3.13 Spectral indices of model HII regions in a local hydrogen number density of $n_\star = 3.2 \times 10^4\,\mathrm{cm}^{-3}$ and viewing projection angle (see equation 3.32) of $\theta_\mathrm{i} = 45°$.

$M_\star$	Age [kyr]				
[$\mathrm{M}_\odot$]	20	40	60	80	100
6	−0.10	−0.10	−0.10	−0.10	−0.10
9	−0.10	−0.10	−0.10	−0.10	−0.10
12	−0.08	−0.09	−0.09	−0.09	−0.09
15	0.01	−0.04	−0.06	−0.07	−0.07
20	0.35	0.14	0.07	0.03	0.00
30	0.82	0.45	0.29	0.19	0.14
40	1.10	0.62	0.43	0.31	0.23
70	1.13	0.46	0.32	0.22	0.17
120	0.94	0.38	0.21	0.14	0.10

out by the stellar wind has a spectral index of 0.1 for radiation at radio wavelengths, which is lower than the head and the limbs.

Table 3.12 shows the spectral indices of models for a range of local densities and masses. These indices were calculated using the total radio continuum flux of each model for frequencies of 1.4 GHz and 5.0 GHz. At these frequencies the objects are more optically thick the higher the stellar mass (this is also seen in table 3.13). Higher-mass stars have more intense ionising radiation and blow stronger winds so they ionise deeper into the dense cloud leading to a higher proportion of the total flux from areas of high density. For masses $M_\star > 40\,\mathrm{M}_\odot$ the spectral indices decrease, which is likely due to the competing effect of larger regions having a higher proportion of flux from optically thin regions. These stars are ionising the regions around the densest part of the cloud (or through it in the case of the star with $M_\star = 120\,\mathrm{M}_\odot$ in a local density of $n_\star = 12.8 \times 10^4\,\mathrm{cm}^{-3}$).

In table 3.13 spectral indices are shown to decrease over time. HII regions (after their initial Strömgren expansion phase) expand according to equation 3.24 so that the pressure and density in this region decrease, and hence the spectral indices should decrease also.

Figure 3.13 shows the radio spectrum of one of the model HII regions and also a HII region that is produced by the same star but in a uniform density environment. Surprisingly, the turn-over frequency is very similar for the power-law case, but it is slightly lower because the HII region covers more low density gas down the slope than high density gas up the slope. The total fluxes have a higher proportion from lower density gas and therefore the integrated spectral indices will lean closer to indices from lower density regions. The close similarity between the SEDs is consistent with the fact that the density slope of ionised gas is much shallower than the initial slope in the neutral ambient gas.

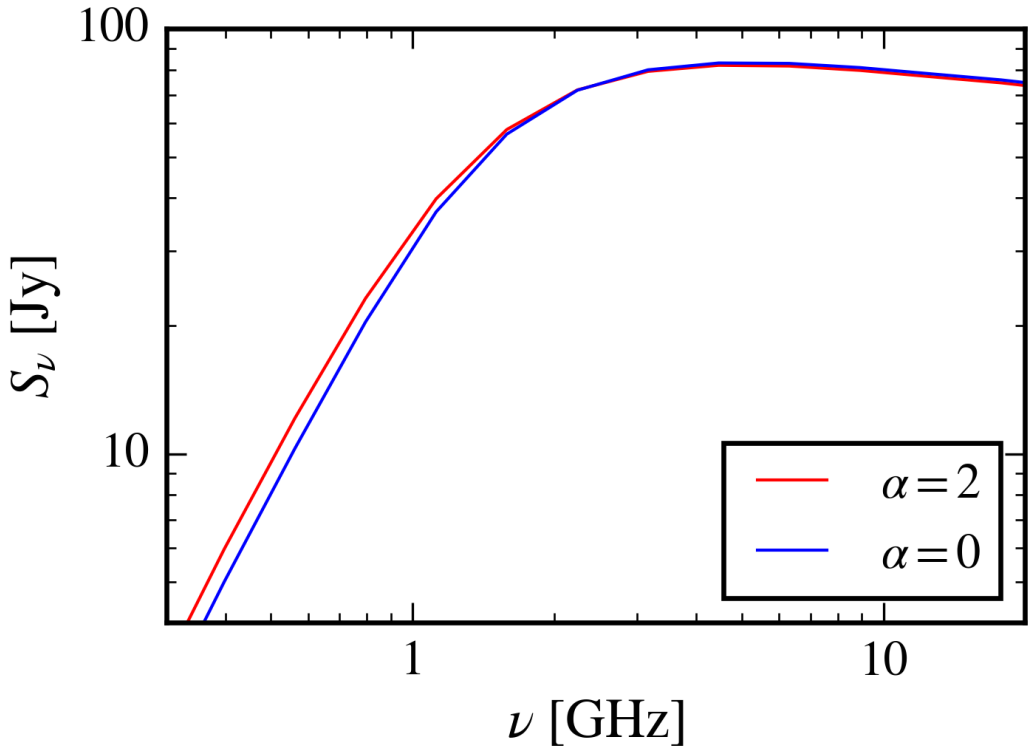

Fig. 3.13 The radio spectrum of two model HII regions around stars of mass $M_\star = 30\,\mathrm{M}_\odot$ with a local hydrogen number density of $n_\star = 3.2 \times 10^4\,\mathrm{cm}^{-3}$ at an age of $t = 50\,\mathrm{kyr}$ and at a projection angle (see equation 3.32) of $\theta_\mathrm{i} = 45°$. One of the stars is in a power-law density environment, $\alpha = 2$, and the other is in a uniform density environment, $\alpha = 0$. Both objects were viewed at a projection angle of $\theta_\mathrm{i} = 45°$ and assumed to be at a distance of 1.5 kpc.

3.4 Conclusions

Cometary HII regions were simulated that result from stars that blow stellar winds and are placed off-centre from a power-law density gas cloud. All of the models produce limb-brightening. Some are diminished if the star's HII region contains the dense centre of the cloud (which is true for stars with high Lyman output near low density clouds). There is a cavity blown out by the stellar wind in each model, which is observed in real cometary HII regions. The morphological class of a HII region depends on the viewing projection angle. Morphologies are more shell-like the smaller the angle between the viewing direction and the object's axis of symmetry. Spectral indices are higher for higher-mass stars, which can be explained as larger HII regions covering more of the high density gas near the cloud centre. This effect turns over at even higher masses as the volume of ionised low density gas increases more than the volume of ionised high density gas in the cloud centre. Model SEDs for power-law density models were almost identical to those of the same stars placed in uniform density surroundings, which is consistent with the shallow density structures found in the simulated ionised regions. The turn-over frequency in the radio spectrum for the power-law density models is slightly lower compared to the models with uniform ambient density. This is because HII regions in a power-law density medium cover more low density gas than high density gas, which means the proportion of emission from optically thin regions is higher.

If the effects of the entire spectrum of radiation from the model stars had been included the temperature structures of the resulting HII regions would be different. We would see higher temperatures near the ionisation front due to hardening of the radiation field (Wood and Mathis, 2004). The extra pressure due to these high temperatures is expected to be $\sim 20\,\%$ higher than in the HII regions I modelled. Another limitation of this model is that the initial thermal pressure of the neutral gas was taken to be uniform to prevent gas from moving away from the cloud centre

(which would happen if the temperature was uniform instead). In a future study the effects of gravity could be included to better model these environments.

In chapter 4 I use the grid of simulated models presented in this chapter to select HII regions that correspond to regions generated in a model Milky Way. The ultimate goal is to compare observables from this simulated survey with the CORNISH survey in order to investigate how well these models describe HII region evolution.

Chapter 4

Galaxy Population Synthesis

4.1 Introduction

In chapter 3 work on producing a grid of models of HII regions was presented. This chapter shows the results of incorporating said models into simulations of the CORNISH survey given prescriptions for the Galactic density distribution (Cordes and Lazio, 2002) and stellar accretion (McKee and Tan, 2003). This work builds on that of Davies et al. (2011), who tested different accretion models by comparing the luminosity distributions of YSOs (young stellar objects) from simulations of the RMS survey with that of the real RMS survey.

4.2 The Model

The code of Davies et al. (2011) was modified to generate the Galactic high-mass star population using an updated Galactic electron density distribution. The global SFR (star formation rate) of the Galaxy was assumed to be at a constant value of SFR $= 1.5\,\mathrm{M}_{\odot}\,\mathrm{yr}^{-1}$. This value lies in the range $1.5\,\mathrm{M}_{\odot}\,\mathrm{yr}^{-1}$ to $2.0\,\mathrm{M}_{\odot}\,\mathrm{yr}^{-1}$ predicted by the best-fit models of Davies et al. (2011), which were determined by reproducing the observed number of YSOs in the RMS survey with their population

synthesis model. At some point in the evolution of an UCHII region, the ionising star will have evolved such that it would not be included in the CORNISH survey. For this reason only stars with MS (main-sequence) age, $t_{\rm MS}$, below $t_{\rm max} = 800\,{\rm kyr}$ were selected.

With an assumed constant SFR and maximum MS age we can calculate the total mass of the distribution of young stars ($t < t_{\rm max}$) in the Galaxy as

$$M_{\rm tot} = {\rm SFR}\, t_{\rm max}\,. \tag{4.1}$$

Stars were generated one at a time, each with a final mass randomly selected from the IMF of Kroupa (2001), until the total mass of generated stars reached $M_{\rm tot}$. Each star was given a random age selected from a uniform random distribution with range $0\,{\rm kyr} < t \leq t_{\rm max}$. The current mass of each star was then found using the accretion model by McKee and Tan (2003).

4.2.1 Galactic Gas Distribution

A model for the Galactic free electron density structure, NE2001, was found by Cordes and Lazio (2002) who used pulsar dispersion measures and distances and radio-wave scattering measurements. They modelled the distribution of free electrons as a composition of thin disk, thick disk and spiral arm components. In this work, each generated star was given a specific location in the Galaxy that was randomly sampled to reproduce the Schmidt-Kennicutt law for star-forming galaxies (Kennicutt, 1998):

$${\rm SFR} \propto \Sigma_{\rm dens}^{1.4}\,, \tag{4.2}$$

where $\Sigma_{\rm dens}$ is the surface density of neutral gas in galaxies. The neutral gas density in the galaxy was assumed to have the same density structure as the free electrons and also assumed to be proportional to the surface density, $\rho \propto \Sigma_{\rm dens}$. This is a good

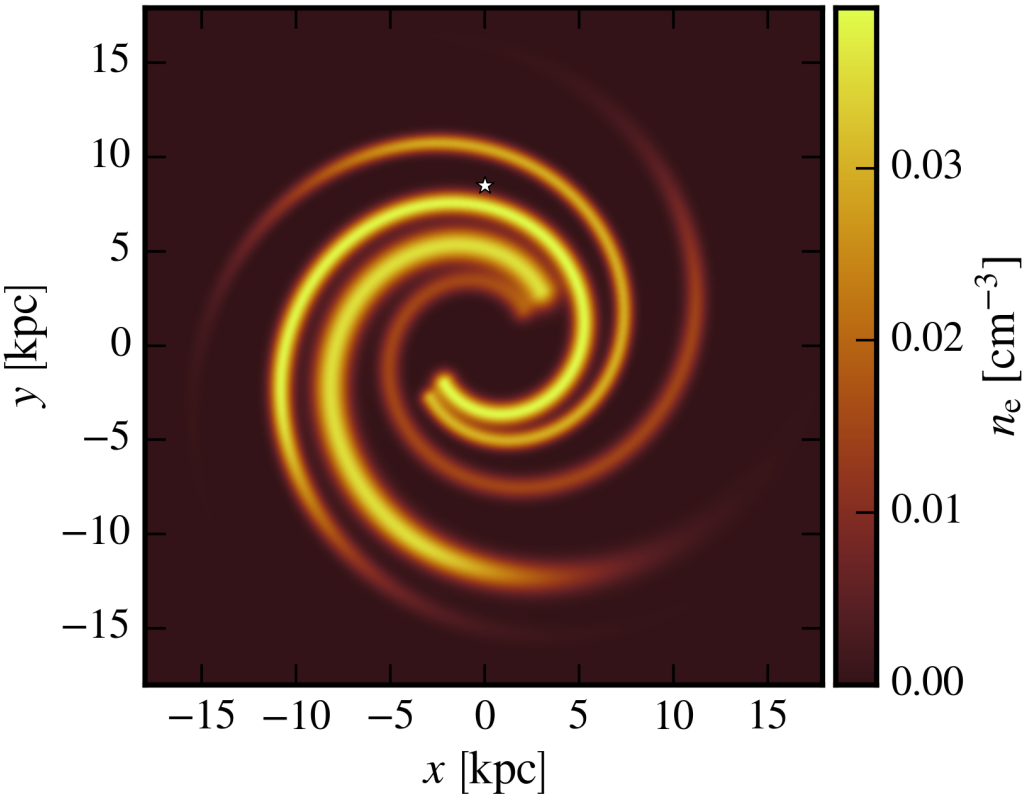

Fig. 4.1 Electron number density map of the $z = 0$ slice of the spiral arms in the Galaxy using the scheme in section 4.2.1. The star marker located at $(0\,\text{kpc}, 8.5\,\text{kpc})$ shows the position of the sun.

approximation if the scale height is uniform across the Galaxy and is small compared to the radius of the Galaxy.

In the simulations only the spiral arm component was included because this resulted in distributions of stars with longitudes, latitudes and distances from the sun that fit best with the UCHII regions in the CORNISH survey (see figure 4.1). The free electron density of spiral arm j is given by

$$n_{\mathrm{arm},j}(\vec{x}) = n_{\mathrm{a}} f_j \exp\left(-\left(\frac{s_j(\vec{x})}{w_j w_{\mathrm{a}}}\right)^2\right) \mathrm{sech}^2\left(\frac{z}{h_j h_{\mathrm{a}}}\right) S\left(\frac{r-A_{\mathrm{a}}}{2\,\mathrm{kpc}}\right), \tag{4.3}$$

where r and z are the Galactocentric distance and the distance from the Galactic plane respectively, $\vec{x}$ is the Cartesian position in the Galaxy, $n_{\mathrm{a}} f_j$ is the peak electron number density, $w_j w_{\mathrm{a}}$ is the half-width, $h_j h_{\mathrm{a}}$ is the scale height, and A_{a} is the radial cut-off. Fitted values of these parameters are found in Cordes and Lazio (2002). The functions $S(x)$ and $s_j(\vec{x})$ are given by

$$S(x) = \begin{cases} \mathrm{sech}^2(x), & \text{if } x \geq 0, \\ 1, & \text{if } x < 0, \end{cases} \tag{4.4}$$

and

$$s_j(\vec{x}) = \left[(x-x_0)^2 + (y-y_0)^2\right]^{\frac{1}{2}}, \tag{4.5}$$

where $(x_0, y_0, 0)$ is the position on the spiral arm curve for spiral arm j that is closest to $(x, y, 0)$. The spiral arm curves are, in polar coordinates, given by

$$\theta_j = A_{\mathrm{sp},j} \log_{10}\left(\frac{r_j}{r_{\mathrm{min},j}}\right) + \theta_{0,j}, \tag{4.6}$$

where θ_j are the Galactocentric azimuthal angles, r_j are the Galactocentric distances, and $A_{\mathrm{sp},j}$ and $\theta_{0,j}$ are fitted parameters with values from Davies et al. (2011).

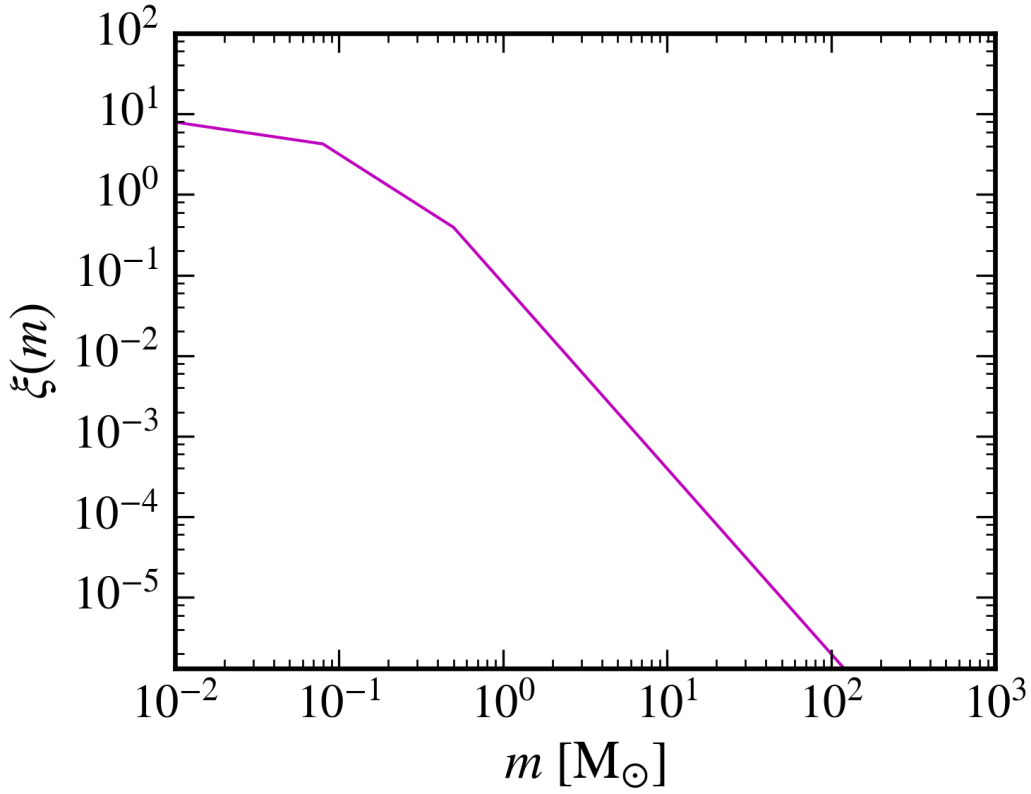

Fig. 4.2 The IMF by Kroupa (2001).

4.2.2 Stellar Population

The masses of each star in the generated population were determined using the multi-part power-law IMF by Kroupa (2001) with a cut-off at a stellar mass of $m = 120\,\mathrm{M}_\odot$:

$$\xi(m) \propto \begin{cases} m^{-0.3}, & 0.01 \leq m/\mathrm{M}_\odot \leq 0.08, \\ m^{-1.3}, & 0.08 \leq m/\mathrm{M}_\odot \leq 0.50, \\ m^{-2.3}, & 0.50 \leq m/\mathrm{M}_\odot \leq 120, \end{cases} \tag{4.7}$$

where $\xi(m)\Delta m$ is the probability that a star has a mass in range m to $m+\Delta m$ within a specified volume of space. Figure 4.2 shows a plot of this IMF.

To randomly generate a distribution of stars with IMF in equation 4.7 we first find which mass interval a random star belongs in. For a general multi-part power-law

distribution,

$$P_i(m) = A_i m^{-\alpha_i}, \quad m_i \leq m \leq m_{i+1}, \tag{4.8}$$

where $i = 0, 1, \ldots, N-1$ and N is the number of mass intervals. Using the requirement that the distribution is continuous, $P_i(m_i) = P_{i-1}(m_i)$, we have

$$A_i = A_{i-1} m_i^{\alpha_i - \alpha_{i-1}} = A_0 \prod_{j=0}^{i-1} m_{j+1}^{\alpha_{j+1} - \alpha_j}. \tag{4.9}$$

Given that a star definitely has a mass within the mass intervals of the multi-part power-law:

$$\sum_{i=0}^{N-1} P_i(m_i \leq m \leq m_{i+1}) = A_0 \sum_{i=0}^{N-1} \left[\left(\frac{m_{i+1}^{1-\alpha_i} - m_i^{1-\alpha_i}}{1-\alpha_i} \right) \prod_{j=0}^{i-1} m_{j+1}^{\alpha_{j+1} - \alpha_j} \right] = 1, \tag{4.10}$$

we have

$$A_0 = \frac{1}{\sum_{i=0}^{N-1} \left[\left(\frac{m_{i+1}^{1-\alpha_i} - m_i^{1-\alpha_i}}{1-\alpha_i} \right) \prod_{j=0}^{i-1} m_{j+1}^{\alpha_{j+1} - \alpha_j} \right]}, \tag{4.11}$$

giving us the probabilities that a random mass lies in each interval:

$$P_i(m_i \leq m \leq m_{i+1}) = A_0 \left(\frac{m_{i+1}^{1-\alpha_i} - m_i^{1-\alpha_i}}{1-\alpha_i} \right) \prod_{j=0}^{i-1} m_{j+1}^{\alpha_{j+1} - \alpha_j}. \tag{4.12}$$

Given the cumulative probabilities,

$$C_i = \sum_{j=0}^{i} P_j(m_j \leq m \leq m_{j+1}), \tag{4.13}$$

a star has a random mass that lies in mass range $m_k \leq m \leq m_{k+1}$ if C_k is the minimum cumulative probability such that $x < C_k$, where x is a value from random variable X, which is uniformly distributed over $[0, 1]$. Finally, we use inverse transform sampling to get the random mass within this interval:

$$m = \left[\left(m_{k+1}^{1-\alpha_k} - m_k^{1-\alpha_k} \right) y + m_k^{1-\alpha_k} \right]^{1/(1-\alpha_k)}, \tag{4.14}$$

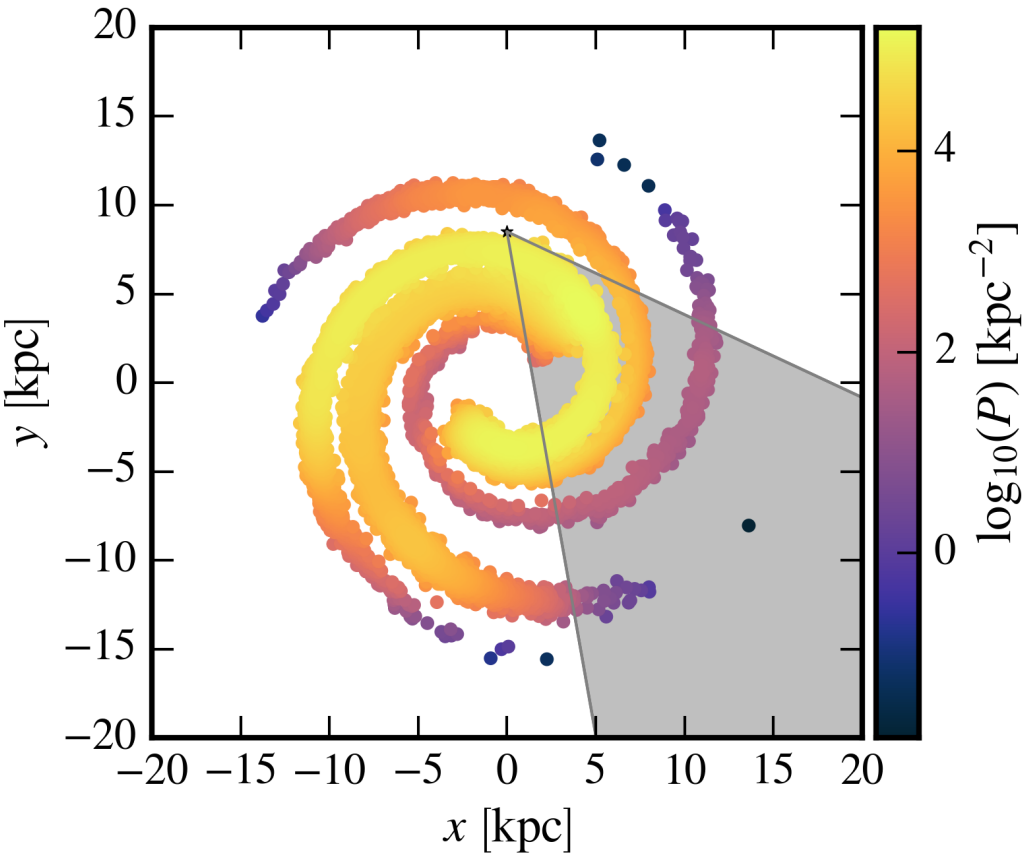

Fig. 4.3 Scatter plot of stars with mass $M_\star > 6\,\mathrm{M}_\odot$ generated for the model Galaxy. The colour map represents the logarithm of the population density. The star marker located at $(0\,\mathrm{kpc}, 8.5\,\mathrm{kpc})$ shows the position of the sun. The region shaded in grey is the CORNISH survey window ($10° < l < 65°$ and $|b| < 1°$).

where y is another value from the random variable X.

4.2.3 Accretion

Davies et al. (2011) found that simulations with accretion rates that increase as the stellar mass grows produced the best qualitative fits with the observed data. I therefore decided to use the turbulent core model by McKee and Tan (2002). According to the model an accreting star has an accretion rate given by

$$\dot{M} = 4.6 \times 10^{-4} \left(\frac{M_{\mathrm{fin}}}{30\,\mathrm{M}_\odot} \right)^{0.75} \left(\frac{\Sigma_{\mathrm{cl}}}{\mathrm{g\,cm^{-2}}} \right)^{0.75} \left(\frac{M_{\mathrm{cur}}}{M_{\mathrm{fin}}} \right)^{0.5} \quad \mathrm{M_\odot\,yr^{-1}}, \qquad (4.15)$$

where $M_{\rm cur}$ and $M_{\rm fin}$ are, respectively, the current and final mass of the star and $\Sigma_{\rm cl}$ is the surface density of a prestellar clump.

Equation 4.15 can be solved to get the stellar mass as a function of time:

$$M_{\rm cur}(t) = 1.76\times10^{-9}\left(\frac{M_{\rm fin}}{30\,{\rm M}_\odot}\right)^{0.5}\left(\frac{\Sigma_{\rm cl}}{{\rm g\,cm^{-2}}}\right)^{1.5}\left(\frac{t}{\rm yr}\right)^{2}\quad {\rm M}_\odot\,, \tag{4.16}$$

where t is the time since the star started accreting. From equation 4.16 we get the formation time, $t_{\rm form}$, for which $M_{\rm cur}(t_{\rm form}) = M_{\rm fin}$:

$$t_{\rm form} = 1.29\times10^{5}\left(\frac{M_{\rm fin}}{30\,{\rm M}_\odot}\right)^{0.25}\left(\frac{\Sigma_{\rm cl}}{{\rm g\,cm^{-2}}}\right)^{-0.75}\quad {\rm yr}\,, \tag{4.17}$$

McKee and Tan (2003) found that high-mass stars join the MS at approximately $20\,{\rm M}_\odot$. The time it takes for a star to accrete this mass is given by

$$t_{20} = 1.07\times10^{5}\left(\frac{M_{\rm fin}}{30\,{\rm M}_\odot}\right)^{-0.25}\left(\frac{\Sigma_{\rm cl}}{{\rm g\,cm^{-2}}}\right)^{-0.75}\quad {\rm yr}\,. \tag{4.18}$$

Using this accretion prescription the current mass of generated stars is given by

$$M_\star = \begin{cases} M_{\rm cur}\,, & \text{for } t < t_{\rm form}\,, \\ M_{\rm fin}\,, & \text{otherwise}\,. \end{cases} \tag{4.19}$$

The MS age of the each star is given by,

$$t_{\rm ms} = \begin{cases} t - t_{\rm form}\,, & \text{for } t > t_{\rm form} \text{ and } t_{\rm form} < t_{20}\,, \\ t - t_{20}\,, & \text{for } t > t_{20} \text{ and } t_{20} < t_{\rm form}\,, \\ 0\,, & \text{otherwise}\,. \end{cases} \tag{4.20}$$

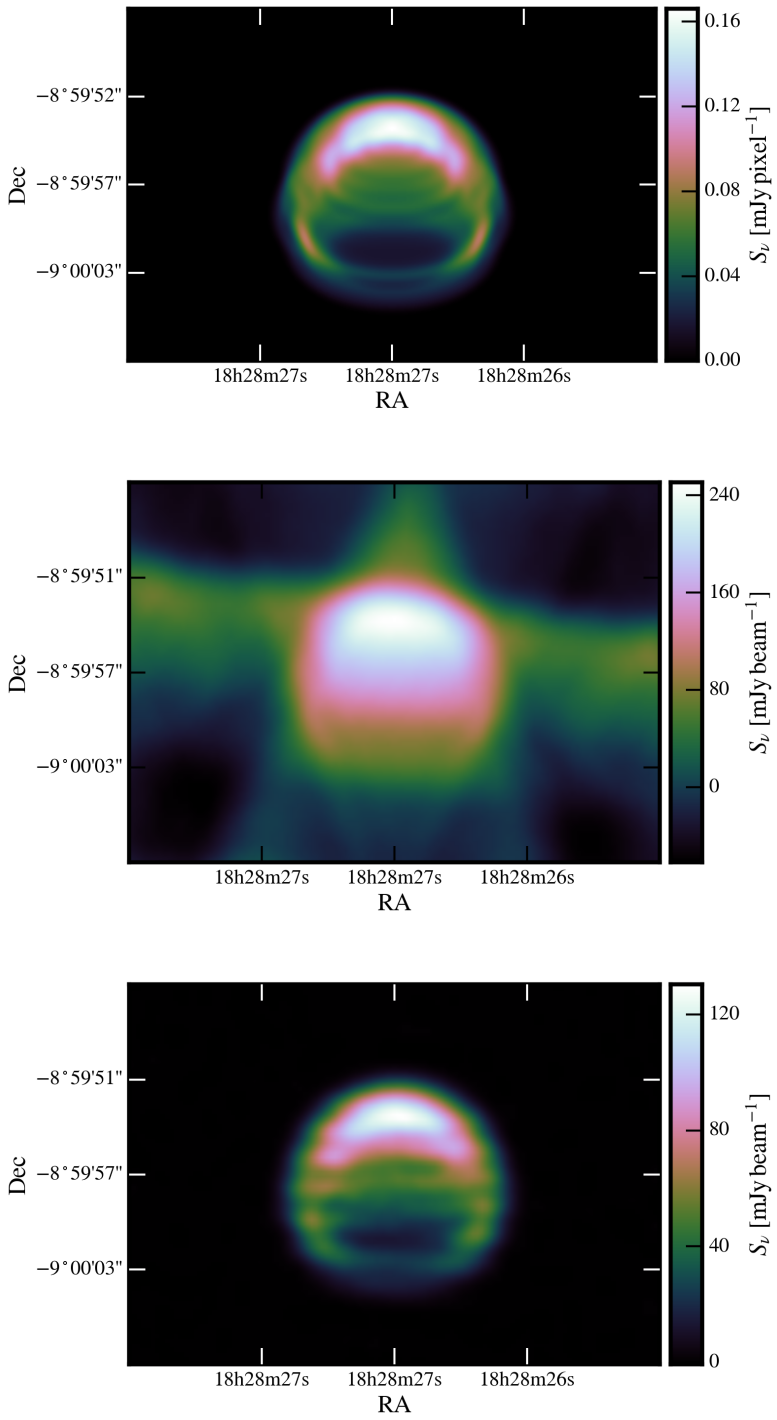

Fig. 4.4 Radio continuum images of a simulated cometary UCHII region included in the simulated survey with $n_\star = 6.4 \times 10^4\,\mathrm{cm}^{-3}$. The top plot shows the synthetic radio image of the model, the middle plot shows the image after being processed by CASA using the `simobserve` routine, and the bottom plot shows the CASA image after cleaning with the CASA's `clean` routine.

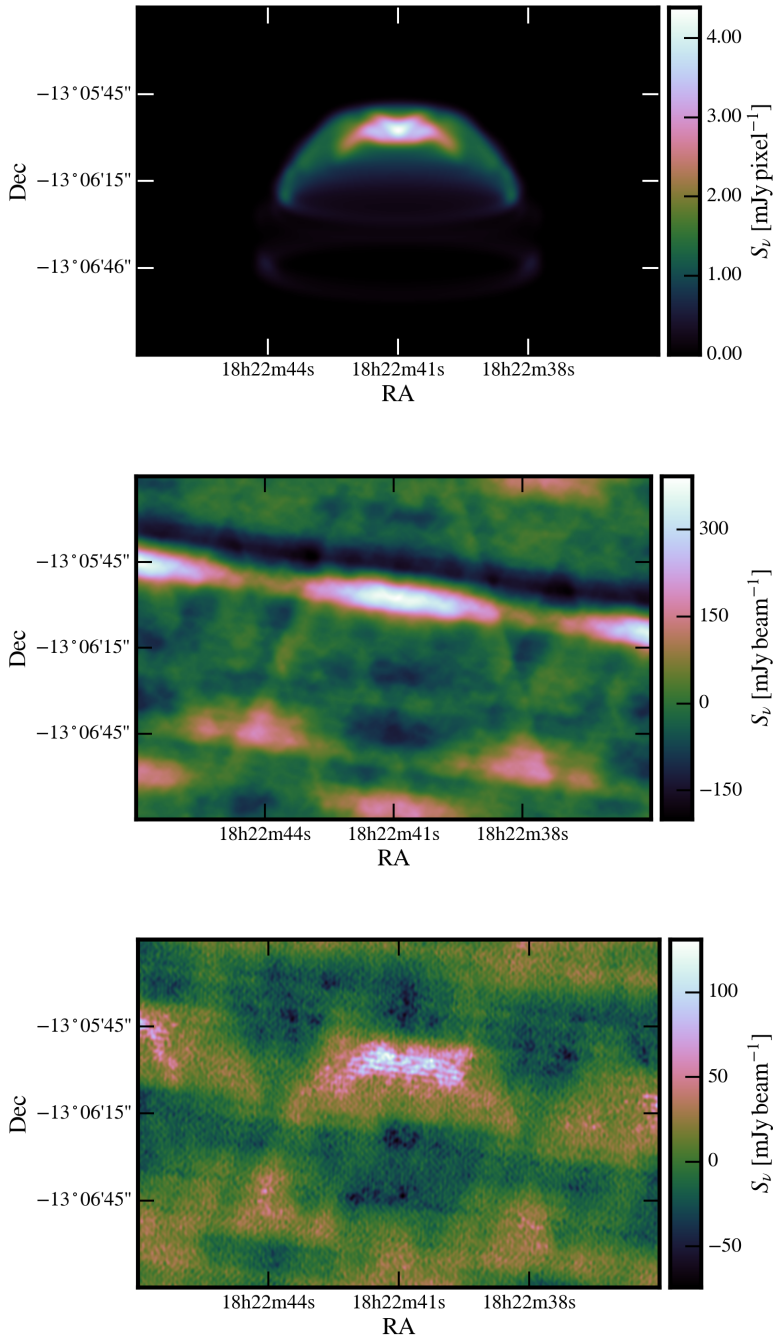

Fig. 4.5 Same as for figure 4.4 except the simulated cometary HII region is over-resolved. The object is too large to be included in the simulated surveys.

4.3 Results and Discussion

With the stellar population model described above I generated populations for the Galaxy (figure 4.3) and selected stars within the CORNISH survey window: $10° < l < 65°$ and $|b| < 1°$. For each selected star I calculated two synthetic radio continuum emission maps, at a random inclination angle, of stars with closest masses available from the model grid (see chapter 3) above and below the generated star's mass. This way values measured using these maps could be used to linearly interpolate the value corresponding to the generated star. The radio maps were calculated using the ray tracing scheme of Dougherty et al. (2003) and the emissivity and absorption coefficient in section 2.4.1. Snapshots of data from each HII region in the model grid were made at intervals of 2 kyr from 0 kyr to 200 kyr. The snapshot with the simulation time closest to the MS lifetime of the star was used to generate the radio maps. I used the snapshot at 200 kyr for stars older than the maximum available age in the model grid because almost all stars in the higher density surveys, with $n_\star \geq 6.4 \times 10^4\,\mathrm{cm}^{-3}$, produce UCHII regions that stagnate before this time. Therefore the snapshot data at 200 kyr is a good approximation to the model at later times. In the lower density surveys most of the stars are below this age anyway so this approximation was not necessary.

Simulated CORNISH observations were made of these radio maps using CASA (McMullin et al., 2007). See Hoare et al. (2012) and Purcell et al. (2013) for details on the observation and imaging parameters. HII regions with $\sigma < 7.0$ were removed (as was done in the CORNISH survey), where σ is the maximum pixel value of the CASA images divided by the RMS-noise. The RMS-noise was not uniform over the observation area: $\mathrm{RMS}_{\mathrm{outer}} = 0.25\,\mathrm{mJy\,beam}^{-1}$ for stars at declinations $\delta > 14.2°$ and $\mathrm{RMS}_{\mathrm{inner}} = 0.35\,\mathrm{mJy\,beam}^{-1}$ for stars elsewhere (Purcell et al., 2013). The lower sensitivity in the inner region during the 2006 season was due to electrical storms. In the 2007 season weather conditions were better and EVLA (Extended

VLA) antenna upgrades were utilised that have more sensitive receivers. However, observations during this time were made at low declinations and therefore through more atmosphere, which effectively increased the noise level. The outer region was mapped at higher declinations in overall better weather conditions and used the EVLA antennas.

For the remaining HII regions in the simulated survey I ran the `imfit` routine in CASA to fit Gaussians to the images in a similar way to Purcell et al. (2013). With these fits, I obtained estimates for the angular size and the integrated fluxes of the HII regions. Finally, HII regions were removed from the survey if their angular sizes were too large. In Purcell et al. (2013) the FWHM of fitted Gaussians was constrained to be $\leq 30''$, so this is also the maximum angular size in these simulated surveys.

A simulated radio continuum image of a cometary HII that would be included in the CORNISH survey is shown in figure 4.4 along with simulated observations of the image using CASA, before and after cleaning. Similarly, images of a HII region that is too large to be have been included in the CORNISH survey are shown in figure 4.5.

I simulated five surveys each assuming a different constant local number density, $n_\star$, available in the grid of models in chapter 3. In this section I present the results of simulating CORNISH surveys and compare distributions of UCHII region properties with those of the real CORNISH survey.

4.3.1 Numbers of UCHII Regions

In table 4.1 the numbers of UCHII regions in each of the five simulated surveys are shown along with the number of objects detected in CORNISH. We see a gradual increase in numbers as local density is increased because HII regions have smaller Strömgren radii and therefore are less likely to be excluded due to their sizes.

Table 4.1 The total number of UCHII regions, N, included in each of the simulated surveys of different local number density, $n_\star$, and the CORNISH survey.

$n_\star$ [cm^{-3}]	N
0.8×10^4	40
1.6×10^4	73
3.2×10^4	124
6.4×10^4	690
12.8×10^4	960
CORNISH	240

There is a sudden jump in the number of UCHII regions between the surveys with $n_\star = 3.2 \times 10^4\,\mathrm{cm}^{-3}$ and $n_\star = 6.4 \times 10^4\,\mathrm{cm}^{-3}$. The reason for this is that HII region stagnation becomes important at densities $n_\star > 3.2 \times 10^4\,\mathrm{cm}^{-3}$; the limiting sizes of HII regions in high density lie within the selection bounds of CORNISH.

4.3.2 Flux Distribution

In figure 4.6 integrated flux distributions are shown along with the CORNISH sample of UCHII regions for comparison. We see a peak in the distributions in the range 50 mJy to 200 mJy. The distributions tail off at low integrated flux as expected as these UCHII regions are less likely to have peak fluxes above the CORNISH selection threshold. At high integrated fluxes the distributions also tail off as higher fluxes tend to have larger angular sizes (see figure 4.8). Therefore, high integrated fluxes are more likely to come from over-resolved HII regions.

Simulated surveys at higher local densities have a higher overall number of selected UCHII regions because more stars are resolved due to smaller angular sizes. There is also a higher proportion of samples with low integrated flux in the simulated surveys with $n_\star = 6.4 \times 10^4\,\mathrm{cm}^{-3}$ and $n_\star = 12.8 \times 10^4\,\mathrm{cm}^{-3}$. This is probably because UCHII regions in dense enough environments stagnate at angular sizes small enough to be included in the CORNISH survey.

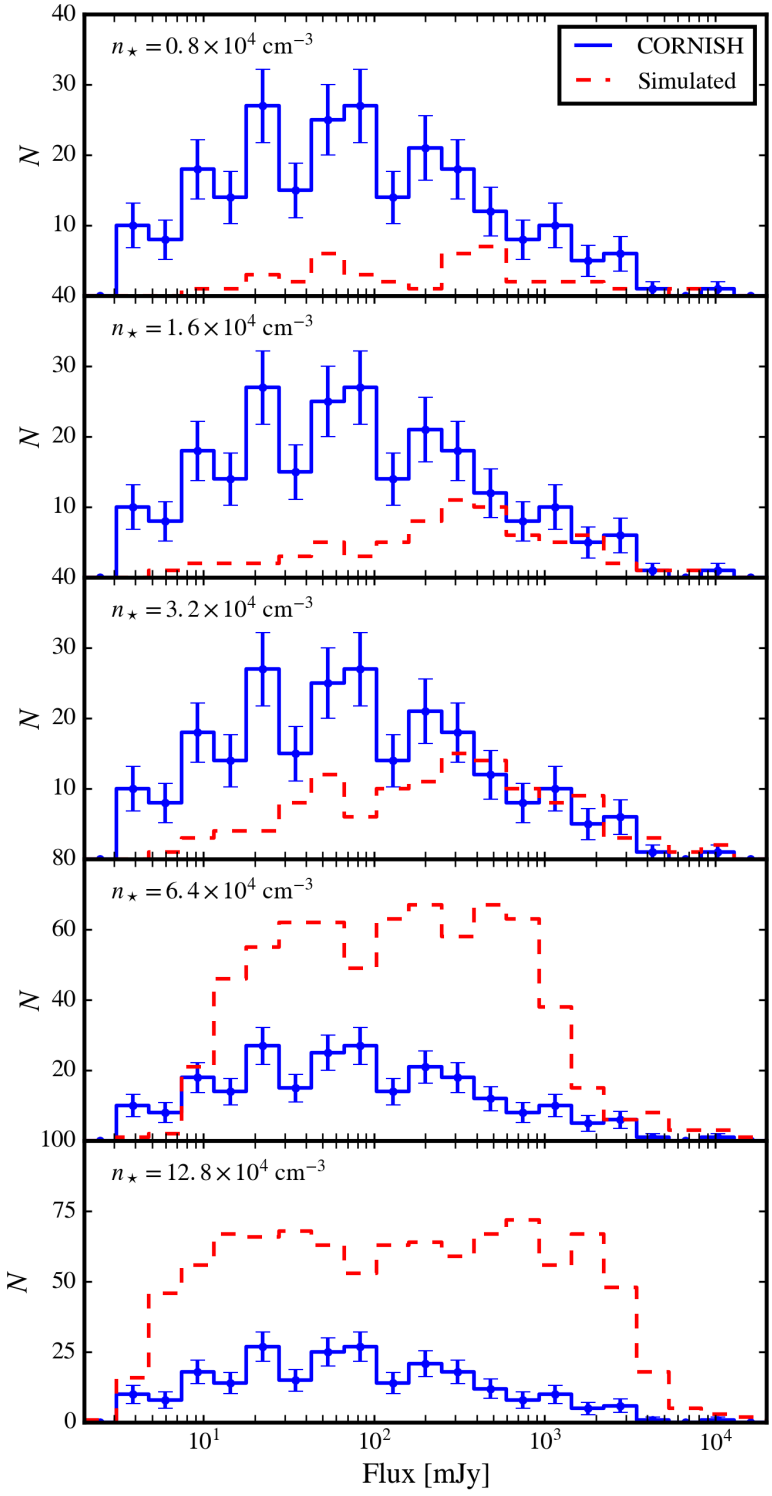

Fig. 4.6 Distributions of UCHII regions with integrated flux. The red histograms are distributions of simulated UCHII regions that would be included in the CORNISH survey and the blue histograms with error bars show the CORNISH sample. Each plot shows the simulated distributions for stars that begin in different local densities (values of which are given in the top left).

4.3.3 Size Distribution

Figure 4.7 shows the normalised distributions of stars in the simulated surveys at different local densities compared with the CORNISH sample. The distributions behave as expected: higher density HII regions have smaller Strömgren radii, leading to the shift we see in higher density distributions towards smaller sizes. Again, we see a better fit for distributions of stars in higher local densities. This indicates that, assuming the model is correct, most of the CORNISH UCHII regions are embedded in dense environments with $n_\star > 6.4 \times 10^4\,\mathrm{cm}^{-3}$.

In figure 4.8 scatter plots are shown of angular size against integrated flux of UCHII regions in each survey. The kernel density estimations, also in this figure, show a positive correlation between the two variables. We also see a positive correlation between stellar mass and integrated flux in figure 4.9, due to the fact that higher-mass stars, with their higher Lyman continuum fluxes, produce larger HII regions and therefore higher integrated fluxes.

4.3.4 Spatial Distribution

Simulated surveys were run for the densities available in the grid of models for different combinations of Galactic density components. Surveys that only include the spiral arm components gave the best fits to the CORNISH spatial distribution. This is consistent with the results of Davies et al. (2011) and gives yet further evidence that OB stars trace the spiral arms, which has been known since the 1950s (see Churchwell, 2002, and references therein).

Normalised distributions of simulated stars with longitude, latitude and distance from the sun are given in figure 4.10 for different local densities (the density of the gas near the stars before they start ionising gas and blowing a wind). We can see qualitatively better fits to the shape of the CORNISH histogram data the higher the local density. The distribution in longitude broadly matches well with that

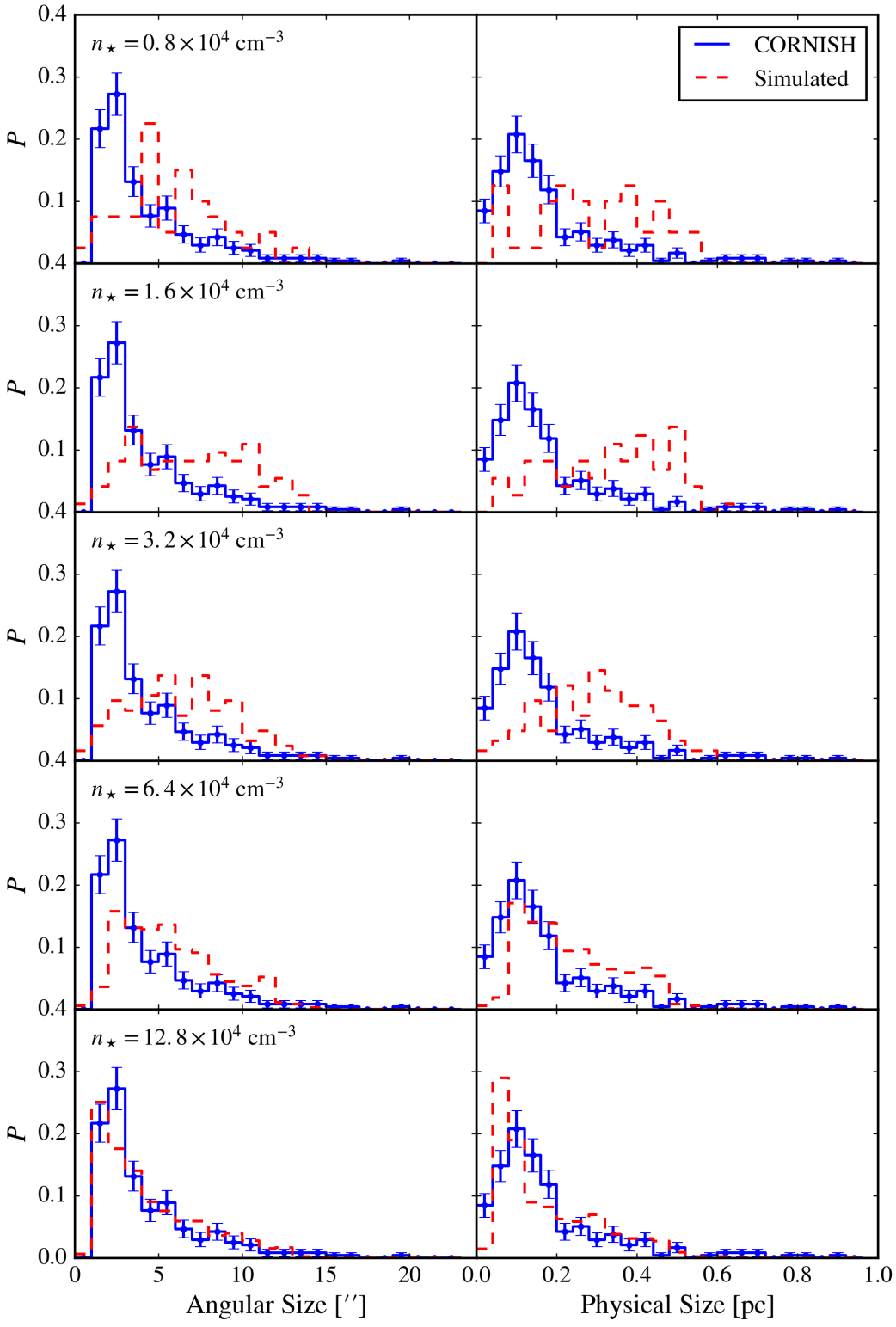

Fig. 4.7 Normalised distributions of UCHII regions with angular size (left) and physical size (right). The red histograms are distributions of simulated UCHII regions that would be included in the CORNISH survey and the blue histograms with error bars show the CORNISH sample. Each row shows the simulated distributions for stars that begin in different local densities (values of which are given in the top left of the left-most plots).

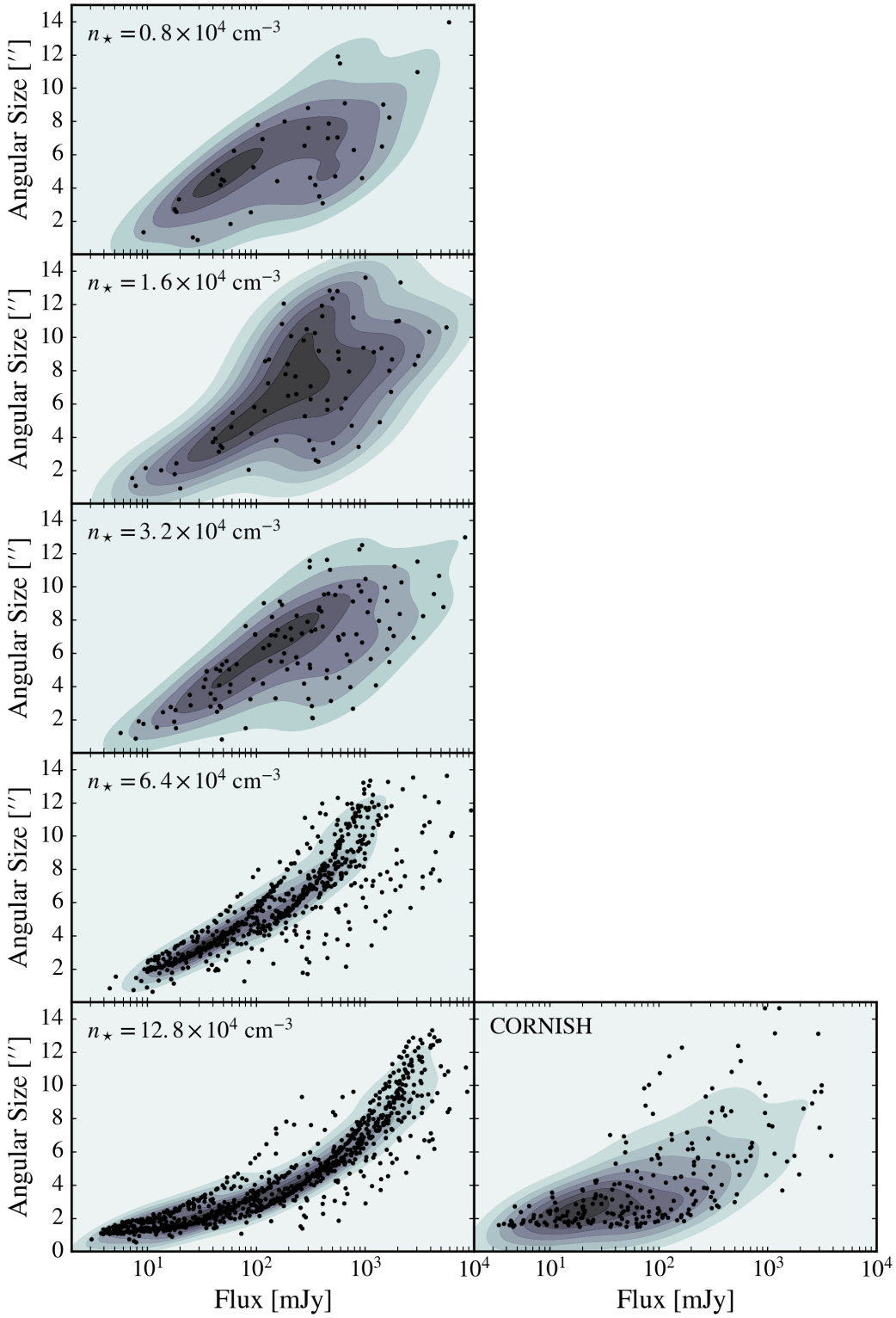

Fig. 4.8 Scatter plots of angular size against integrated flux for simulated surveys (left column) of stars that begin in different local densities (given in the top left of each plot) and the CORNISH survey (right). Points are plotted over a kernel density estimation, which uses Scott's Rule (Scott, 2010) for bandwidth selection.

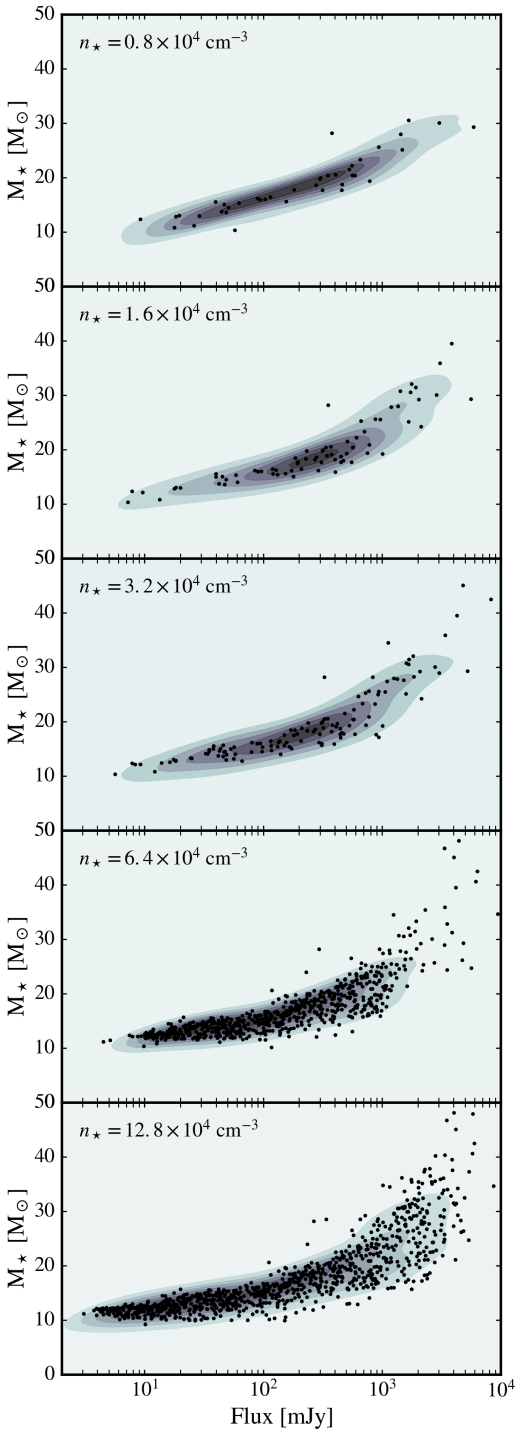

Fig. 4.9 Scatter plots of stellar mass against integrated flux for simulated surveys of stars that begin in different local densities (given in the top left of each plot). Points are plotted over a kernel density estimation, which uses Scott's Rule (Scott, 2010) for bandwidth selection.

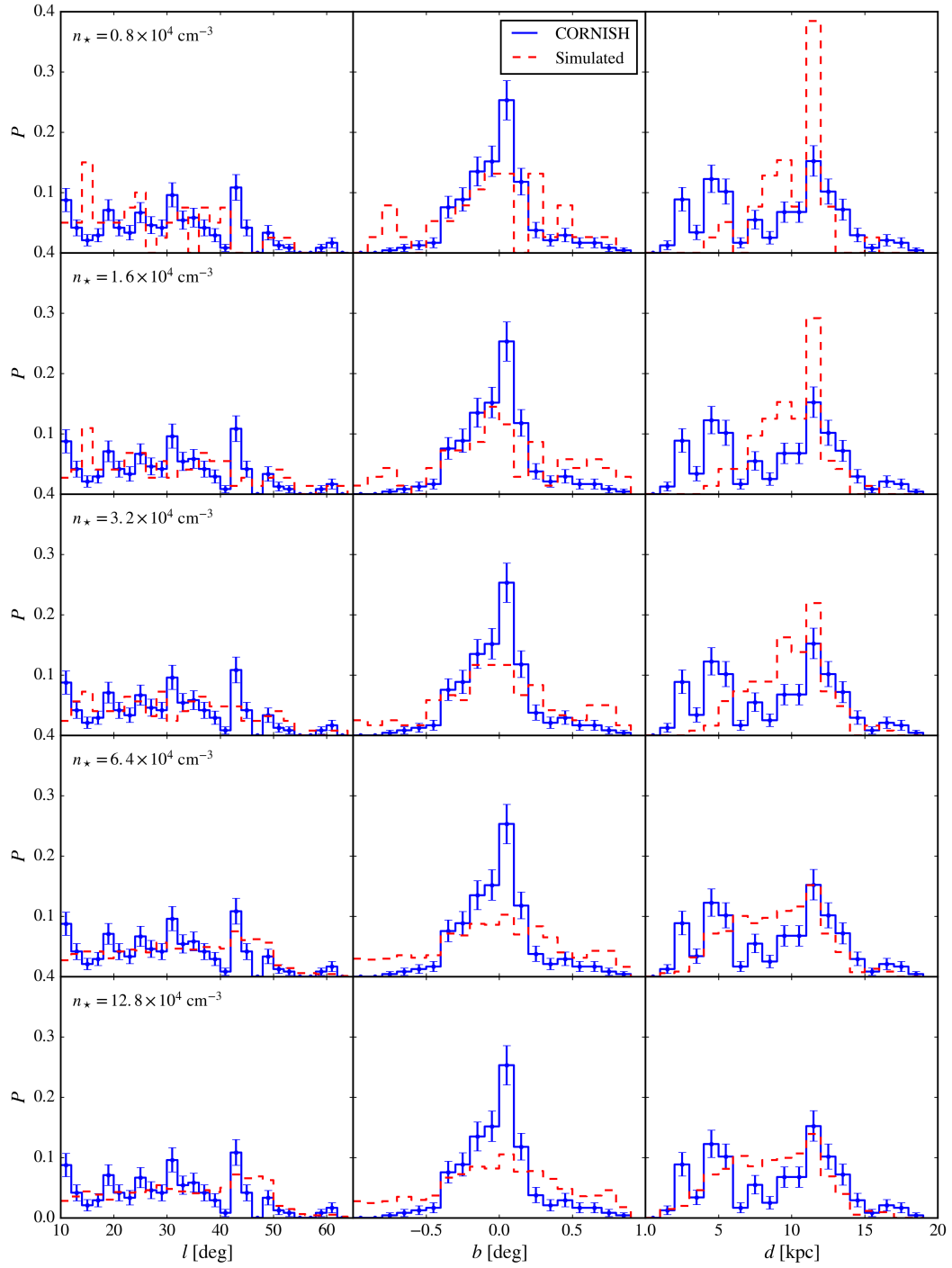

Fig. 4.10 Normalised distributions of UCHII regions with: galactic longitude, l (left); galactic latitude, b (middle); and distance from the sun, d (right). The red histograms are distributions of simulated UCHII regions that would be included in the CORNISH survey and the blue histograms with error bars show the CORNISH sample. Each row shows the simulated distributions for stars that begin in different local densities (values of which are given in the top left of the left-most plots).

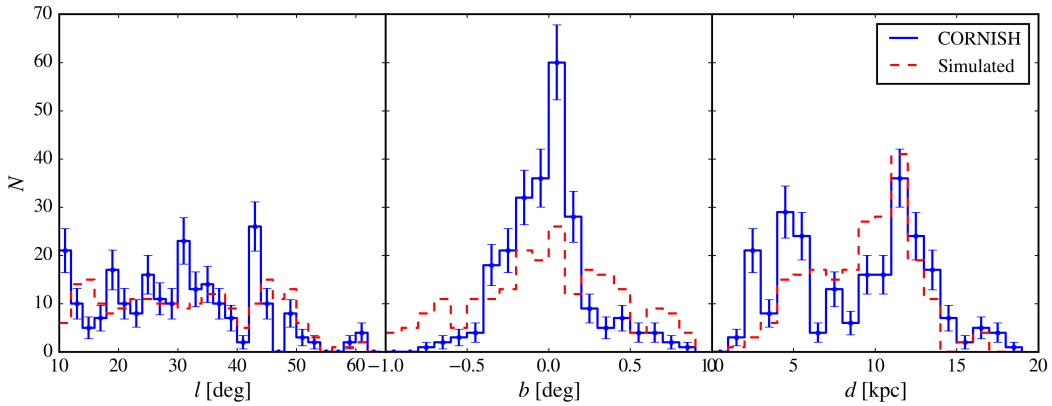

Fig. 4.11 Distributions of UCHII regions with: galactic longitude, l (left); galactic latitude, b (middle); and distance from the sun, d (right). The red histograms are distributions of simulated UCHII regions that would be included in the CORNISH survey and the blue histograms with error bars show the CORNISH sample. The simulated survey was compiled by sampling from a distribution of local densities as described in section 4.3.5.

observed however the scale heights of the simulations are higher than that seen in the CORNISH data.

The distribution of stars with distance from the sun is the most important histogram to look at as this is the only of the three in the figure that can affect distributions of flux and angular size. For the simulated surveys with lower local densities we do not see relatively many UCHII regions at $d = 5\,\mathrm{kpc}$ probably because even the low mass stars are producing HII regions that are too large to be selected by the CORNISH survey. The simulated survey with $n_\star = 12.8 \times 10^4\,\mathrm{cm}^{-3}$ has the closest fit to the CORNISH sample except that there are relatively more stars between $5\,\mathrm{kpc} < d < 12\,\mathrm{kpc}$.

4.3.5 Density Distribution

Although the simulated survey with the highest density fits the CORNISH data best, the total number of objects is a lot higher than observed. Reducing the SFR to $\mathrm{SFR} \simeq 0.5\,\mathrm{M}_\odot\,\mathrm{yr}^{-1}$ would lead to a better fit in normalisation but this value is quite low compared to the range that is accepted in the community (see Davies et al., 2011,

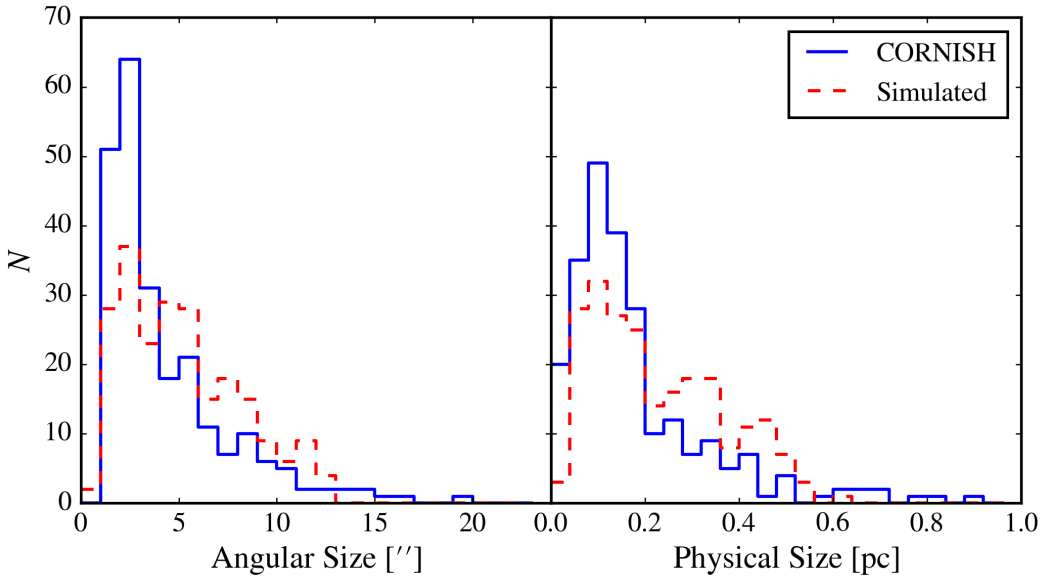

Fig. 4.12 Distributions of UCHII regions with angular size (left) and physical size (right). The red histograms are distributions of simulated UCHII regions that would be included in the CORNISH survey and the blue histograms with error bars show the CORNISH sample. The simulated survey was compiled by sampling from a distribution of local densities as described in section 4.3.5.

and references therein). Also we can see in figure 4.8 that the CORNISH UCHII regions have a broader range of angular sizes at any particular flux, which is also seen in the lower density surveys. This indicates that even though most of the CORNISH UCHII regions are embedded in high density environments, the overall number of HII regions in the Galaxy in these environments is relatively low compared to those in lower density environments. HII regions in high density environments are, however, more likely to be included in the CORNISH sample because they are smaller in size.

I tested this by randomly sampling HII regions from the simulated surveys. The probability of selecting a star from a survey with local density $n_\star$ was assumed to be

$$P(n_\star) \propto n_\star^{-q}, \tag{4.21}$$

where q is a power-law index. A few values of the index were tried: $q = 0$, $q = 0.5$ and $q = 1$, and $q = 0.5$ gave the closest fit. The distributions of observables for

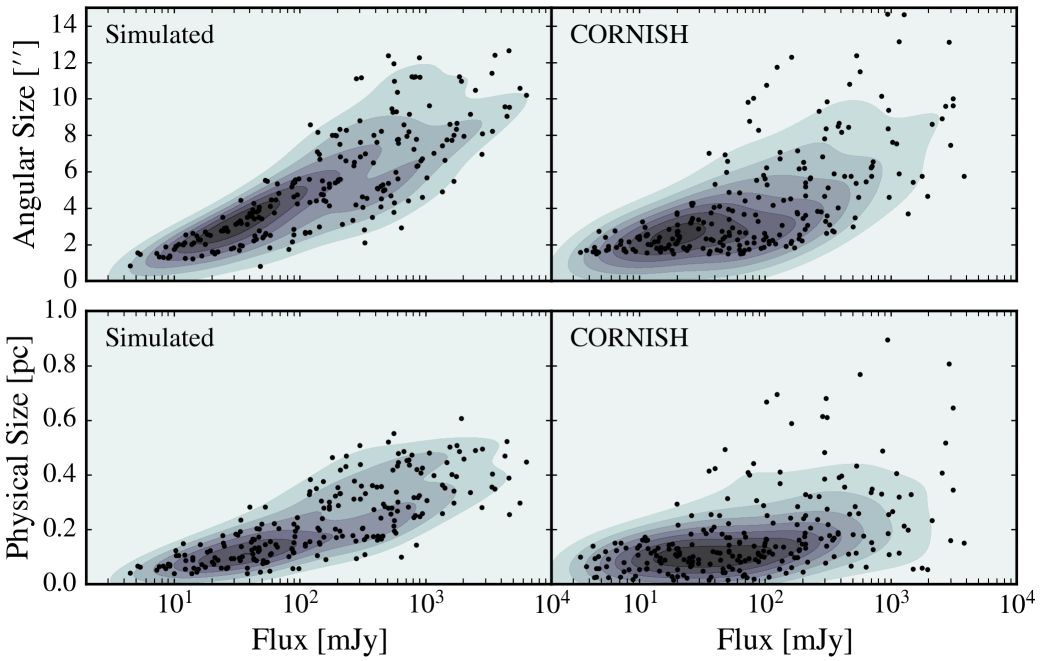

Fig. 4.13 Scatter plots of angular size (top row) and physical size (bottom row) against integrated flux for simulated UCHII regions (left) and UCHII regions in the CORNISH survey (right). Points are plotted over a kernel density estimation, which uses Scott's Rule (Scott, 2010) for bandwidth selection. The simulated survey was compiled by sampling from a distribution of local densities as described in section 4.3.5.

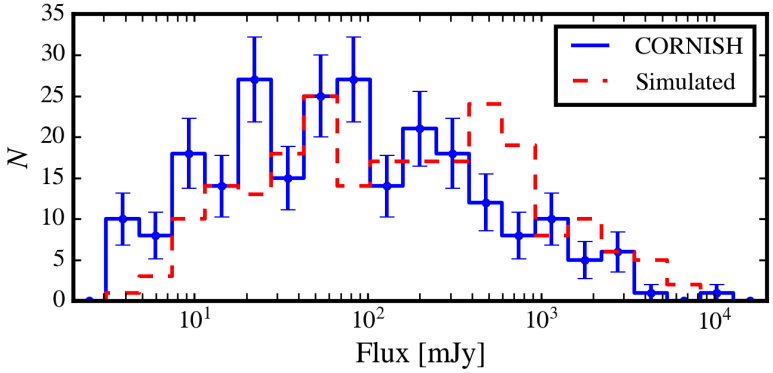

Fig. 4.14 Distribution of UCHII regions with integrated flux. The red histogram is the distribution of simulated UCHII regions that would be included in the CORNISH survey and the blue histogram with error bars shows the CORNISH sample. The simulated survey was compiled by sampling from a distribution of local densities as described in section 4.3.5.

this weighted survey are shown in figures 4.11 to 4.14. These figures show that close agreement between the model and the results of the CORNISH survey can be achieved by noting that stars are born in environments with a variety of densities.

4.4 Conclusion

In this chapter I have presented the results of simulating the CORNISH survey for stars in different local densities by assuming a Galactic density distribution, a stellar accretion model, and a model for the evolution of cometary HII regions.

The Galactic density model is not perfect; we see a narrower latitude distribution in the CORNISH survey. There are more stars with distances from the sun between $5\,\mathrm{kpc} < d < 12\,\mathrm{kpc}$ in the simulations than that observed. Even with these issues the spatial distribution was sufficiently accurate for the rest of the analyses.

It was shown that the models used can reproduce the observed size and flux distributions in the CORNISH survey. Higher density environments lead to better fits to the observed size distributions. The same can be said for the flux distributions except that the fit gets worse for simulations with $n_\star > 6.4 \times 10^4\,\mathrm{cm}^{-3}$. We can get the right number of UCHII regions in the simulated surveys for $\mathrm{SFR} = 1.5\,\mathrm{M}_\odot\,\mathrm{yr}^{-1}$ if we consider that stars are born in a distribution of local densities rather than a single density.

Chapter 5

Conclusions

5.1 Summary

In this thesis I have presented research on the population of UCHII regions in the Milky Way. I developed TORCH (see chapter 2), a high-performance multi-physics integration code capable of simulating the coupled evolution of a star's radiation field, stellar wind and ambient gas. The code utilises Strang splitting to reduce the coupling error associated with integrating separate physical sub-problems concurrently. I have used the work of Nishikawa and Kitamura (2008) to create a rotated-hybrid HLL-HLLC Riemann solver in an effort to repress non-physical unstable flow fields (such as the carbuncle instability). To calculate the ionisation fraction of hydrogen and the change in energy due to photo-ionisations, collisional ionisations, and recombinations I implemented the C^2–Ray method by Mellema et al. (2006). The C^2–Ray method includes a fast interpolative ray-casting scheme to calculate optical depths and an implicit solver for the ionisation fraction.

With TORCH I produced simulations of ZAMS stars that are off-centre in a power-law ($\alpha = 2$) density field (the birth cloud) and are blowing strong stellar winds. I simulated stars with a variety of masses that span the range that UCHII regions are associated with. Stars were located at a single distance from the centre

of their birth clouds ($r_{sc} = 0.35\,pc$). Varying this distance would have little effect on the results (other than mildly affecting morphologies) as there is degeneracy between stars in higher density clouds that are further from the centre and stars in lower density clouds that are closer to the centre. The hydrostatic models of Meynet and Maeder (2000) provided each star's effective temperature and luminosity, which were used to calculate the mass-loss rates and terminal velocities of the stellar wind via the stellar wind model of Vink et al. (2001). Lyman continuum fluxes were taken from the results of Martins et al. (2005) and Lanz and Hubeny (2007). For each star multiple simulations were carried out for different environment densities between $n_\star = 0.8 \times 10^4\,cm^{-3}$ to $n_\star = 12.8 \times 10^4\,cm^{-3}$. Simulated observations of these model HII regions match well with those observed, clearly showing cavities and limb-brightened morphologies. Adjusting the viewing angle of these observations led to significant changes in morphological classification. Classification of CORNISH UCHII regions by Kalcheva (2017, in prep) is showing that most are cometary after removing those that are unresolved. All of the models produced regions bounding fully ionised gas that were roughly spherical, with shallower density structures than the surrounding material. This feature was further expressed through a comparison of the SEDs of the power-law models and corresponding uniform density models, which were almost identical.

With a grid of cometary models that spans a significant portion of the parameter space of UCHII regions I set out in chapter 4 to use these models to simulate a survey of simulated observations using a generated population of stars in our Galaxy. The Davies et al. (2011) galaxy population synthesis code was improved upon by using a more up-to-date model of the Galactic electron density distribution and, with the grid, a more realistic model of HII region evolution. It was found that stars in the higher density surveys, with $n_\star \geq 6.4 \times 10^4\,cm^{-3}$, gave closer qualitative agreement to distributions of integrated flux and size. Assuming all stars are born in the same density environment results in an over-prediction of the overall number of UCHII

region samples for stars in high densities, $n_\star \geq 6.4 \times 10^4\,\mathrm{cm}^{-3}$. This is because stars in higher densities have a higher chance of being detected (due to their smaller sizes) and also because HII region stagnation becomes important for high density fields, where the limiting sizes lie within CORNISH selection bounds. These results suggest that the number of UCHII regions in the Galaxy that are embedded in high densities is relatively low but, as they are more likely to be included in the CORNISH survey, the distribution can still be dominated by these regions. Assuming stars lie in a power-law probability density distribution as a function of local stellar density (with power-law index $= -0.5$) I was able to get very close fits to not only the shape of the flux and size distributions of the CORNISH survey but also the overall number of UCHII regions. It should be noted, however, that we could also get similar results by modifying the ambient temperature (and therefore the stagnation radius of the HII regions). What I have shown here is the effect of a density distribution on the shape of the other distributions and their normalisation.

Overall it was found that the prescriptions used to simulate surveys of UCHII regions lead to results that are consistent with what is observed.

5.2 Future Work and Improvements

The resolution of the model HII regions at early times is sometimes too low. This may have seeded numerical instabilities that grow through to the solution at later times. An improvement would be to run simulations on an AMR (adaptive mesh refinement) grid. This, however, introduces another problem in that the C^2–Ray scheme must be extended to handle interpolating optical depths over coarse-fine cell interfaces. In section A.2 I show a possible scheme for short characteristics ray tracing on AMR grids.

Another issue with the ray tracing in TORCH is that it was not possible to run it in parallel. The hydrodynamics can be parallelised but, due to the constraint that

cells must be causally iterated over, the ray tracing schemes in the radiative transfer and heating/cooling modules cannot. To do so would require partitioning the grid into independent causally linked paths through the grid, which may introduce too much parallel over-head through the increased number of "ghost-cells" surrounding non-cuboidal grids. One can, however, get some parallelism by partitioning the grid into the sections that are traversed separately from the starting positions described in section 2.2.3. The level of parallelism then depends on where the star is in the grid. If high-resolution simulations are desired, it may be better to switch to an explicit scheme for the integration of the ionisation fraction. Although the time-step constraint is more severe for this family of integration schemes, cells may not need to be causally iterated over (see section 2.2.3), meaning each sub-problem can be solved in parallel, which may over-compensate for this increase in computation. For the current work, this was not necessary because I was running many low-resolution models. An adaptive ray tracing scheme that uses HEALPix (Hierarchical Equal-Area isoLatitude Pixelization of the sphere) (Górski et al., 2005) such as that of Abel and Wandelt (2002) would be a great improvement to the current scheme for high-resolution AMR simulations.

The models described a specific scenario for HII region evolution. In reality not all UCHII regions are cometary, and generally form in a clumpy ISM with a variety of birth environments. Steeper density gradients could lead to runaway photo-ionisation on the edges of clouds whilst flatter gradients would lead to more spherically symmetric regions. The proper motion of the stars was neglected, which can affect HII region morphology as not only does the environment of these stars change over their lifetimes but they may also form bow shocks if they are moving supersonically with respect the ambient medium. Another issue with the models is that a temperature gradient was used in order to keep the birth cloud of each HII region in pressure equilibrium. It would be more accurate to have a physically justified model of the cloud, such as a Bonnor–Ebert sphere, and simulate the effects

of self-gravity. Lastly, as I was running low-resolution simulations, the fixed grid led to a large injection region that could have affected these results. Again, this can be remedied with AMR grids.

It would be interesting to see how the distributions in chapter 4 change once a more realistic cloud model is used to to simulate UCHII regions. For example, the stagnation radius of a HII region in equation 3.25 depends on the sound speed of the ambient medium. A lower ambient temperature would lead to a higher stagnation radius, which would not change the results of the lower density surveys ($n_\star < 6.4 \times 10^4\,\mathrm{cm}^{-3}$) as all the HII regions stagnate at sizes too large to be included in the CORNISH survey. It would, however, lead to changes in the shape and normalization of the distributions resulting from the higher density surveys ($n_\star \geq 6.4 \times 10^4\,\mathrm{cm}^{-3}$). For example, reducing the ambient temperature local to the star from 300 K to 10 K would lead to stagnation radii that are 10 times larger.

One could simulate surveys resulting from a number of different HII region models and compare the distributions with CORNISH. The sensitivity of the distributions to varying these models would be tested and we would, as a result, know more about the parameter space that UCHII regions occupy.

Fitting the kinematics of cometary HII region models to individual objects is something that wasn't explored in this thesis. Different velocity structures are predicted by different models, e.g. peak line widths are found ahead of the ionising star in bow shock models as opposed to in the tail as found in champagne flow models. Therefore, these studies can help distinguish between different models. I have updated the code by Dougherty et al. (2003) so that it is capable of producing simulated radio recombination line observations (see section 2.4.2). With this one could directly compare simulations with real observations, such as the deep H53α and H66α radio recombination line observations of DR 21 by Cyganowski et al. (2003).

References

Abel, T., Norman, M. L., and Madau, P. (1999). Photon-conserving Radiative Transfer around Point Sources in Multidimensional Numerical Cosmology. *ApJ*, 523:66–71.

Abel, T. and Wandelt, B. D. (2002). Adaptive ray tracing for radiative transfer around point sources. *MNRAS*, 330:L53–L56.

van Albada, G. D., van Leer, B., and Roberts, Jr., W. W. (1982). A comparative study of computational methods in cosmic gas dynamics. *A&A*, 108:76–84.

Arquilla, R. and Goldsmith, P. F. (1985). Density distributions in dark clouds. *ApJ*, 297:436–454.

Arthur, S. J. (2007). Off-Center H II Regions in Power-Law Density Distributions. *ApJ*, 670:471–479.

Arthur, S. J. and Hoare, M. G. (2006). Hydrodynamics of Cometary Compact H II Regions. *ApJS*, 165:283–306.

Avila-Reese, V. and Vázquez-Semadeni, E. (2001). Turbulent Dissipation in the Interstellar Medium: The Coexistence of Forced and Decaying Regimes and Implications for Galaxy Formation and Evolution. *ApJ*, 553:645–660.

Baldwin, J. A., Ferland, G. J., Martin, P. G., Corbin, M. R., Cota, S. A., Peterson, B. M., and Slettebak, A. (1991). Physical conditions in the Orion Nebula and an assessment of its helium abundance. *ApJ*, 374:580–609.

Bedijn, P. J. and Tenorio-Tagle, G. (1981). The gasdynamics of H II regions. IV - The champagne phase and the propagation of ionization fronts into dense clouds. *A&A*, 98:85–91.

Beuther, H., Churchwell, E. B., McKee, C. F., and Tan, J. C. (2007). The Formation of Massive Stars. *Protostars and Planets V*, pages 165–180.

Biskamp, D. and Müller, W.-C. (2000). Scaling properties of three-dimensional isotropic magnetohydrodynamic turbulence. *Physics of Plasmas*, 7:4889–4900.

Bocher, M. (1906). Introduction to the theory of fourier's series. *Annals of Mathematics*, 7(3):81–152.

Bodenheimer, P., Tenorio-Tagle, G., and Yorke, H. W. (1979). The gas dynamics of H II regions. II - Two-dimensional axisymmetric calculations. *ApJ*, 233:85–96.

Bondi, H. (1952). On spherically symmetrical accretion. *MNRAS*, 112:195.

Bonnell, I. A., Bate, M. R., Clarke, C. J., and Pringle, J. E. (2001). Competitive accretion in embedded stellar clusters. *MNRAS*, 323:785–794.

Bonnell, I. A., Smith, R. J., Clark, P. C., and Bate, M. R. (2011). The efficiency of star formation in clustered and distributed regions. *MNRAS*, 410:2339–2346.

Brocklehurst, M. and Leeman, S. (1971). The Pressure Broadening of Radio Recombination Lines. *Astrophys. Lett.*, 9:35.

Brocklehurst, M. and Seaton, M. J. (1972). On the interpretation of radio recombination line observations. *MNRAS*, 157:179.

van Buren, D. and Mac Low, M.-M. (1992). Bow shock models for the velocity structure of ultracompact H II regions. *ApJ*, 394:534–538.

van Buren, D., Mac Low, M.-M., Wood, D. O. S., and Churchwell, E. (1990). Cometary compact H II regions are stellar-wind bow shocks. *ApJ*, 353:570–578.

Cantó, J., Raga, A. C., and Rodríguez, L. F. (2000). The Hot, Diffuse Gas in a Dense Cluster of Massive Stars. *ApJ*, 536:896–901.

Caselli, P. and Myers, P. C. (1995). The Line Width–Size Relation in Massive Cloud Cores. *ApJ*, 446:665.

Castor, J., McCray, R., and Weaver, R. (1975). Interstellar bubbles. *ApJ*, 200:L107–L110.

Cesaroni, R., Pestalozzi, M., Beltrán, M. T., Hoare, M. G., Molinari, S., Olmi, L., Smith, M. D., Stringfellow, G. S., Testi, L., and Thompson, M. A. (2015). Infrared emission of young HII regions: a Herschel/Hi-GAL study. *A&A*, 579:A71.

Chevalier, R. A. and Clegg, A. W. (1985). Wind from a starburst galaxy nucleus. *Nature*, 317:44.

Cho, J. and Lazarian, A. (2003). Compressible magnetohydrodynamic turbulence: mode coupling, scaling relations, anisotropy, viscosity-damped regime and astrophysical implications. *MNRAS*, 345:325–339.

Churchwell, E. (2002). Ultra-Compact HII Regions and Massive Star Formation. *ARA&A*, 40:27–62.

Comeron, F. (1997). Dynamical evolution of wind-driven HII regions in strong density gradients. *A&A*, 326:1195–1214.

Comeron, F. and Kaper, L. (1998). Numerical simulations of wind bow shocks produced by runaway OB stars. *A&A*, 338:273–291.

Cordes, J. M. and Lazio, T. J. W. (2002). NE2001.I. A New Model for the Galactic Distribution of Free Electrons and its Fluctuations. *ArXiv Astrophysics e-prints*.

Cunningham, A. J., Klein, R. I., Krumholz, M. R., and McKee, C. F. (2011). Radiation-hydrodynamic Simulations of Massive Star Formation with Protostellar Outflows. *ApJ*, 740:107.

Cyganowski, C. J., Reid, M. J., Fish, V. L., and Ho, P. T. P. (2003). Dual Cometary H II Regions in DR 21: Bow Shocks or Champagne Flows? *ApJ*, 596:344–349.

Dale, J. E., Bonnell, I. A., and Whitworth, A. P. (2007). Ionization-induced star formation - I. The collect-and-collapse model. *MNRAS*, 375:1291–1298.

Davies, B., Hoare, M. G., Lumsden, S. L., Hosokawa, T., Oudmaijer, R. D., Urquhart, J. S., Mottram, J. C., and Stead, J. (2011). The Red MSX Source survey: critical tests of accretion models for the formation of massive stars. *MNRAS*, 416:972–990.

De Pree, C. G., Wilner, D. J., Deblasio, J., Mercer, A. J., and Davis, L. E. (2005). The Morphologies of Ultracompact H II Regions in W49A and Sagittarius B2: The Prevalence of Shells and a Modified Classification Scheme. *ApJ*, 624:L101–L104.

Deharveng, L., Lefloch, B., Zavagno, A., Caplan, J., Whitworth, A. P., Nadeau, D., and Martín, S. (2003). Triggered massive-star formation at the border of the H II Region Sh 104. *A&A*, 408:L25–L28.

Dougherty, S. M., Pittard, J. M., Kasian, L., Coker, R. F., Williams, P. M., and Lloyd, H. M. (2003). Radio emission models of colliding-wind binary systems. *A&A*, 409:217–233.

Dyson, J. E., Williams, R. J. R., and Redman, M. P. (1995). Clumpy Ultra Compact HII Regions - Part One - Fully Supersonic Wind-Blown Models. *MNRAS*, 277:700.

Elmegreen, B. G. (1998). Observations and Theory of Dynamical Triggers for Star Formation. In Woodward, C. E., Shull, J. M., and Thronson, Jr., H. A., editors, *Origins*, volume 148 of *Astronomical Society of the Pacific Conference Series*, page 150.

Elmegreen, B. G. and Lada, C. J. (1977). Sequential formation of subgroups in OB associations. *ApJ*, 214:725–741.

Falle, S. A. E. G. (1991). Self-similar jets. *MNRAS*, 250:581–596.

Felli, M., Churchwell, E., and Massi, M. (1984). A high-resolution study of M17 at 1.3, 2, 6, and 21 CM. *A&A*, 136:53–64.

Franco, J., Tenorio-Tagle, G., and Bodenheimer, P. (1990). On the formation and expansion of H II regions. *ApJ*, 349:126–140.

Gaume, R. A., Fey, A. L., and Claussen, M. J. (1994). VLA recombination line observations of the cometary H II region G34.3+0.2: Dynamics and physical properties. *ApJ*, 432:648–655.

Glebbeek, E., Gaburov, E., Portegies Zwart, S., and Pols, O. R. (2013). Structure and evolution of high-mass stellar mergers. *MNRAS*, 434:3497–3510.

Godunov, S. K. (1959). A difference method for numerical calculation of discontinuous solutions of the equations of hydrodynamics. *Matematicheskii Sbornik*, 89(3):271–306.

Gordon, M. A. and Sorochenko, R. L., editors (2009). *Radio Recombination Lines*, volume 282 of *Astrophysics and Space Science Library*.

Górski, K. M., Hivon, E., Banday, A. J., Wandelt, B. D., Hansen, F. K., Reinecke, M., and Bartelmann, M. (2005). HEALPix: A Framework for High-Resolution Discretization and Fast Analysis of Data Distributed on the Sphere. *ApJ*, 622:759–771.

Gritschneder, M., Naab, T., Walch, S., Burkert, A., and Heitsch, F. (2009). Driving Turbulence and Triggering Star Formation by Ionizing Radiation. *ApJ*, 694:L26–L30.

Harten, A. (1983). High resolution schemes for hyperbolic conservation laws. *J. Comput. Phys.*, 49(3):357–393.

Hatchell, J. and van der Tak, F. F. S. (2003). The physical structure of high-mass star-forming cores. *A&A*, 409:589–598.

Hennebelle, P., Whitworth, A. P., Cha, S.-H., and Goodwin, S. P. (2004). Protostellar collapse induced by compression - II. Rotation and fragmentation. *MNRAS*, 348:687–701.

Hennebelle, P., Whitworth, A. P., Gladwin, P. P., and André, P. (2003). Protostellar collapse induced by compression. *MNRAS*, 340:870–882.

Henney, W. J., Arthur, S. J., de Colle, F., and Mellema, G. (2009). Radiation-magnetohydrodynamic simulations of the photoionization of magnetized globules. *MNRAS*, 398:157–175.

Henney, W. J., Arthur, S. J., and García-Díaz, M. T. (2005). Photoevaporation Flows in Blister H II Regions. I. Smooth Ionization Fronts and Application to the Orion Nebula. *ApJ*, 627:813–833.

Hills, J. G. and Day, C. A. (1976). Stellar Collisions in Globular Clusters. *Astrophys. Lett.*, 17:87.

Hoare, M. G., Kurtz, S. E., Lizano, S., Keto, E., and Hofner, P. (2007). Ultracompact Hii Regions and the Early Lives of Massive Stars. *Protostars and Planets V*, pages 181–196.

Hoare, M. G., Purcell, C. R., Churchwell, E. B., Diamond, P., Cotton, W. D., Chandler, C. J., Smethurst, S., Kurtz, S. E., Mundy, L. G., Dougherty, S. M., Fender, R. P., Fuller, G. A., Jackson, J. M., Garrington, S. T., Gledhill, T. R., Goldsmith, P. F., Lumsden, S. L., Martí, J., Moore, T. J. T., Muxlow, T. W. B., Oudmaijer, R. D., Pandian, J. D., Paredes, J. M., Shepherd, D. S., Spencer, R. E., Thompson, M. A., Umana, G., Urquhart, J. S., and Zijlstra, A. A. (2012). The Coordinated Radio and Infrared Survey for High-Mass Star Formation (The CORNISH Survey). I. Survey Design. *PASP*, 124:939–955.

Hoyle, F. and Lyttleton, R. A. (1939). The effect of interstellar matter on climatic variation. *Proceedings of the Cambridge Philosophical Society*, 35:405.

Hummer, D. G. (1994). Total Recombination and Energy Loss Coefficients for Hydrogenic Ions at Low Density for 10<T/E/Z/2<10/7K. *MNRAS*, 268:109.

Icke, V. (1979a). Star formation through an accretion shock - A model for H/+/ blisters. *A&A*, 78:352–361.

Icke, V. (1979b). The propagation of an ionization front in an inhomogeneous medium. *ApJ*, 234:615–618.

Icke, V., Gatley, I., and Israel, F. P. (1980). The appearance of dusty H II blisters at radio and infrared wavelengths. *ApJ*, 236:808–822.

Immer, K., Cyganowski, C., Reid, M. J., and Menten, K. M. (2014). The cometary H II regions of DR 21: Bow shocks or champagne flows or both? *A&A*, 563:A39.

Israel, F. P. (1978). H II regions and CO clouds - The blister model. *A&A*, 70:769–775.

Kahn, F. D. (1974). Cocoons around early-type stars. *A&A*, 37:149–162.

Kennicutt, Jr., R. C. (1998). The Global Schmidt Law in Star-forming Galaxies. *ApJ*, 498:541–552.

Kolmogorov, A. N. (1941). The Local Structure of Turbulence in Incompressible Viscous Fluid for Very Large Reynolds' Numbers. In *Dokl. Akad. Nauk SSSR*, volume 30, pages 301–305.

Koo, B.-C. and McKee, C. F. (1992). Dynamics of wind bubbles and superbubbles. I - Slow winds and fast winds. II - Analytic theory. *ApJ*, 388:93–126.

Korycansky, D. G. (1992). An off-center point explosion in a radially stratified medium - Kompaneets approximation. *ApJ*, 398:184–189.

de Koter, A., Heap, S. R., and Hubeny, I. (1997). On the Evolutionary Phase and Mass Loss of the Wolf-Rayet–like Stars in R136a. *ApJ*, 477:792.

de Koter, A., Schmutz, W., and Lamers, H. J. G. L. M. (1993). A Fast Non-Lte Code for Expanding Atmospheres - a Test of the Validity of the Sobolev Approximation. *A&A*, 277:561.

Koyama, H. and Inutsuka, S.-I. (2000). Molecular Cloud Formation in Shock-compressed Layers. *ApJ*, 532:980–993.

Koyama, H. and Inutsuka, S.-i. (2002). An Origin of Supersonic Motions in Interstellar Clouds. *ApJ*, 564:L97–L100.

Kritsuk, A. G., Lee, C. T., and Norman, M. L. (2013). A supersonic turbulence origin of Larson's laws. *MNRAS*, 436:3247–3261.

Kroupa, P. (2001). On the variation of the initial mass function. *MNRAS*, 322:231–246.

Krumholz, M. R., McKee, C. F., and Klein, R. I. (2005). How Protostellar Outflows Help Massive Stars Form. *ApJ*, 618:L33–L36.

Kuiper, R., Klahr, H., Beuther, H., and Henning, T. (2011). Three-dimensional Simulation of Massive Star Formation in the Disk Accretion Scenario. *ApJ*, 732:20.

Kurtz, S., Churchwell, E., and Wood, D. O. S. (1994). Ultracompact H II regions. 2: New high-resolution radio images. *ApJS*, 91:659–712.

Lamers, H. J. G. L. M. and Leitherer, C. (1993). What are the mass-loss rates of O stars? *ApJ*, 412:771–791.

Lamers, H. J. G. L. M., Snow, T. P., and Lindholm, D. M. (1995). Terminal Velocities and the Bistability of Stellar Winds. *ApJ*, 455:269.

Laney, C. (1998). *Computational Gasdynamics*. Cambridge University Press.

Lang, K. R. (1978). *Astrophysical formulae. A compendium for the physicist and astrophysicist.*

Lanz, T. and Hubeny, I. (2007). A Grid of NLTE Line-blanketed Model Atmospheres of Early B-Type Stars. *ApJS*, 169:83–104.

Larson, R. B. (1981). Turbulence and star formation in molecular clouds. *MNRAS*, 194:809–826.

Larson, R. B. and Starrfield, S. (1971). On the formation of massive stars and the upper limit of stellar masses. *A&A*, 13:190–197.

van Leer, B. (1979). Towards the ultimate conservative difference scheme. V - A second-order sequel to Godunov's method. *Journal of Computational Physics*, 32:101–136.

Li, Z.-Y. and Nakamura, F. (2006). Cluster Formation in Protostellar Outflow-driven Turbulence. *ApJ*, 640:L187–L190.

Liou, M.-S. (2000). Mass flux schemes and connection to shock instability. *Journal of Computational Physics*, 160(2):623–648.

Lumsden, S. L. and Hoare, M. G. (1996). An Infrared Study of the Velocity Structure of the Cometary Compact H II Region G29.96-0.02. *ApJ*, 464:272.

Lumsden, S. L., Hoare, M. G., Urquhart, J. S., Oudmaijer, R. D., Davies, B., Mottram, J. C., Cooper, H. D. B., and Moore, T. J. T. (2013). The Red MSX Source Survey: The Massive Young Stellar Population of Our Galaxy. *ApJS*, 208:11.

Mac Low, M.-M., van Buren, D., Wood, D. O. S., and Churchwell, E. (1991). Bow shock models of ultracompact H II regions. *ApJ*, 369:395–409.

Mac Low, M.-M., Klessen, R. S., Burkert, A., and Smith, M. D. (1998). Kinetic Energy Decay Rates of Supersonic and Super-Alfvénic Turbulence in Star-Forming Clouds. *Physical Review Letters*, 80:2754–2757.

Mac Low, M.-M., Toraskar, J., Oishi, J. S., and Abel, T. (2007). Dynamical Expansion of H II Regions from Ultracompact to Compact Sizes in Turbulent, Self-gravitating Molecular Clouds. *ApJ*, 668:980–992.

Maron, J. and Goldreich, P. (2001). Simulations of Incompressible Magnetohydrodynamic Turbulence. *ApJ*, 554:1175–1196.

Martins, F., Schaerer, D., and Hillier, D. J. (2005). A new calibration of stellar parameters of Galactic O stars. *A&A*, 436:1049–1065.

Mathieu, R. D. (1994). Pre-Main-Sequence Binary Stars. *ARA&A*, 32:465–530.

Matzner, C. D. (2002). On the Role of Massive Stars in the Support and Destruction of Giant Molecular Clouds. *ApJ*, 566:302–314.

McKee, C. F. (1999). The Dynamical Structure and Evolution of Giant Molecular Clouds. In Lada, C. J. and Kylafis, N. D., editors, *NATO Advanced Science Institutes (ASI) Series C*, volume 540 of *NATO Advanced Science Institutes (ASI) Series C*, page 29.

McKee, C. F. and Tan, J. C. (2002). Massive star formation in 100,000 years from turbulent and pressurized molecular clouds. *Nature*, 416:59–61.

McKee, C. F. and Tan, J. C. (2003). The Formation of Massive Stars from Turbulent Cores. *ApJ*, 585:850–871.

McMullin, J., Waters, B., Schiebel, D., Young, W., and Golap, K. (2007). Astronomical data analysis software and systems xvi (asp conf. ser. 376), ed. *RA Shaw, F. Hill, & DJ Bell (San Francisco, CA: ASP)*, 127.

Mellema, G., Iliev, I. T., Alvarez, M. A., and Shapiro, P. R. (2006). C^2-ray: A new method for photon-conserving transport of ionizing radiation. *New A*, 11:374–395.

Meynet, G. and Maeder, A. (2000). Stellar evolution with rotation. V. Changes in all the outputs of massive star models. *A&A*, 361:101–120.

Miller, III, W. W. and Cox, D. P. (1993). The Diffuse Ionized Interstellar Medium: Structures Resulting from Ionization by O Stars. *ApJ*, 417:579.

Mottram, J. C., Hoare, M. G., Davies, B., Lumsden, S. L., Oudmaijer, R. D., Urquhart, J. S., Moore, T. J. T., Cooper, H. D. B., and Stead, J. J. (2011). The RMS Survey: The Luminosity Functions and Timescales of Massive Young Stellar Objects and Compact H II Regions. *ApJ*, 730:L33.

Myers, P. C. and Fuller, G. A. (1992). Density structure and star formation in dense cores with thermal and nonthermal motions. *ApJ*, 396:631–642.

Nishikawa, H. and Kitamura, K. (2008). Very simple, carbuncle-free, boundary-layer-resolving, rotated-hybrid riemann solvers. *Journal of Computational Physics*, 227(4):2560 – 2581.

Osterbrock, D. E. (1989). *Astrophysics of gaseous nebulae and active galactic nuclei*.

Padoan, P. and Nordlund, Å. (1999). A Super-Alfvénic Model of Dark Clouds. *ApJ*, 526:279–294.

Pavlovski, G., Smith, M. D., and Mac Low, M.-M. (2006). Hydrodynamical simulations of the decay of high-speed molecular turbulence - II. Divergence from isothermality. *MNRAS*, 368:943–958.

Pavlovski, G., Smith, M. D., Mac Low, M.-M., and Rosen, A. (2002). Hydrodynamical simulations of the decay of high-speed molecular turbulence - I. Dense molecular regions. *MNRAS*, 337:477–487.

Pirogov, L. E. (2009). Density profiles in molecular cloud cores associated with high-mass star-forming regions. *Astronomy Reports*, 53:1127–1135.

Preibisch, T. and Zinnecker, H. (2007). Sequentially triggered star formation in OB associations. In Elmegreen, B. G. and Palous, J., editors, *Triggered Star Formation in a Turbulent ISM*, volume 237 of *IAU Symposium*, pages 270–277.

Purcell, C. R., Hoare, M. G., Cotton, W. D., Lumsden, S. L., Urquhart, J. S., Chandler, C., Churchwell, E. B., Diamond, P., Dougherty, S. M., Fender, R. P., Fuller, G., Garrington, S. T., Gledhill, T. M., Goldsmith, P. F., Hindson, L., Jackson, J. M., Kurtz, S. E., Martí, J., Moore, T. J. T., Mundy, L. G., Muxlow, T. W. B., Oudmaijer, R. D., Pandian, J. D., Paredes, J. M., Shepherd, D. S., Smethurst, S., Spencer, R. E., Thompson, M. A., Umana, G., and Zijlstra, A. A. (2013). The Coordinated Radio and Infrared Survey for High-mass Star Formation. II. Source Catalog. *ApJS*, 205:1.

Quirk, J. J. (1994). A contribution to the great riemann solver debate. *International Journal for Numerical Methods in Fluids*, 18(6):555–574.

Raga, A. C., Cantó, J., and Rodríguez, L. F. (2012). The universal time-evolution of an expanding HII region. *Rev. Mexicana Astron. Astrofis.*, 48:149–157.

Raga, A. C., Mellema, G., and Lundqvist, P. (1997a). An Axisymmetric, Radiative Bow Shock Model with a Realistic Treatment of Ionization and Cooling. *ApJS*, 109:517–535.

Raga, A. C., Noriega-Crespo, A., Cantó, J., Steffen, W., van Buren, D., Mellema, G., and Lundqvist, P. (1997b). The Bow Shock and H II Regions around a Runaway O Star. *Rev. Mexicana Astron. Astrofis.*, 33:73–81.

Redman, M. P., Williams, R. J. R., and Dyson, J. E. (1996). Clumpy ultracompact H II regions. II. Cores, spheres and shells from subsonic flows. *MNRAS*, 280:661–666.

Reid, M. J. and Ho, P. T. P. (1985). G34.3 + 0.2 - A 'cometary' H II region. *ApJ*, 288:L17–L19.

Rodrigues, O. (1840). Des lois géometriques qui regissent les déplacements d' un systéme solide dans l' espace, et de la variation des coordonnées provenant de ces déplacement considérées indépendent des causes qui peuvent les produire. *Journal de Mathématiques Pures et Appliquées*, 5:380 – 440.

Roe, P. L. (1981). Approximate Riemann Solvers, Parameter Vectors, and Difference Schemes. *Journal of Computational Physics*, 43:357–372.

Rozyczka, M. (1985). Two-dimensional models of stellar wind bubbles. I - Numerical methods and their application to the investigation of outer shell instabilities. *A&A*, 143:59–71.

Ruffert, M. (1994). Three-dimensional hydrodynamic Bondi-Hoyle accretion. III. Mach 0.6, 1.4 and 10; γ=5/3. *A&AS*, 106.

Ruffert, M. and Arnett, D. (1994). Three-dimensional hydrodynamic Bondi-Hoyle accretion. 2: Homogeneous medium at Mach 3 with gamma = 5/3. *ApJ*, 427:351–376.

Rusanov, V. (1962). The calculation of the interaction of non-stationary shock waves and obstacles. *USSR Computational Mathematics and Mathematical Physics*, 1(2):304 – 320.

Scott, D. W. (2010). Scott's rule. *Wiley Interdisciplinary Reviews: Computational Statistics*, 2(4):497–502.

Silich, S., Tenorio-Tagle, G., and Muñoz-Tuñón, C. (2003). On the Rapidly Cooling Interior of Supergalactic Winds. *ApJ*, 590:791–796.

Silich, S., Tenorio-Tagle, G., and Rodríguez-González, A. (2004). Winds Driven by Super Star Clusters: The Self-Consistent Radiative Solution. *ApJ*, 610:226–232.

Spitzer, L. (1978). *Physical Processes in the Interstellar Medium*. New York Wiley-Interscience.

Stone, J. M., Ostriker, E. C., and Gammie, C. F. (1998). Dissipation in Compressible Magnetohydrodynamic Turbulence. *ApJ*, 508:L99–L102.

Strang, G. (1968). On the construction and comparison of difference schemes. *SIAM Journal on Numerical Analysis*, 5(3):506–517.

Strickland, D. K. and Stevens, I. R. (1998). Predicting x-ray emission from wind-blown bubbles - limitations of fits to rosat spectra. *MNRAS*, 297:747–759.

Strömgren, B. (1939). The Physical State of Interstellar Hydrogen. *ApJ*, 89:526.

Sweby, P. K. (1984). High resolution schemes using flux limiters for hyperbolic conservation laws. *SIAM J. Numer. Anal.*, 21(5):995–1011.

van der Tak, F. F. S., van Dishoeck, E. F., Evans, II, N. J., and Blake, G. A. (2000). Structure and Evolution of the Envelopes of Deeply Embedded Massive Young Stars. *ApJ*, 537:283–303.

Tenorio-Tagle, G. (1979). The gas dynamics of H II regions. I - The champagne model. *A&A*, 71:59–65.

Tenorio-Tagle, G., Wünsch, R., Silich, S., and Palouš, J. (2007). Hydrodynamics of the Matter Reinserted within Super Stellar Clusters. *ApJ*, 658:1196–1202.

Tenorio-Tagle, G., Yorke, H. W., and Bodenheimer, P. (1979). The gas dynamics of H II regions. III - The components of the galactic extended low density H II region. *A&A*, 80:110–118.

Toro, E. F. (1997). *Riemann solvers and numerical methods for fluid dynamics : a practical introduction*. Springer, Berlin, New York.

Vázquez-Semadeni, E., Ryu, D., Passot, T., González, R. F., and Gazol, A. (2006). Molecular Cloud Evolution. I. Molecular Cloud and Thin Cold Neutral Medium Sheet Formation. *ApJ*, 643:245–259.

Vink, J. S., de Koter, A., and Lamers, H. J. G. L. M. (2001). Mass-loss predictions for O and B stars as a function of metallicity. *A&A*, 369:574–588.

Vink, J. S., de Koter, A., and Lamers, H. J. G. L. M. (1999). On the nature of the bi-stability jump in the winds of early-type supergiants. *A&A*, 350:181–196.

Vink, J. S., de Koter, A., and Lamers, H. J. G. L. M. (2000). New theoretical mass-loss rates of O and B stars. *A&A*, 362:295–309.

Vishniac, E. T. (1983). The dynamic and gravitational instabilities of spherical shocks. *ApJ*, 274:152–167.

Vishniac, E. T. (1994). Nonlinear instabilities in shock-bounded slabs. *ApJ*, 428:186–208.

Walsh, A. J., Burton, M. G., Hyland, A. R., and Robinson, G. (1998). Studies of ultracompact HII regions - II. High-resolution radio continuum and methanol maser survey. *MNRAS*, 301:640–698.

Weaver, R., McCray, R., Castor, J., Shapiro, P., and Moore, R. (1977). Interstellar bubbles. II - Structure and evolution. *ApJ*, 218:377–395.

Whitworth, A. (1979). The erosion and dispersal of massive molecular clouds by young stars. *MNRAS*, 186:59–67.

Whitworth, A. P., Bhattal, A. S., Chapman, S. J., Disney, M. J., and Turner, J. A. (1994). The Preferential Formation of High-Mass Stars in Shocked Interstellar Gas Layers. *MNRAS*, 268:291.

Williams, R. J. R. (1999). Shadowing instabilities of ionization fronts. *MNRAS*, 310:789–796.

Williams, R. J. R., Dyson, J. E., and Redman, M. P. (1996). Clumpy ultracompact H II regions. III. Cometary morphologies around stationary stars. *MNRAS*, 280:667–672.

Wood, D. O. S. and Churchwell, E. (1989a). Massive stars embedded in molecular clouds - Their population and distribution in the galaxy. *ApJ*, 340:265–272.

Wood, D. O. S. and Churchwell, E. (1989b). The morphologies and physical properties of ultracompact H II regions. *ApJS*, 69:831–895.

Wood, K. and Mathis, J. S. (2004). Monte Carlo photoionization simulations of diffuse ionized gas. *MNRAS*, 353:1126–1134.

Wünsch, R., Silich, S., Palouš, J., and Tenorio-Tagle, G. (2007). Super stellar clusters with a bimodal hydrodynamic solution: an approximate analytic approach. *A&A*, 471:579–583.

Yorke, H. W. and Bodenheimer, P. (1999). The Formation of Protostellar Disks. III. The Influence of Gravitationally Induced Angular Momentum Transport on Disk Structure and Appearance. *ApJ*, 525:330–342.

Yorke, H. W. and Sonnhalter, C. (2002). On the Formation of Massive Stars. *ApJ*, 569:846–862.

Yorke, H. W., Tenorio-Tagle, G., and Bodenheimer, P. (1983). Theoretical radio continuum maps of H II regions in the champagne phase. *A&A*, 127:313–319.

Zavagno, A., Anderson, L. D., Russeil, D., Morgan, L., Stringfellow, G. S., Deharveng, L., Rodón, J. A., Robitaille, T. P., Mottram, J. C., Schuller, F., Testi, L., Billot, N., Molinari, S., di Gorgio, A., Kirk, J. M., Brunt, C., Ward-Thompson, D., Traficante, A., Veneziani, M., Faustini, F., and Calzoletti, L. (2010). Star formation triggered by H II regions in our Galaxy. First results for N49 from the Herschel infrared survey of the Galactic plane. *A&A*, 518:L101.

Zinnecker, H. and Yorke, H. W. (2007). Toward Understanding Massive Star Formation. *ARA&A*, 45:481–563.

Appendix A

Details and Proofs

A.1 Cell Path Length

The length of the segment of a ray passing through a cell is given by

$$\Delta S = \sqrt{1 + \frac{(t_i - s_i)^2 + (t_j - s_j)^2}{(t_k - s_k)^2}} \Delta r \,, \tag{A.1}$$

where i, j and k are vector components, $\vec{t}$ is the target cell centre position vector, $\vec{s}$ is the source position vector and Δr is the physical width of the grid cell. The kth direction is chosen such that

$$\hat{k} = \frac{\hat{n} \cdot (\vec{t} - \vec{s})}{|\hat{n} \cdot (\vec{t} - \vec{s})|} \,, \tag{A.2}$$

where $\hat{n}$ is the geometric normal to the grid cell face (pointing into the grid cell) that the ray crosses, entering the cell.

The cell path length in equation A.1 is found by first noting that

$$\Delta S = |\vec{t} - \vec{c}| \Delta r \,, \tag{A.3}$$

where $\vec{c}$ is the position vector of the point where the ray crosses the square with vertices at the centres of the cells that contribute to the optical depth (see figure 2.5). The crossing point lies somewhere on the line from the source to the target, i.e.

$$\vec{c} = \vec{t} + \lambda(\vec{s} - \vec{t}), \tag{A.4}$$

and λ can be found because we know the kth coordinate of $\vec{c}$:

$$c_k = t_k + \lambda(s_k - t_k) \tag{A.5}$$

$$\lambda = \frac{t_k - c_k}{t_k - s_k} = \frac{1}{t_k - s_k}, \tag{A.6}$$

therefore

$$\begin{aligned} \Delta S &= |\vec{t} - \vec{c}|\Delta r \\ &= \lambda |\vec{t} - \vec{s}|\Delta r \\ &= \frac{\sqrt{(t_i - s_i)^2 + (t_j - s_j)^2 + (t_k - s_k)^2}}{t_k - s_k}\Delta r, \end{aligned} \tag{A.7}$$

giving equation A.1 as required.

A.2 AMR Short Characteristics Ray Tracing

There are only a handful of distinct grid cell arrangements that need special treatment and all occur on coarse-fine AMR grid boundaries. To find which cells contribute to the optical depth to a cell find the triangle that the ray crosses whose vertices are neighbouring cell centres that have the smallest average distance to the crossing point. Next use barycentric interpolation, which calculates weights according to where the ray crosses the triangle plane.

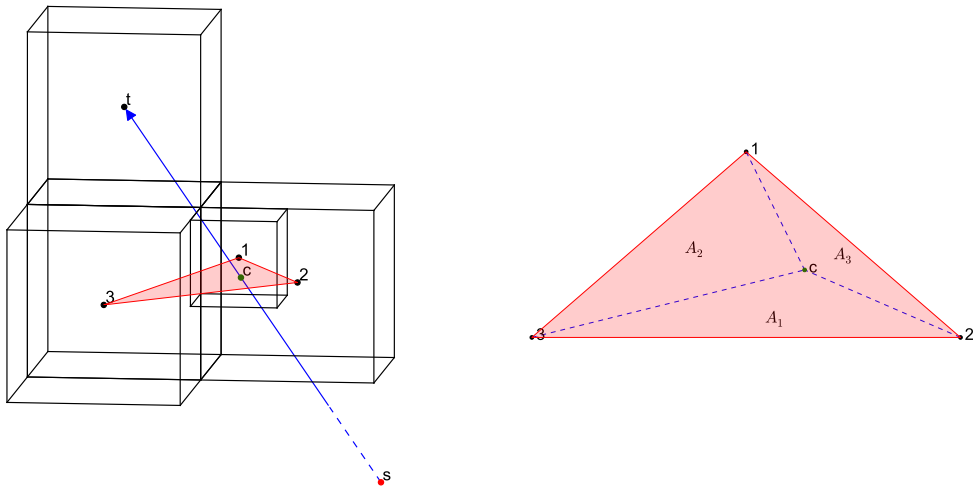

Fig. A.1 This diagram shows a ray passing from the source (the red dot denoted by 's') passing through the interpolation plane (crossing at the green dot, 'c') to the centre of the target grid cell (black dot, 't'). Three nearest neighbours are chosen such that their cell centres (denoted by IDs 1–3) form vertices of a triangle plane that the ray passes through. A barycentric interpolation is then performed, according to where the crossing point (green dot 'c') is on the triangle plane, to find the weight each nearest neighbour contributes to a weighted average of optical depths. The optical depth from source to target cell is then equal to this weighted average.

The optical depth is approximately

$$\tau = \frac{A_1(\tau_1 + \Delta\tau_1) + A_2(\tau_2 + \Delta\tau_2) + A_3(\tau_3 + \Delta\tau_3))}{A}, \tag{A.8}$$

where A_1, A_2 and A_3 are areas shown in figure A.1, A is the area of the triangle and τ_1, τ_2 and τ_3 are the optical depths to cells with cell centre IDs 1, 2 and 3 respectively.

We can find areas A_i from the position vectors of the contributing neighbouring cell centres. First consider a normal vector to the triangle plane,

$$\vec{n} = (\vec{x}_1 - \vec{x}_2) \times (\vec{x}_3 - \vec{x}_1)\,, \tag{A.9}$$

where $\vec{x}_i$ are the position vectors to the cell centres. The equation of the plane containing the triangle is then

$$\vec{n} \cdot (\vec{x} - \vec{x}_1) = 0\,. \tag{A.10}$$

A position $\vec{R}$ on the ray that passes from source to target cell satisfies

$$\vec{R} = \vec{s} + \lambda(\vec{t} - \vec{s})\,, \tag{A.11}$$

where $\vec{s}$ is the position vector of the source, $\vec{t}$ is the position vector of the target cell centre and λ parametrises a position on the ray. At $\lambda = \lambda_c$, the ray crosses the plane,

$$\begin{aligned} &\therefore \quad \vec{n} \cdot (\vec{s} + \lambda_c(\vec{t} - \vec{s}) - \vec{x}_1) = 0 \\ &\implies \lambda_c = \frac{(\vec{x}_1 - \vec{s}) \cdot \vec{n}}{(\vec{t} - \vec{s}) \cdot \vec{n}}\,. \end{aligned} \tag{A.12}$$

The position vector of the crossing point is

$$\vec{c} = \vec{s} + \frac{(\vec{x}_1 - \vec{s}) \cdot \vec{n}}{(\vec{t} - \vec{s}) \cdot \vec{n}}(\vec{t} - \vec{s})\,. \tag{A.13}$$

If a triangle is specified by vectors $\vec{u}$ and $\vec{v}$ originating at one vertex, then the area is a half of the corresponding parallelogram: area $= \frac{1}{2}|\vec{u} \times \vec{v}|$,

$$\begin{aligned} \therefore \quad A &= \frac{1}{2}|\vec{n}| \\ A_1 &= \frac{1}{2}|(\vec{x}_2 - \vec{c}) \times (\vec{x}_3 - \vec{c})| \\ A_2 &= \frac{1}{2}|(\vec{x}_3 - \vec{c}) \times (\vec{x}_1 - \vec{c})| \\ A_3 &= \frac{1}{2}|(\vec{x}_1 - \vec{c}) \times (\vec{x}_2 - \vec{c})| \,. \end{aligned} \tag{A.14}$$

In summary:

$$\begin{aligned} \vec{a}_i &\equiv \varepsilon_{ijk}(\vec{x}_j \times \vec{x}_k) \\ \vec{n} &= \sum_i \vec{a}_i \\ \vec{c} &= \vec{s} + \frac{(\vec{x}_1 - \vec{s}) \cdot \vec{n}}{(\vec{t} - \vec{s}) \cdot \vec{n}}(\vec{t} - \vec{s}) \\ A &= \frac{1}{2}|\vec{n}| \\ A_i &= \frac{1}{2}|(\vec{a}_i - \varepsilon_{ijk}(\vec{x}_j - \vec{x}_k) \times \vec{c})| \,, \end{aligned} \tag{A.15}$$

where ε_{ijk} is the Levi-Civita symbol and $k \neq j \neq i = 1$, 2 or 3.

There is a special case that must be considered when selecting the triangle to use for interpolation. If more than one triangle could be chosen (i.e. they have the same average vertex-to-crossing point distance) then choose the one with the smallest area. If the areas are equal then calculate the result separately for each and take an average at the end.